HAL
open science

Photo-generated Metasurfaces at Terahertz Frequencies

Eduardo Antonio Alvear Cabezon

To cite this version:

Eduardo Antonio Alvear Cabezon. Photo-generated Metasurfaces at Terahertz Frequencies. Electronics. Université Clermont Auvergne [2017-2020], 2019. English. NNT : 2019CLFAC040 . tel-02481483

HAL Id: tel-02481483

https://theses.hal.science/tel-02481483v1

Submitted on 17 Feb 2020

HAL is a multi-disciplinary open access archive for the deposit and dissemination of scientific research documents, whether they are published or not. The documents may come from teaching and research institutions in France or abroad, or from public or private research centers.

L'archive ouverte pluridisciplinaire **HAL**, est destinée au dépôt et à la diffusion de documents scientifiques de niveau recherche, publiés ou non, émanant des établissements d'enseignement et de recherche français ou étrangers, des laboratoires publics ou privés.

UNIVERSITÉ CLERMONT AUVERGNE

ECOLE DOCTORALE DES SCIENCES FONDAMENTALES

THÈSE

Présentée pour obtenir le grade de

DOCTEUR D'UNIVERSITÉ

Spécialité : Physique - Milieux denses et matériaux.

Par « **ALVEAR CABEZÓN Eduardo Antonio** »

Ingénieur double diplôme en Électronique

PHOTO-GENERATED METASURFACES AT TERAHERTZ FREQUENCIES

Soutenue publiquement le « *23/09/2019* », devant la commission d'examen :

COQUILLAT Dominique : Directeur de Recherche, Université Montpellier (Présidente)
MONAT Christelle : Prof. Ecole central de Lyon (Rapporteur)
DEGIRON Aloyse : Chargé de Recherche, Université Paris Diderot (Rapporteur)

CENTENO Emmanuel : Prof. Université Clermont Auvergne (Directeur)
TALIERCIO Thierry : Prof. Université Montpellier (Directeur)
SMAALI Rafik : MCF. Université Clermont Auvergne (Co-directeur)

Dedicated to my family...

"*If I have seen further than others, it is by standing upon the shoulders of Giants.*"

Isaac Newton

Prologue

In the terahertz (THz) frequency range, the need to develop THz devices to obtain a versatile control of the THz waves at high-speed modulation remains a great challenge.

Electro-optical materials are urgently needed by today's society and for the easy development of the potential THz technology.

Contents

Contents 8

Acknowledgement 11

1 Introduction 13
1.1 Terahertz technology . . . 13
1.2 THz sources and detectors . . . 14
1.3 Indium Arsenide platform for the next-generation of THz detection devices . . . 18
1.4 Thesis motivations . . . 19
1.5 Thesis objective . . . 20

2 Photo-generated metasurfaces at THz frequencies 21
2.1 Photo-generation process at THz frequencies . . . 22
2.2 Interaction of the laser pump with the InAs slab . . . 23
2.3 Photo-generation process . . . 25
2.3.1 Optical absorption process . . . 26
2.3.2 Optical generation process . . . 27
2.3.3 Photo-generated carriers densities . . . 27
2.3.4 Ambipolar transport equation . . . 29
2.3.5 Excess carriers recombination rate . . . 29
2.3.6 Excess carriers lifetime recombination . . . 30
2.3.7 Photo-generated patterns distribution . . . 33
2.4 Efficient implementation of the RCWA method . . . 35
2.4.1 THz waves in TE polarization . . . 35
2.4.2 THz waves in TM polarization . . . 36
2.5 Results and discussion . . . 37
2.5.1 Thin films . . . 38
2.5.2 Thick films . . . 39
2.5.3 Ultra-thick films . . . 42
2.6 Summary . . . 44

3 Technological fabrication 47
3.1 Photo-conduction devices . . . 47
3.1.1 TLM substrate composition . . . 48
3.1.2 Fabrication - TLM . . . 49
3.1.3 Results and discussion . . . 51
3.2 THz modulation samples: InAs membranes . . . 53

3.2.1 Fabrication process 54
3.2.2 Wet chemical etching : Calibration of the etching rate for InAs using (H_3PO_4: H_2O_2 : H_2O) 56
3.2.3 InAs membranes made by epitaxy growth 56
3.2.4 Results and discussion 57
3.3 Summary 59

4 Optical Characterization 61
4.1 Physical properties of InAs material 61
4.1.1 Photo-luminescence at low-temperature 62
4.1.2 Photo-luminescence at different temperatures 64
4.1.3 Photo-luminescence at room-temperature 67
4.1.4 Numerical simulation of PL at room-temperature 68
4.1.5 Results and discussion 73
4.1.6 Conclusion 73
4.2 Photo-conduction devices 74
4.2.1 Theory and model 74
4.2.2 Optical characterization set-up 79
4.2.3 Results and discussion 82
4.2.4 Conclusion 86
4.3 Summary 87

5 Photo-driven THz modulator 89
5.1 THz modulation samples: InAs membranes 89
5.1.1 Experimental set-up 90
5.1.2 Optical characterization of the InAs membranes 91
5.1.3 Photo-modulation of the transmission of the InAs membranes 93
5.1.4 Conclusion 99
5.2 Photo-driven THz modulator 100
5.2.1 Optical characterization set-up 100
5.2.2 Static photo-driven THz modulator 101
5.2.3 Dynamic photo-driven THz modulator 109
5.2.4 Conclusion 114
5.3 Summary 115

Conclusion and perspectives 117

A Scattering Matrix Method 121

B Finite Difference Method 123

C InAs etching rate calibration 125

Bibliography 129

Publications and Conference proceedings list 139
Publications 139
Conference Proceedings 140

Acknowledgement

First of all, I would like to warmly thank my two advisors for having supported me actively throughout this thesis. Emmanuel Centeno, I would like to express my great gratitude for giving me the opportunity to work by your side on this research project. I would like to thank you for the endless guidance, advice and support that you have provided me. Thierry Taliercio, I really appreciated your scientific rigor and your critical sense which brought me a lot of insight. You have managed to guide me and my experimental work by your constant attention, advice and suggestions.

I express my respectful gratitude to Rafik Smaali, Fernando Gonzalez-Posada and Stéphane Blin, for the attention they have paid to my research and the advice they have lavished on me. Thank you for the discussions and for the interest you have shown in my work on a theoretical and experimental level.

I warmly thank Christelle Monat and Aloyse Degiron, for the care they took in reading this manuscript. I wish to express my gratitude to them for the honor they have given me by accepting to be rapporteurs of my thesis. I would like to thank Dominique Coquillat for the honor that she has given me by accepting to judge this work and to preside over the defense jury.

I thank all the members of the Electromagnetism and Nanophotonics (ELENA) group at the Université Clermont Auvergne that I had the opportunity to meet and that made my last three years in the lab very pleasant. A big thank you to all the people of NANOstructures pour Moyen InfraRouge (NANOMIR) group at the Université de Montpellier, for their good humor and for the availability they have shown towards me. Thanks to the members of the plasmonic group for the great collective work. A great thanks to all the teachers and everyone that I have come across during my Ph.D thesis for their professionalism, pedagogy and friendship. I would like to express my sincere gratitude to my master thesis supervisor Tahsin Akalin for having given me the opportunity to understand the potential of applications at the THz range. I also address a thought to my professors at Pontificia Universidad Católica de Valparaíso (PUCV) in Chile and at École d'ingénieur ESIEE-Paris who gave me the motivation to study fundamental physics with the good education they provided me.

Thank you to my family for supporting me despite the few thousand kilometers that separate us. Thank you, Esther Merlin, for reading my thesis over and over again. Yves Adam, thank you for the quality of your thoughts and keywords. Finally, a big thanks to all my friends that I cannot mention individually.

Chapter 1

Introduction

1.1 Terahertz technology 13
1.2 THz sources and detectors 14
1.3 Indium Arsenide platform for the next-generation of THz detection devices 18
1.4 Thesis motivations 19
1.5 Thesis objective 20

1.1 Terahertz technology

Over the last two decades, the versatile control of terahertz (THz) electromagnetic radiation has been something extremely difficult to obtain. However, the apparition of new needs in our society has increased the motivations in developing the potential of THz technology [1]. The THz frequency is a part of the electromagnetic spectrum from 0.3THz ($1000\mu m$) to 10THz ($30\mu m$) (see figure1.1-A). In this part of the spectrum, a lot of efforts have been made to realize photonic components able to control THz radiations, which are crucial for several application domains, such as security [2], medical imaging [3] and wireless networks [4].

In today's society, the number of acts of terrorism or smugglers has grown exponentially in different regions of the world. In response to these events, the development of preventive alerts detection systems for security applications becomes a crucial need. In this context, the THz radiation is already used at airports for security scanning, since the THz waves can be used to observe many compounds and materials, especially molecular crystals that have vibrational absorption bands at these frequencies [2]. In this form, the THz radiation can detect concealed weapons, target compounds such as explosives [5], drugs [6] and even concealed in envelopes [7], that have a characteristic response at THz frequencies, which can act as spectroscopic fingerprints for material identifications [8] and in imaging quality control for nondestructive evaluation of packaged power electronic devices [9].

All previous development of the THz detection systems have been motivated because THz radiations apparently poses no health risk to humans, where long THz exposure hasn't reported any chromosomal damage [10, 11]. In this scenario, the THz radiation is useful for medical purposes. The THz imaging is already used for medical applications [12, 13] to image and identificate cancer diagnosis [14] and also in agricultural scanning inspection [15, 16].

Besides of the brilliant development in security scanning and medicine imaging, THz technology opens a new frontier for wireless communication systems, since THz band has larger bandwidth that current technology (10 to 100 times larger) [17]. The benefits that the THz band brings in the high demands in data transfer rates [18] (predicted up to 1 terabit-per-second (Tbps) for 2020 [19]) and accompanied of a higher directionality focusing than radio waves allows to overcome the main limitations of the current telecommunications technology [20]. Nevertheless, this THz band has to face several challenges such as weather environment conditions that need to be considered before implementation [21, 22]. In addition, based on the telecommunication domain, the THz radiation has also been implemented for space research in Tbps communication between satellite links [23] since THz radiation in the space do not suffer the atmosphere attenuation [24]. Furthermore, astronomers located in Chile at Atacama Large Millimeter Array (ALMA) have shown interest in THz sensor technology, since that approximately one-half of the total luminosity and 98% of the photons emitted since the Big-Bang fall into the submillimeter and far-IR. In this scenario, astronomers are able to detect the electromagnetic waves passing through atmospheric windows between 30GHz (0.03THz) and 950GHz (0.95THz). The monitoring could help to prove the existence of the invisible dark universe, including newborn galaxies as far as 13 billion light years away, the birth of a new solar system, or extraterrestrial organic molecules [25, 26].

1.2 THz sources and detectors

Since the advent of efficient THz sources, different varieties of coherent THz sources have been created (see figure1.1-B) [26] such as solid-state electronic devices which are limited to low frequencies generation, quantum cascade laser (THz-QCL) and optical THz generation. The optical THz generation are divided into two categories: THz generation by femtosecond laser pulses generating an ultrafast photocurrent in a photoconductive emitter using electric-field carrier acceleration, and the second, THz generation by non-linear optical effects such as, electro-optic rectification (EOR) where the passage of an intense laser pulse generates a quasi-DC nonlinear polarization where electrons are being pushed by a sinusoidally-oscillating force, and difference-frequency generation (DFG) which involves injecting two lasers into a non-linear crystal to generate a wide tunable frequencies in the THz domain [26, 27, 28, 29, 30, 31, 32]. These THz sources are crucial for several application domains, such as security, medical imaging and wireless networks as previously mentioned. Nevertheless, despite the identification of various possible applications, the spectral coverage of these sources does not meet all the different applications [33]. The limitations are related to source power, lack of compactness and prize, although researches to find more versatile THz sources continue.

In the other hand, a lot of efforts have been made to realize photonic components able to detect THz radiations efficiently [34, 35]. Versatile THz waves detectors have been considered as something of a "holy grail" for many years [27]. The advent of mode-locked femtosecond lasers in the 1990s has pushed the development of THz time-domain spectroscopy (THz-TDS) [36]. One of the first THz detectors set-up is illustrated in figure1.2-A, where a femtosecond laser source, corresponding to a Ti:sapphire laser emits a pulsed light beam which is splitted into two probe pulses

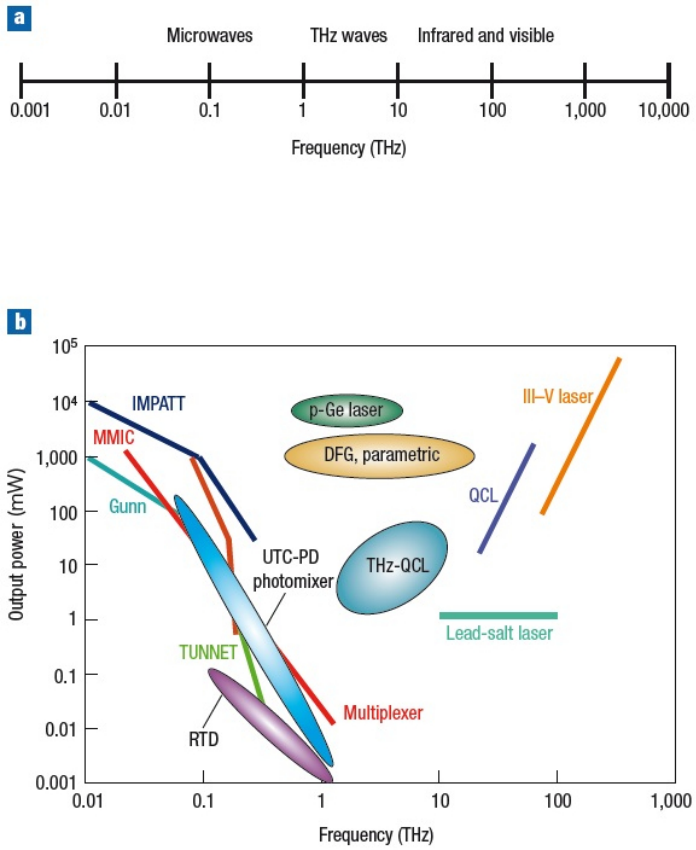

Figure 1.1 – *(a) A schematic showing the THz gap within the electromagnetic spectrum. (b) THz emission power as a function of frequency; IMPATT diode stands for impact ionization avalanche transit-time diode, MMIC stands for microwave monolithic integrated circuit, TUNNET stands for tunnel injection transit time and the multiplexer is an Schottky barrier diode (SBD) frequency multiplier. Ovals denote recent THz sources. The values of the last two are indicated by peak power; others are by C.W. power [26].*

beams (excitation and detection). The excitation pulses probe pulse reaches the THz emitter such as a photoconductive antenna, a semiconductor wafer or a nonlinear crystal, where the excitation pulses is transformed into THz electromagnetic pulses. These THz pulses radiation are propagated in free space and focused onto an ultrafast detector, such as a photoconductive switch [37] or an electro-optic sampling crystal [38]. The THz radiation induced a transient birefringence in the sensor crystal that field-induced a modulation in the index of refraction in the sample. This modulation is detected using the second pulses probe pulse after passing through a time-delay stage and polarization-resolving optics [39].

The detector measures the electric-field amplitude of the electromagnetic waves. Some examples are presented in figure1.2-B, where the THz pulses emitted from a p-InAs [40] or an organic DAST ($diethylaminosulfurtetrafluoride$) crystal [41] are collimated and then focused into a low-temperature-grown GaAs (LT-GaAs) photoconductive antenna probed with a 1.56 μm probe laser [42]. Figure1.2-C shows

their Fourier-transformed spectra on a logarithmic scale in the frequency domain.

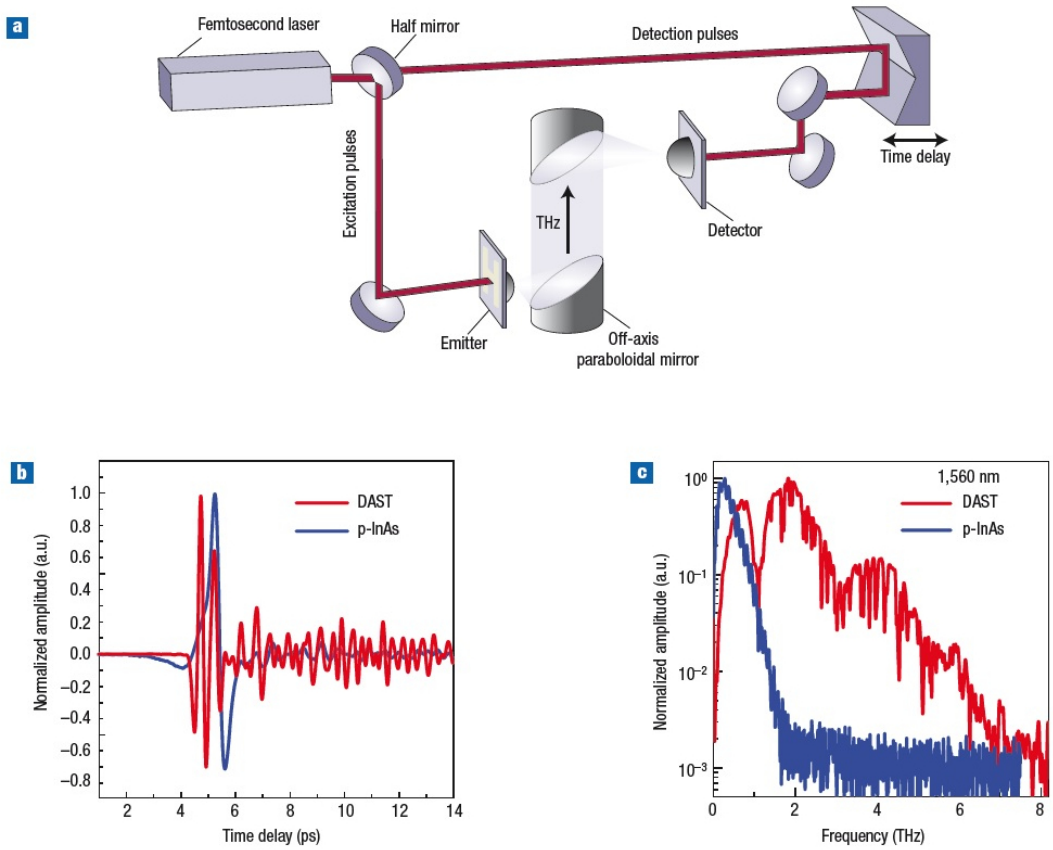

Figure 1.2 – *(a) Schematic of the THz-TDS optics set-up. (b) Examples of THz pulses emitted from a p-InAs and a DAST and detected by LT-GaAs photoconductive antenna. (c) Corresponding Fourier-transformed spectra on a logarithmic scale in the frequency domain.*

This THz-wave generation and detection system in the time domain using a femtosecond laser opened up the interest of 2D measurements and spatio-temporal coupling of few-cycle THz pulses. It has been implemented in the conventional THz detection configuration set-up with the use of an electro-optic sample. It allows to measure the electric field distribution of the THz pulses by using a charge coupled device (CDD) camera to catch the spatial distribution of the probe beam [43]. These two approaches demonstrate the possibility of THz detection and imaging for the first time. However, they cannot easily be implemented using a low-power femtosecond laser: an amplified laser system is necessary to obtain high pump power required to achieve a significant modulation of the birefringence of the sensor crystal in order to change the refraction index of the non-linear material. In addition, the limitations are related to the lack of compact source, prize and mainly in THz generation efficiency that is again conditioned by the femtosecond laser pulse.

All these last inconveniences were overcomed with the advent of the THz quantum cascade laser (QCL) in 2002 [33, 44]. This THz source highly detectable even with a microbolometer focal plane array, which was compatible with real-time read-

out at video rate [45] open up the possibility to obtain THz videos. Nowadays, four different technology platforms have been used as the basis for pixel arrays in commercial THz cameras: III-V high-electronmobility transistors (HEMTs), silicon complementary metal–oxide–semiconductor (CMOS) circuits, microbolometers and pyroelectric devices which operate at room temperature and with video-rate read-out. Some others specifications are presented in figure1.3.

The major issues that refrains the different focal-plane array technologies presented in figure1.3 concern: the fairly expensive cost, the slow speed modulation rates (frame rates), the lack of compactness and the narrow operating range of THz frequencies.

	CMOS	GaAs HETEROSTRUCTURE	MICROBOLOMETER	PYROELECTRIC
Number of pixels	32 x 32	64 x 64	320 x 240	320 x 320
Pixel size (µm)	80	1500	50	75
Operating range (THz)	0.3 – 1.3	0.05 – 0.7	0.6 – 4.0	0.1 and up
NEP ($nW \cdot Hz^{-1/2}$)	0.4	1	0.03	13
Responsivity (kV/W)	140	50	18 (at peak)	N/A
Frame rate (fps)	30	24	25	50

Figure 1.3 – *A summary of the typical specifications of four types of commercially available focal plane arrays that can be used to visualize THz beams. Experimental comparisons of some of these cameras has been discussed in [46].*

Besides the different mentioned approaches to control THz waves radiations are the metasurfaces. Metasurfaces are passive components that offer in particular a versatile platform to manipulate the phase, the polarization or the intensity of electromagnetic waves [47, 48, 49, 50, 51, 52, 53]. Metasurfaces are composed of an array of metallic and/or dielectric resonators settled with a subwavelength period onto a surface and has attracted a great attention due to the unlimited ways of easy fabrication process. However, those metasurfaces operate in a given THz frequency which is the main limitation of this technology. To overcome this obstacle, active components such as hybrid component have been studied. The dynamical control of their electromagnetic properties has been explored by tuning their resonances with external stimuli, such as electrical, thermal or mechanical actuators [54, 55]. However, these approaches offer limited spectral and modulation actuations since the spectral shift for the resonances is accompanied by a decreasing efficiency. So far, all-optical modulators that have been realized consider in particular Mie or plasmonic resonators [56, 57, 58].

All those previous limitations lead to the research of a new versatile approach. In this context, we propose photo-generated metasurfaces. This attractive approach yields to a versatile and fully reconfigurable device operating over a wide range of frequencies [59, 60, 61]. In this approach, the permittivity of a semiconductor is locally modified by applying an optical excitation which is often a near infrared

(IR) laser pump. The optical management of the permittivity is attributed to the shift of the plasma frequency in the THz range that depends on the photo-carrier density. Photo-generated patterns of controlled size, shape and spacing have for example been demonstrated with a spatially varied IR pump [62, 63]. Ideally, these photo-generated patterns can be properly designed to achieve an optimal modulation of the THz signals [64].

The main advantages of photo-generated metasurfaces allow us to introduce dynamically metallic patterns in a way that we can realize the previous structures by using photo-generation process without lost in term of efficiency. However, the major issue that refrains the realization of on-chip integrated photo-generated components concerns the high pump irradiance attaining hundreds of kW/cm^2 [65, 66] required to achieve a significant dynamical control of THz waves over a wide range of frequencies with high-speed modulation rate up to the MHz range.

1.3 Indium Arsenide platform for the next-generation of THz detection devices

The choice of the new promising semiconductor platform is crucial for the development of THz detectors operating at very low pump power and at high-speed modulation rate. Nowadays, the major issue that refrains the realization of on-chip integrated photo-generated components concerns the high pump irradiance required to achieve a significant modulation of the THz waves. The challenge is to find a material suitable for efficient photo-generation and capable to perform a larger photo-carrier diffusion process, both at room temperature. In this context, silicon is a material widely used for on-chip photonics, however, its indirect band gap restrains an efficient photo-generation [67, 68]. In the research of direct band gap semiconductors, photo-generated surfaces made of gallium arsenide (GaAs) have been realized with pump irradiance attaining hundreds of kW/cm^2 [66, 65]. However, these high irradiances reached with pulsed lasers are incompatible with integrated components on-chip, since they are sources that deliver low intensity irradiances in the continuous wave (CW) regime.

Regarding the conventional THz detectors, they are typically made of GaAs for photoconductive switch or electro-optics crystals $(ZnTe, GaSe, DAST)$ [69, 38, 70, 71, 72, 73]. These materials demand a high amount of energy to induce the transient birefringence modulation that would allow to detect the THz waves by changing the optical refraction index of the material. The high pump power demanded is due to the fact that they are materials with a wide energy gap and with very short carrier life-time. This two features counterproductive the photo-generation process. The high pump energy has been conventionally supplied by a pulsed laser femtosecond probe, that makes this technology inefficient since these lasers are fairly expensive, have lack of compactness and can produce a narrow THz operating range.

It has been reported that some narrow band-gap III-V semiconductors, such as Indium Arsenide (InAs) after ultra-fast photo-generation of charge carriers, can emit THz waves differently owing to their high electron mobility. InAs radiates THz waves mainly by photo-carrier transport driven by the photo-Dember field [69]. InAs has been reported to generate THz waves with intensity one order of magnitude higher than those of wide band-gap semiconductors such as InP and GaAs. These physical

particularity features of narrow-gap semiconductors with high electron mobility at room temperature lead us to explore the potential of photo-generated metasurfaces based on InAs to control fast and efficiently the THz radiation. We bring to the light the InAs material because it was declared as a material not suitable for THz detection, since its high intrinsic carrier concentration at room temperature does not allow to obtain a tuneability of the plasma frequency for frequencies above ≥ 1.5 THz [74].

Before concluding, we propose the undoped InAs material as a candidate platform for the next-generation of THz detectors devices [75, 76]. Since, InAs is a material that allows to have versatile tunability with low-pump irradiance at room temperature and it is compatible with CMOS technology making them promising candidates for future commercial applications. Recent works have demonstrate the use of the InAs material in different kind of applications such as [77, 78, 79, 80, 81], demonstrating that the InAs material allow to be easy manipulated and manufactured with high quality allowing to be easily integrated into the current technology with the classical recipes of fabrication available in clean room laboratories or industries.

1.4 Thesis motivations

Metasurfaces are static geometric structures. We know how to design and manufacture them easily but it is difficult to dynamically modify their electromagnetic properties making its fixed THz response inefficient. Photo-generated metasurfaces mean that we can dynamically change their geometry in real-time. In this scenario, we can change the THz beam reflected or transmitted in real-time and at high-speed modulation rate. Nevertheless, the holographic technique linked to the classical photo-generated metasurface technology is a device called spatial light modulator (SLM). SLM allows to tune by liquid crystal or moving mirrors from an incoming IR light beam to design dynamic structures on the semiconductor material used as a screen to obtain any kind of transmitted or reflected THz beam. However, this holographic system is fairly expensive: it cost around twenty thousand euros, it is not compact and is slow because it has a time delay rate up to 10kHz (one hundred milliseconds).

In the conventional photo-generated metasurfaces approach, several issues must be bypassed in terms of high pump power, modulation rate, fairly expensive cost, lack of compactness and the operating range of THz frequencies before this approach might be implemented in the application domain. Consequently, these issues represent one of the main motivation to be investigated and bypassed in this thesis in terms of low-pump irradiance, faster modulation rate, costless, compactness and with a high versatility able to address a wide range of frequencies in order to accelerate the progress of non-destructive THz systems.

As a general motivation, bring to light a solution to reduce the high laser pump required to create fast and efficiently THz devices at room temperature would permit to make this technology compact, and to unificate this technology with the conventional electronics by its integrable and adaptable low-pump irradiance. This low-pump irradiance corresponds to a compact and costless conventional continuous wave (CW) laser, which is able to tune the semiconductor material properties from a non-metallic state to a metallic one. This material versatility will allow to print

optically integrated photo-generated circuits totally reconfigurables in real time and to manufacture fastly and efficiently on-chip devices. In addition, this versatile manufacture will eventually allow to obtain structures with original shape properties that are unreachable with the standard recipes of clean room process. These original devices are environmentally favourable since they do not pollute to the environment and due to the fact that their platform or screen are reusable for optical printing of different applications. These benefits mentioned have been the research motivation of this thesis to bring solutions to all the necessities previously mentioned. This approach will contribute with a new point of view and with a new way to use the InAs for the THz detection technology.

1.5 Thesis objective

In this thesis, we figure out strategies to propose a fundamental new design of photo-generated metasurfaces that tackles the actual limitations of high pump fluences required to manufacture fastly and efficiently THz components. Photo-generated metasurfaces are photo-excited structures defined into a bulk to design a material by using photocarrier diffusion process and also on the surface to make the conventional flat components. This work reveals the crucial impact of the photocarrier diffusion to realize optimal metasurfaces for the control of THz radiations. This scientific insight allows to control efficiently and dynamically the THz waves over a wide range of frequencies with very low pump irradiances and with high-speed modulation rate up to the MHz range. This will be theoretically explained in Chapter 2 and the proof-of-principle of photo-generated metasurfaces with efficient broadband to detect THz light at different wavelengths is given in Chapter 3 to Chapter 5.

Chapter 2

Photo-generated metasurfaces at THz frequencies

2.1 Photo-generation process at THz frequencies 22
2.2 Interaction of the laser pump with the InAs slab 23
2.3 Photo-generation process 25
2.3.1 Optical absorption process 26
2.3.2 Optical generation process 27
2.3.3 Photo-generated carriers densities 27
2.3.4 Ambipolar transport equation 29
2.3.5 Excess carriers recombination rate 29
2.3.6 Excess carriers lifetime recombination 30
2.3.7 Photo-generated patterns distribution 33
2.4 Efficient implementation of the RCWA method 35
2.4.1 THz waves in TE polarization 35
2.4.2 THz waves in TM polarization 36
2.5 Results and discussion 37
2.5.1 Thin films 38
2.5.2 Thick films 39
2.5.3 Ultra-thick films 42
2.6 Summary 44

Active metasurfaces have draw attention due to the unlimited ways of controlling electromagnetic radiations. In this chapter, we will theoretically study the THz electromagnetic properties of photo-generated metasurfaces in an InAs slab. We will use a spatially modulated optical pump in order to modify the permittivity. Those modifications are calculated by solving the ambipolar rate equation for the photo-carriers. This work reveals the crucial impact of the photo-carrier diffusion to realize optimal metasurfaces for the control of THz radiations. We will demonstrate that InAs is a promising semiconductor to manufacture THz devices. We will also demonstrate that low-pump irradiances in the continuous regime of only tens of W/cm^2 *is sufficient to modulate the absorption of the THz waves up to* 67% *on a broad frequency range from 1 THz to 3 THz. In the following sections, the THz electromagnetic properties of photo-generated metasurfaces in an InAs slab are presented.*

2.1 Photo-generation process at THz frequencies

In the photo-generation process at THz frequencies, the permittivity of a semiconductor is locally modified by applying an optical excitation which is often a near infrared (IR) laser pump [59, 60]. The optical management of the permittivity in the conducting layer is attributed to the shift of the plasma frequency (ω_p) in the THz range that depends on the photo-carrier density (N). Then, the photo-generated pattern can be properly designed to achieve an optimal modulation of the THz waves [62, 63, 64, 82, 76].

In this chapter, we theoretically investigate the excitation and the active control of the optical properties of photo-generated metasurfaces at THz frequencies. We reveal the crucial impact of the photo-carrier diffusion for the control of THz radiations inside of a metasurface. We discuss the modulation of the absorption coefficient for THz waves interacting with an InAs slab standing in air, as presented in figure2.1.

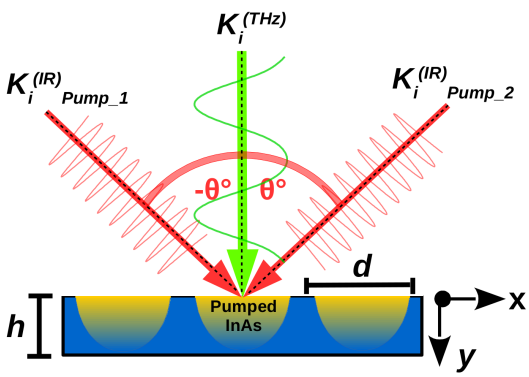

Figure 2.1 – *Schematic of the interference pattern produced by two IR tilted plane waves with incident angles $\pm\theta$. The pumped InAs slab of thickness h and periodicity d is enlightened by a THz plane wave at normal incidence.*

We consider an intrinsic InAs slab of thickness h irradiated by an IR pump of wavelength $\lambda_{IR} = 815\,nm$ corresponding to a conventional laser pump. At this wavelength, the relative permittivity of InAs is $\epsilon_{IR}^{InAs} = 13.64 + 3.3i$ [83]. To photo-generate grating patterns at THz frequencies, the IR pump is splitted into two tilted plane waves of respective incident angles $\pm\theta$ that propagate the half of the incident pump irradiance denoted Φ_0.

In this scenario, the electromagnetic properties of the slab are examinated for a photo-generated grating of variable pitch. This geometry is shown to support several absorption mechanisms that critically depend on the thickness of the InAs slab. The diversity of photonics effects (Fabry-Perot resonances, complex dielectric-metal or metal-metal grating absorption and epsilon near-zero (ENZ) absorption [84, 85, 86, 87]) is exploited to create broad-band or resonant modulations that depend of the polarization of the THz waves. To demonstrate theoretically the excitation and the active control of the optical properties of photo-generated metasurfaces at THz frequencies, we detail the steps to follow, as presented below:

1. **Interaction of the laser pump with the InAs slab**: We develop a theoretical analysis for the resolution of the Maxwell's equations in the case of a

periodic pump excitation.

2. **Photo-generation process**: The theoretical study was performed by using a home-made multiphysics code based on the Finite Difference Method (FDM) that solves the ambipolar transport equation.
3. **Efficient implementation of the RCWA method**: We study the electromagnetic properties of an InAs slab, whose permittivity has been optically modified by a photo-generation process, by using the Rigorous Coupled Wave Analysis (RCWA) that solves the electromagnetic problems at the THz frequencies. We track the evolution of the THz absorption peaks for both polarizations (TE and TM) when the grating period is changing.

2.2 Interaction of the laser pump with the InAs slab

The interaction of the IR laser pump with the semiconductor in order to photo-generate grating patterns in the conducting layer at THz frequencies begins from Maxwell's equations, where the current density and the charge density are not considered:

$$\nabla \cdot \vec{D} = 0 \tag{2.1}$$

$$\nabla \cdot \vec{B} = 0 \tag{2.2}$$

$$\nabla \times \vec{E} = -\frac{\partial \vec{B}}{\partial t} \tag{2.3}$$

$$\nabla \times \vec{H} = \frac{\partial \vec{D}}{\partial t} \tag{2.4}$$

In these equations there are four macroscopic fields where $\vec{E}$ is the electric field, $\vec{H}$ the magnetic field, $\vec{D}$ the dielectric density, and $\vec{B}$ the magnetic density. The material equations related to linear, homogeneous and isotropic media:

$$\vec{D} = \varepsilon_0 \varepsilon_r \vec{E} \tag{2.5}$$

$$\vec{B} = \mu_0 \mu_r \vec{H} \tag{2.6}$$

where ε_0 and μ_0 are the vacuum electric permittivity and the vacuum magnetic permeability. $\varepsilon_r = \varepsilon' + i\varepsilon''$ is the relative permittivity of the medium, μ_r is the relative permeability which is equals 1 for nonmagnetic media. For a harmonic regime, the Maxwell's equations can be written as it follows:

$$\nabla \times \vec{E} = -i\omega \vec{B} = -i\omega\mu_0 \frac{\partial \vec{H}}{\partial t} \tag{2.7}$$

$$\nabla \times \vec{H} = i\omega \vec{D} = i\omega\varepsilon_0\varepsilon_r \frac{\partial \vec{E}}{\partial t} \tag{2.8}$$

where ω is the angular frequency of the wave. These equations describe the propagation of transverse electric (TE) or transverse magnetic (TM) waves.

In the system under study, the InAs slab of thickness h is enlightened with a laser pump whose radiation propagates in TE-polarization, corresponding to a field perpendicular to the plane of incidence, and therefore parallel to the interface of

the InAs slab. The development of the Maxwell's equations (Eq.2.7 and Eq.2.8), considering that the propagation in the z-direction is infinity and knowing that (E_x, E_y and $H_z = 0$), yields to the equations that describe the TE propagation waves are:

$$\partial_y E_z = -i\omega\mu_0 H_x \tag{2.9}$$

$$\partial_x E_z = i\omega\mu_0 H_y \tag{2.10}$$

$$\partial_x H_y - \partial_y H_x = i\omega\varepsilon_0\varepsilon_r E_z \tag{2.11}$$

In this case, the central coefficient of the TE-polarization is E_z. We replace Eq.2.9 and Eq.2.10 in the Eq.2.11 to obtain the following expression:

$$\partial_x^2 E_z + \partial_y^2 E_z + k_0^2\varepsilon_r E_z = 0 \tag{2.12}$$

where $k_0 = \omega/c = 2\pi/\lambda$ is the wave-number, $\varepsilon_r = n_i^2$ with n_i as the refractive index in each medium. The propagation wave-vector ($\vec{k}$) is distributed along the x and y directions. α is the in-plane propagation wave-vector and $\beta = \sqrt{k_0^2 n_i^2 - \alpha^2}$ is the propagation wave-vector along the y-direction. The development of Eq.2.12 yields to

$$\partial_y^2 E_z + (k_0^2 n_i^2 - \alpha^2)E_z = 0 \tag{2.13}$$

To photo-generate grating patterns, we use an interference pattern produced by two tilted plane waves irradiation with incident angles $\pm\theta$. The components of the two wave-vectors ($\vec{k_1}$) and ($\vec{k_2}$), presented in a schematic in the figure2.2, may be written:

$$\begin{aligned} \alpha_1 &= -k_0 sin(\theta) = -\alpha_2 = \alpha_0 \\ \beta_1 &= -k_0 cos(\theta) = \beta_2 = \beta_0 \end{aligned} \tag{2.14}$$

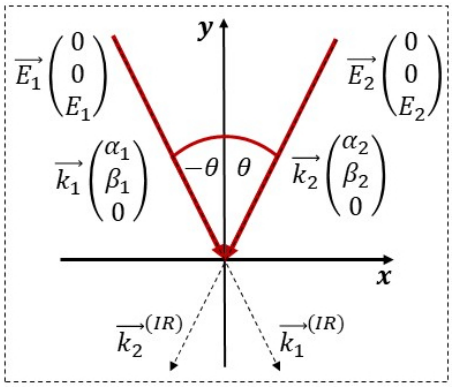

Figure 2.2 – *Description of the electric field interference pattern produced by two tilted plane waves of the respective incident angles $\pm\theta$.*

The equations that describe the electric field interference pattern produced by two tilted plane waves irradiations, are given by:

$$\begin{aligned} E_{IR}(x,y) &= E_1 + E_2 \\ E_{IR}(x,y) &= E_0 \exp^{i\alpha_0 x} \exp^{i\beta_0 y} + E_0 \exp^{-i\alpha_0 x} \exp^{i\beta_0 y} \\ E_{IR}(x,y) &= 2E_0 cos(\alpha_0 x) \exp^{i\beta_0 y} \end{aligned} \tag{2.15}$$

where the expression of the IR electric field intensity is:

$$\begin{aligned} I &=\mid E_{IR}(x,y) \mid^2 = E_{IR}(x,y)E_{IR}(x,y)^* \\ I &= 2E_0(1+cos(2\alpha_0 x)) \end{aligned} \tag{2.16}$$

with a periodic condition $2\alpha_0 x = 2\pi x/d$ where d is the spatial period along the x-direction. This grating pitch is correlated to the angle θ by the following expression: $d = \lambda_{IR}/(2\sin\theta)$. This interferential process allows us to periodically vary the IR electric field intensity within the InAs slab:

$$\mid E_{IR}(x,y) \mid^2 = 2Z_0\Phi_0 \mid E(y) \mid^2 (1+cos(2\pi x/d)) \tag{2.17}$$

where $E(y)$ is a normalized total electric field calculated using the Scattering Matrix Method (as it is illustrated in Appendix A), and Z_0 is the vacuum impedance. Figure2.3-A illustrates that the electric field distributed into the InAs layer reaches a maximal penetration distance of only $1\mu m$. An interference pattern pitch describes the non-homogeneous extinction of the electric field distributed into the InAs layer. We observe that the E-field varies along the x-direction as the pump modulation does. In contrast, the E-field reaches only $1\mu m$ in the y-direction, as presented in figure2.3-B.

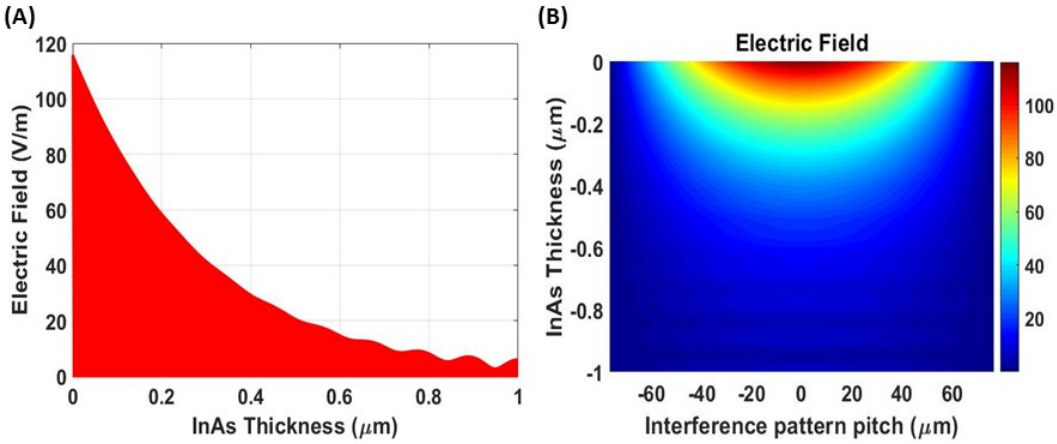

Figure 2.3 – *(A) Maps of the electric field distribution in the InAs layer (along the y-direction) and (B) description of the non-homogeneous extinction of the electric field along the x-direction. Both for a pitch $d = 153\mu m$, a thickness $h = 1\mu m$ and for a pump fluence of 50 W/cm^2.*

In the following section, we extend our study to include the photo-generation process. It will be devoted to the comprehension of the free carrier generation and dynamics such as carrier diffusion and recombination lifetime, effects that will play a crucial role for realizing optimal metasurfaces for the control of the THz waves radiations.

2.3 Photo-generation process

This section deals with the photo-generation process in the InAs slab. We present the optical absorption, the generation process, the mechanisms of transport and

recombination of the free-carriers.

2.3.1 Optical absorption process

We start with the optical absorption process which is based on the interaction between photons and electrons. When the photon energy is higher than the band-gap energy ($E_g^{InAs} = 0.354eV$), it can excite free-electrons from the valence band to a free-state into the conduction band (the energy of the laser pump with a wavelength of $\lambda_{IR} = 815nm$ is equal to $h\nu = 1.5eV$). In the case of the InAs slab, the transition corresponds to a direct band-gap material due to the fact that the minimum of the conduction band and the maximum of the valence band coincide in the space of the wave vectors, as presented in figure4.1. Consequently, the interaction between photons and electrons results in the absorption coefficient (α). In direct band-gap semiconductors without any excitonic effect which is justified for InAs, the absorption coefficient can be approximated by:

$$\alpha(h\nu) = A(h\nu - E_g)^{1/2} \tag{2.18}$$

where A is a constant. In addition, the intensity of the electromagnetic wave that passes through the direct gap semiconductor is given by:

$$I = I_0 \exp(-\alpha y) \tag{2.19}$$

where I_0 is the intensity of the incident beam and y the thickness of the semiconductor layer. The penetration depth of monochromatic radiation into a semiconductor is found to be (α^{-1}). In the InAs slab, the high absorption coefficient $\alpha_{InAs} = 67682(cm^{-1})$ [88] is indeed accompanied by a short penetration distance for the pump $L_p^{InAs} = 147nm$ at a wavelength $815nm$, as presented in figure2.3. This means that the active thickness of the InAs, where more than 99% of the carriers are photo-generated, reaches only $1\mu m$ (corresponding approximately to 10Lp; obtained by the E-field penetration distance previously presented in figure2.3-A).

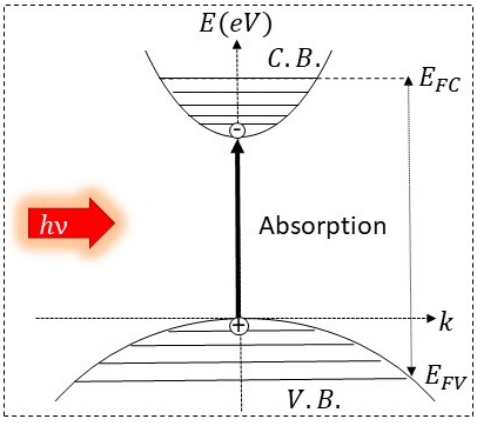

Figure 2.4 – *Schematic of the absorption process of the InAs material; direct band-gap semiconductor, optically pumped. The inter-bands electrons transitions from the valence-band (V.B.) to the conduction-band (C.B.) are performed with constant k.*

2.3.2 Optical generation process

The optical generation process of electron-hole pairs occurs when the InAs slab is illuminated with photons with energy higher than E_g. We assume here a 100% quantum efficiency by assuming that a photon generates an electron-hole pair. The generation term G^{op} is related to the electric field intensity [89] previously presented in equation2.17 by:

$$G^{op}(x,y) = \pi/(hcZ_0)Im(\varepsilon_{IR}) \mid E_{IR}(x,y) \mid^2 \tag{2.20}$$

where h is the Planck constant, c the celerity of light, (ε_{IR}) the relative complex permittivity of the semiconductor at pump wavelength (λ_{IR}). At $\lambda_{IR} = 815nm$, the respective imaginary permittivity of InAs is $Im(\epsilon_{IR}^{InAs} = 3.3)$.

2.3.3 Photo-generated carriers densities

After the photo-generation of the free carriers in the semiconductor, the evolution of this non-equilibrium electron-hole gas density within the intrinsic InAs slab is driven by the electrostatic potential and the diffusion phenomena. Figure2.5 illustrates the photo-generated carrier density distribution in an InAs semiconductor after the photo-geneation of free carriers. At $t = 0(s)$, the electron-hole carrier density is the same due to the fact that each photon generates an electron-hole pair $\Delta n(x,0) = \Delta p(x,0)$. For the sake of simplification, we consider a constant carrier distribution at $t = 0(s)$ as represented by the dashed line in Figure2.5. At $t \neq 0(s)$, the electrons with a reduced effective electron mass ($m_{eff}^{InAs} = 0.023m_0$; where m_0 is the electron mass in the vacuum) which consequently have a high mobility value ($\mu_n^{InAs} = 33000(cm^2V/s)$) diffuse faster than holes (see figure2.5) which have a reduced mobility value ($\mu_p^{InAs} = 460(cm^2V/s)$) due to their high effective mass value ($m_{eff}^{InAs} = 0.41m_0$).

The difference in mobilities ($\mu_n \gg \mu_p$) results in the existence of a space charge density (ρ) and consequently, an internal electric field (E_i). This field accelerates the slowest carriers (holes) and decelerates the fastest carriers (electrons). Subsequently, in order to link the electrostatic potential V (in this case the electric field E_i) to the space charge density distribution (ρ), we use the Poisson equation:

$$\nabla^2 V(y) = -\frac{\rho(y)}{\varepsilon} = -\frac{d^2E_i(y)}{dy^2} = -\frac{e}{\varepsilon}(p - n + N_D - N_A) \tag{2.21}$$

where e is the elementary charge, n and p are the free electron hole density, N_D and N_A are the concentration of ionized donors and acceptors and the ε is the dielectric permittivity of the InAs material ($\varepsilon = \varepsilon_0\varepsilon_R$ where ε_R is the relative permittivity).

We can assume that the electrical neutrality is preserved during photo-generation since the free carriers of the material will tend to drift in opposite directions

$$\nabla \cdot E_i = \frac{e(p-n)}{\varepsilon} = \frac{\partial E_i}{\partial t} \approx 0 \tag{2.22}$$

in a very short time corresponding to the dielectric relaxation time $\tau_{diel} = \varepsilon/\sigma \approx 10^{-12}(s)$ [89], where σ is the conductivity of the material. Therefore, we can not have an excess charge in the material when it is illuminated and the medium will remain electrically neutral ($\Delta n = \Delta p$).

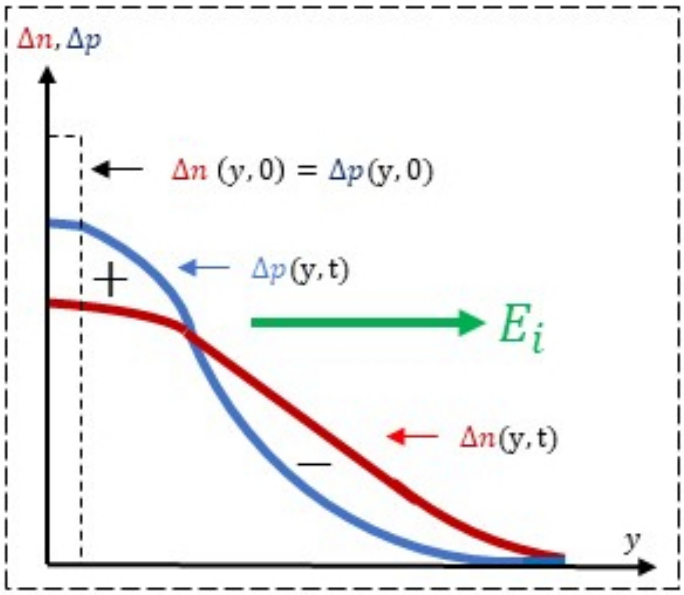

Figure 2.5 – *Schematic of the photo-generated carrier distribution in an optically excited InAs slab. E_i represents an internal field that results from the difference in mobility between electrons and holes.*

To describe carrier transport phenomena, we use the continuity equations for electrons and for holes, which govern the condition of dynamic equilibrium of the charge carriers in the semiconductor [90]. They give the relation between the currents, the generation and recombination mechanisms and the spatial and temporal distribution of free charge carriers:

$$D_n \frac{\partial^2 n}{\partial y^2} + \mu_n (E \frac{\partial n}{\partial y} + n \frac{\partial E}{\partial y}) + G^{opt} - R = \frac{\partial n}{\partial t} \tag{2.23}$$

$$D_p \frac{\partial^2 n}{\partial y^2} - \mu_p (E \frac{\partial n}{\partial y} + p \frac{\partial E}{\partial y}) + G^{opt} - R = \frac{\partial n}{\partial t} \tag{2.24}$$

If we multiply Eq.2.23 by $\mu_n n$, and multiply Eq.2.24 by $\mu_p p$, and add the two equations. The result of this addition gives:

$$(\mu_n n D_p + \mu_p p D_n) \frac{\partial^2 n}{\partial y^2} + (\mu_n \mu_p)(p - n) E \frac{\partial n}{\partial y} + (\mu_n n + \mu_p p)(G^{opt} - R) = (\mu_n n + \mu_p p) \frac{\partial n}{\partial t} \tag{2.25}$$

if we divide Eq.2.25 by the term $(\mu_n n + \mu_p p)$, this equation becomes:

$$D_a \frac{\partial^2 n}{\partial y^2} + \mu_a E \frac{\partial n}{\partial y} + G^{opt} - R = \frac{\partial n}{\partial t} \tag{2.26}$$

This ambipolar transport equation2.26 describes the behavior of the excess electrons and holes in time and space. The parameter D_a is called the ambipolar diffusion coefficient:

$$D_a = \frac{\mu_n n D_p + \mu_p p D_n}{\mu_n n + \mu_p p} \tag{2.27}$$

and μ_a is called the ambipolar mobility:

$$\mu_a = \frac{(\mu_p \mu_n)(p-n)}{\mu_n n + \mu_p p} \tag{2.28}$$

The Einstein relation relates the mobility and diffusion coefficient by

$$D_{(n,p)} = \mu_{(n,p)} \frac{kT}{e} \tag{2.29}$$

where k is the Boltzmann constant. Using these relations, the ambipolar diffusion coefficient may be written in the form

$$D_a = \frac{D_n D_p (n+p)}{D_n n + D_p p} \tag{2.30}$$

2.3.4 Ambipolar transport equation

Within the undoped-InAs slab, the IR pump photo-generates electron-hole pairs whose density N is governed by the ambipolar transport equation [91]

$$\frac{\partial N}{\partial t} = G^{op} - \frac{N}{\tau_r} + D_a \Delta N \tag{2.31}$$

as we consider an intrinsic InAs slab ($n_i = n_0 = p_0$), the mobility (μ_a) and the ambipolar diffusion coefficient (D_a) are found to be:

$$\mu_a = 0 \tag{2.32}$$

$$D_a = \frac{2 D_n D_p}{(D_p + D_n)} \tag{2.33}$$

where $D_{(n,p)}$ represent respectively, the diffusion coefficient of electrons and holes connected by the Einstein relation (Eq.2.29). The ambipolar diffusion coefficient in the undoped-InAs material is $D_a = 23.5 cm^2 s^{-1}$ at room temperature (300K) [89].

We remark that, the ambipolar transport equation (Eq.2.31) is governed by the minority carriers. This is due to the fact that the photo-carriers created by photo-generation process diffuse together $\Delta n(x,t) \approx \Delta p(x,t)$ which corresponds to the ambipolar diffusion. In this context, the photo-carrier with slow mobility value (normally the minority carrier (holes)) provoke a deceleration of the ambipolar diffusion. The majority carrier density is not affected by the irradiation, except under very strong excitation as we will present in the next section. In the following section, we present the theory of recombination of the photo-generated excess carriers.

2.3.5 Excess carriers recombination rate

Within the InAs material, the pump creates electron-hole pairs. The excess electrons and holes recombine in pairs, so the recombination rate (R) must be equal: $R_n = R_p$. As previously mentioned, the InAs is subjected to a non-external electric field polarization, therefore, the photo-generated free carriers in the InAs slab are animated like the molecules of a gas in a chamber with a Brownian motion. Using the

concept of collision model (κ_r), we can assume that the rate of pair recombination obeys:

$$R = \kappa_r np \tag{2.34}$$

where, R is the recombination rate of electrons and holes under non-equilibrium, $n = n_0 + \Delta n$ and $p = p_0 + \Delta p$, with n_0 and p_0 as the carrier concentrations at the equilibrium. Then, the recombination rate at the equilibrium is represented by:

$$R_0 = \kappa_r n_0 p_0 = \kappa_r n_i^2 \tag{2.35}$$

We assume neutrality condition $\Delta n = \Delta p$, therefore, the total recombination rate is given by:

$$R_T = R - R_0 = \kappa_r (np - n_i^2) = \kappa_r \Delta n (n_0 + p_0 + \Delta n) \tag{2.36}$$

where, R_T is the total recombination rate of excess carriers. We can write the equation2.36 in the form:

$$R_T = \frac{\Delta n}{\tau(\Delta n)} = \frac{\Delta p}{\tau(\Delta p)} \tag{2.37}$$

with

$$\tau(\Delta n) = \frac{1}{\kappa_r (n_0 + p_0 + \Delta n)} \tag{2.38}$$

where $\tau(\Delta n)$ is the carrier lifetime in an optically excited semiconductor and it corresponds to τ_r in the Equ.2.31.

In the following section, we are interested in studying the recombination lifetime of the excess carriers. The objective is to present each recombination mechanisms that are activated by the photo-generation process under different injection levels. We discuss how the excess carriers by using the concept of collision model (κ_r) are subjected to different types of recombination conditions.

2.3.6 Excess carriers lifetime recombination

The recombination mechanisms of the photo-carriers in the InAs slab are:

1. **Shockley-Read-Hall (SRH) recombination**: Recombination mechanisms introduced by crystalline defects and impure atoms (Fig.2.6-A).
2. **Radiative recombination**: Recombination mechanisms introduced by the excess of energy which is released in the form of a photon of energy close to the energy gap (Fig.2.6-B).
3. **Auger recombination**: Recombination mechanisms introduced by the excess energy released during a recombination which is transferred to another electron or other hole staying in the same band (Fig.2.6-C).

2.3.6.1 Shockley-Read-Hall (SRH) theory of recombination:

In a perfect semiconductor material, the electronics energy states do not exist within the bandgap. However, in a real semiconductor, defects and impure atoms appear within the crystal, creating the apparition of discrete electronic states or impurity energy bands within the bandgap. These defects can momentarily trap the electrons (or holes) before returning them to the conduction band (or the valence band). They can also play the role of recombination center, capturing both

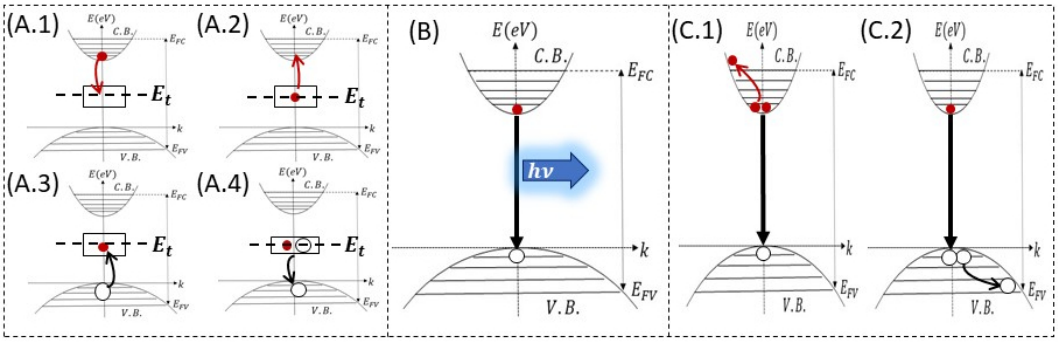

Figure 2.6 – *Description of the different photo-carriers recombination mechanisms: (a) SRH recombination, (b) Radiative recombination and (c) Auger recombination.*

electrons and holes with almost equal probability and causing the electron-hole pair recombination.

The Shockley-Read-Hall (SRH) theory of recombination assumes that a single recombination center exists at an energy E_t within the bandgap. There are four processes in the SRH recombination (see figure2.6-A): The capture of an electron from the conduction band by a neutral empty trap, in Fig.2.6-(A.1), the emission of an electron back into the conduction band, in Fig.2.6-(A.2), the capture of a hole from the valence band by a trap containing an electron, in Fig.2.6-(A.3), and the emission of a hole from a neutral trap into the valence band, in Fig.2.6-(A.4). The concept of collision model κ_r; (which is part of the pair recombination in Eq.2.34), is considered in the relation between the capture constants (C) and the emission constants (E) which are found to be: $E_n = n'C_n$ for the electrons and $E_p = p'C_p$ for the holes. The free carrier concentrations (n' and p') are given by:

$$\begin{cases} n' = N_c \exp^{\frac{-(E_c - E_t)}{kT}} \\ p' = N_v \exp^{\frac{(E_v - E_t)}{kT}} \end{cases}$$

the capture constants can be expressed as $C_n = \nu_{th}\sigma_{cn}$ and $C_p = \nu_{th}\sigma_{cp}$:

$$\begin{cases} \tau_{n0} = \frac{1}{\nu_{th}\sigma_{cn}N_t} \\ \tau_{p0} = \frac{1}{\nu_{th}\sigma_{cp}N_t} \end{cases}$$

τ_{n0} and τ_{p0} are the fundamental life-time of the electrons and holes related to the following three terms: the thermal agitation speed of the carriers ν_{th}, the concentration in recombination centers N_t and their capture cross-section $\sigma_{cn,cp}$.

Then, the general SRH recombination rate (R_{SRH}) with a center of concentration N_t located at the gap level E_t with a section for capturing electrons σ_{cn} and for holes σ_{cp} is given by:

$$R_{SRH} = \frac{np - n_i^2}{\tau_{n0}(p + p') + \tau_{p0}(n + n')} \tag{2.39}$$

Consequently, the expression of the SRH lifetime recombination rate (τ_{SRH}), by considering the equation2.38, can be written as follows:

$$\tau_{SRH} = \frac{\Delta n}{R_{SRH}} = \frac{\tau_{n0}(p_0 + \Delta n + p') + \tau_{p0}(n_0 + \Delta n + n')}{n_0 + p_0 + \Delta n} \tag{2.40}$$

The injection level of the excess carriers allows us to simplify the expression of τ_{SRH} (where $\Delta n = \Delta p$):

— For a n-type semiconductor at low-pump injection ($n = n_0 + \Delta n \approx n_0$) and ($p = p_0 + \Delta n << n_0$): $\tau_{SRH} = \tau_{p0}$.

— For a p-type semiconductor at low-pump injection ($p = p_0 + \Delta n \approx p_0$) and ($n = n_0 + \Delta n << p_0$): $\tau_{SRH} = \tau_{n0}$.

— At high-pump injection for a n-type or p-type semiconductor, we find similar relations: $\tau_{SRH} = \tau_{n0} + \tau_{p0}$.

2.3.6.2 Radiative recombination

The radiative recombination needs an electron of the conduction band and a hole of the valence band. The excess electrons loss their energy spontaneously from the conduction band to the valence band, as presented in figure2.6-B, and the excess energy is released in the form of a photon of energy close to the energy gap E_g. The radiative recombination rate is related to the equation2.36, which depends on the concentration of the excess carriers photo-generated by the optical pump (where $\Delta n = \Delta p$):

$$R_{rad} = \kappa_r(np - n_i^2) \approx Bnp \tag{2.41}$$

where B is the InAs radiative bimolecular recombination coefficient and its value according to the state of the art at a temperature of $300K$ is $B_{InAs} = 8.5\text{x}10^{-11}(cm^3s^{-1})$ [92]. Furthermore, the expression of the radiative lifetime recombination rate (τ_{rad}) is found to be:

$$\tau_{rad} = \frac{\Delta n}{R_{rad}} = \frac{\Delta n}{B(n_0\Delta n + p_0\Delta n + \Delta n^2)} \tag{2.42}$$

The injection level of the excess carriers allows us to simplify the expression of τ_{rad} (where $\Delta n = \Delta p$):

— For a n-type semiconductor at low-pump injection ($n = n_0 + \Delta n \approx n_0$) and ($p = p_0 + \Delta n << n_0$): $\tau_{rad} = \frac{1}{Bn_0}$.

— For a p-type semiconductor at low-pump injection ($p = p_0 + \Delta n \approx p_0$) and ($n = n_0 + \Delta n << p_0$): $\tau_{rad} = \frac{1}{Bp_0}$.

— At high-pump injection for a n-type or p-type semiconductor, we find similar relations because the τ_{rad} is dependent on the level of injection: $\tau_{rad} = \frac{1}{B\Delta n}$.

2.3.6.3 Auger recombination

The Auger recombination process is a nonradiative process. The consideration of this type of recombination is necessary when high-pump injections are applied or when a heavily doped semiconductor is used. The Auger recombination is a three-particle recombination, where the recombination between an electron and hole, is accompanied by the transfer of energy to another free electron or hole, but not both for one event. The third particle involved in this process will eventually lose its energy by heating the crystal lattice. The Auger recombination rate is related to the equation2.36 as follows:

$$R_{Auger} = \kappa_r(np - n_i^2) \approx C_n n^2 p + C_p p^2 n \tag{2.43}$$

where C is the InAs Auger coefficient and its value according to the state of the art at a temperature of $300K$ is $C = 2.2\text{x}10^{-27}(cm^3s^{-1})$.

In addition, the expression of the Auger lifetime recombination rate (τ_{Auger}) is found to be:

$$\tau_{Auger} = \frac{\Delta n}{R_{Auger}} = \frac{\Delta n}{C_n(n_0+\Delta n)^2(p_0+\Delta n) + C_p(p_0+\Delta n)^2(n_0+\Delta n)} \tag{2.44}$$

The injection level of the excess carriers allows us to simplify the expression of τ_{Auger} (where $\Delta n = \Delta p$):

- For a n-type semiconductor at low-pump injection ($n = n_0 + \Delta n \approx n_0$) and ($p = p_0 + \Delta n << n_0$): $\tau_{Auger} = \frac{1}{C_p n_0^2}$.
- For a p-type semiconductor at low-pump injection ($p = p_0 + \Delta n \approx p_0$) and ($n = n_0 + \Delta n << p_0$): $\tau_{Auger} = \frac{1}{C_p p_0^2}$.
- At high-pump injection for a n-type or p-type semiconductor, we find similar relations because the τ_{Auger} is dependent on the level of injection: $\tau_{Auger} = \frac{1}{(C_n+C_p)\Delta n^2}$.

2.3.6.4 Effective lifetime of minority carriers (τ_{eff})

The last three presented recombination rate mechanisms are present in all semiconductors. In general, we use an effective recombination rate (R_{eff}) covering all the recombination rates mechanisms in volume of the semiconductor:

$$R_{eff} = R_{SRH} + R_{rad} + R_{Auger} \tag{2.45}$$

where the effective lifetime rate (τ_{eff}) is found to be:

$$\frac{1}{\tau_{eff}} = \frac{1}{\tau_{SRH}} + \frac{1}{\tau_{rad}} + \frac{1}{\tau_{Auger}} \tag{2.46}$$

In the following theoretical analysis of photo-generated metasurfaces, the radiative bimolecular recombination (B) and the Auger recombination (C) are neglected since the pump fluence is limited in order to keep the carrier density lower than $10^{17}\,cm^{-3}$. This is due to the fact that after $10^{17}\,cm^{-3}$ the ambipolar transport equation, given by Equ.2.31, becomes in a nonlinear differential equation since radiative and thermal recombinations cannot be neglected. At low-irradiance conditions, the radiative recombination BN^2 and the thermal recombination CN^3 have a minor impact in contrast to the photo-carrier recombination N/τ_r, and the ambipolar transport equation is a linear equation. In this scenario, we consider a mean recombination lifetime for the InAs material τ_r = 1x$10^{-7}(s)$. In addition, the neglected recombinations parameters (B and C) will be studied in the experimental work (next chapters) for a strong laser pump irradiation.

2.3.7 Photo-generated patterns distribution

For a continuous wave (CW) pump excitation, the carrier density reaches a steady state and Eq.(2.31) becomes:

$$\Delta N(x,y) - \frac{N(x,y)}{L_a^2} = -\frac{G^{op}(x,y)}{D_a} \tag{2.47}$$

where the ambipolar diffusion length defined by $L_a = \sqrt{D_a \tau_r}$ is equal to 15.32 μm for InAs when it is considered τ_r = 1x$10^{-7}(s)$. Since the IR electric field intensity is

a periodic function in the x-direction, it implies that both the source term $G^{op}(x,y)$ and the density of the photo-generated carriers are periodic functions (of period d) that decompose in Fourier series:

$$N(x,y) = \sum_{n=-\infty}^{\infty} N_n(y) e^{inKx}, \tag{2.48}$$

$$G^{op}(x,y) = \sum_{n=-\infty}^{\infty} G_n^{op}(y) e^{inKx} \tag{2.49}$$

where $K = 2\pi/d$ is the spatial frequency. In this framework, Eq.(2.47) becomes:

$$\frac{\partial^2 N_n(y)}{\partial y^2} - \Big((nK)^2 + \frac{1}{L_a^2}\Big) N_n(y) = -\frac{G_n^{op}(y)}{D_a} \tag{2.50}$$

We numerically solve the latter equation using a Finite Difference Method (FDM); (as it is illustrated in Appendix B), which allows us to take into account the non uniform spatial distribution of the source term within the InAs slab [93]. We observed that the distribution of photo-generated carriers is the same when surface recombinations are considered or not, however, the only difference is a decrease in the photo-generated carrier density value that we control increasing the pump irradiance. In this context, assuming that the surface recombinations are neglected at both interfaces and a periodic pump the carrier density reads:

$$N(x,y) = N_0(y) + N_1(y) cos(Kx) \tag{2.51}$$

These photo-generated carriers are responsible for the modification of the InAs electromagnetic properties at THz frequency. The optically induced variation of the relative permittivity is modeled with a Drude model:

$$\epsilon_{THz}(x,y) = \epsilon_\infty \Big(1 - \frac{\omega_p^2(N(x,y))}{\omega^2 + i\omega/\tau(N)}\Big). \tag{2.52}$$

At THz frequencies $\epsilon_\infty = 12.3$ for InAs semiconductor and the local plasma frequency ω_p is:

$$\omega_p(x,y) = \sqrt{N(x,y)e^2/(m_{eff}\epsilon_0\epsilon_\infty)} \tag{2.53}$$

The local modification of $\omega_p(x,y)$ allows us to change drastically the nature of InAs: in the areas where the plasma frequency ω_p is larger than the operating THz frequency, the dielectric semiconductor turns into a metal. In addition, the relaxation time $\tau(N) = \mu m_{eff}/e$ depends on the photocarrier concentration. The mobility μ and the effective mass m_{eff} are modified by the carrier density [94]. We extract these parameters from Hall Effect and reflectance measurements by the following empirical relations [95, 96, 97]:

$$\mu(x,y) = \frac{2}{1 + \sqrt{0.25 N(x,y) 10^{-17}}} \; (m^2 V^{-1} s^{-1}) \tag{2.54}$$

$$m_{eff}(x,y) = (0.02 + 2.3(N(x,y))^{0.335} \times 10^{-8}) m_0 \tag{2.55}$$

where m_0 is the electron's mass. Using Eq.(2.52), the relative permittivity at THz frequencies for InAs is numerically computed and reads:

$$\epsilon_{THz}(x,y) = \epsilon_0(y) + \Delta\epsilon(y)cos(Kx) \tag{2.56}$$

where $\epsilon_0(y)$ is the average permittivity in the x-direction and $\Delta\epsilon(y)$ represents the permittivity modulation.

In the following section, we extend our study to include the interaction of a THz wave radiation in both polarizations TE and TM over the photo-generated metasurface. We use a home-made RCWA code [98] to calculate the electromagnetic properties of the metasurfaces enlightened by a THz plane wave.

2.4 Efficient implementation of the RCWA method

The periodic distribution of photo-generated permittivity $\varepsilon_{THz}(x,y)$ induced in the InAs slab present gradual variations in both x and y-directions. This allows us to obtain a photogenerated grating diffraction configuration as illustrated in figure2.7. We use a home-made Rigorous Coupled-Wave Analysis (RCWA) code to calculate the electromagnetic properties of the metasurfaces illuminated by a THz plane wave. The absorption spectra are derived from the calculation of the reflexion (R) and transmission (T) coefficients using $A = 1 - R - T$ where A is the absorption coefficient. The scattering process are assumed negligible.

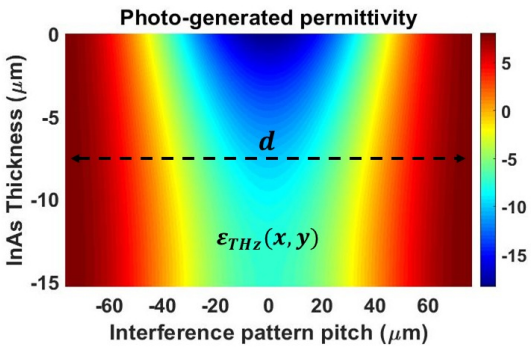

Figure 2.7 – *Map of the real part of the relative permittivity for a pitch* $d = 10La = 153\mu m$, *a thickness* $h = 15.3\mu m$ *at* $\lambda_{THz} = 15La = 230\mu m = 1.3THz$ *and for a laser pump irradiance of* $\Phi_0 = 50W/cm^2$.

The spatial distribution of $\varepsilon_{THz}(x,y)$ (see figure2.7) is a periodic distribution that can be expressed in a Fourier series as:

$$\epsilon(x) = \sum_{p=-\infty}^{\infty} \epsilon_p e^{-i\frac{2\pi p}{d}x} \tag{2.57}$$

2.4.1 THz waves in TE polarization

We start with the equations that describe the propagation of TE polarization waves presented in equations(2.9, 2.10 2.11). In this case, a linear polarized THz

wave with transverse electric (TE) polarization is obliquely incident on the photo-generated grating based on an undoped-InAs slab. The central coefficient of the TE-polarization is E_z:

$$\partial_x^2 E_z + \partial_y^2 E_z + k^2 \varepsilon E_z = 0 \tag{2.58}$$

Since the problem is periodic along the x-direction, we use the Bloch's theorem which presents a simple form to describe the field:

$$E_z = \sum_{q=-\infty}^{\infty} E_q(y) e^{i\alpha_q x} e^{i\omega t} \tag{2.59}$$

where q is a vector which contains n number of harmonics retained in the field, $\alpha_q = \alpha_0 + q\frac{\lambda}{d}$ with $\alpha_0 = \sin(\theta_{THz})$ control the pseudo-periodicity of the fields by using the THz wave angle of incidence (θ_{THz}). Thus, by neglecting the dependence in $e^{i\omega t}$, we can write:

$$E_z = e^{i\alpha_0 x} \sum_{q=-\infty}^{\infty} E_q(y) e^{i\frac{2\pi q}{d}x} \tag{2.60}$$

By projecting Eq.2.60 on Eq.2.58, we get an equation in y for each Fourier component of the field decomposition thus obtaining:

$$\partial_y^2 E_{zm}(y) = \alpha_m^2 E_{zm}(y) - k^2 \sum_{p=-\infty}^{\infty} \varepsilon_{m-p} E_{zp}(y) \tag{2.61}$$

The above equation can be simplified in a matrix notation for the E_z field.

$$\partial_y^2 E_z = T E_z \tag{2.62}$$

where T is the Toeplitz matrix composed of ε_{m-p} elements corresponding to the Fourier coefficients, as follows:

$$T = [\epsilon] - [\alpha_d][I][\alpha_d] \tag{2.63}$$

where I is the unity matrix with m elements, α_d is a diagonal matrix with diagonal elements α_m where $m = 2n+1$, and $[\epsilon]$ is the matrix with their m, p element equal to ε_{m-p}, defined in Eq.2.57. The matrix notation is used to calculate the electromagnetic properties implementing the matrices S. To calculate the electromagnetic properties of the metasurfaces enlightened by a THz wave, we use the scattering matrix method presented in Appendix A.

2.4.2 THz waves in TM polarization

In this scenario, a linear polarized THz wave with transverse magnetic (TM) polarization is obliquely incident on the photo-generated grating based on an undoped-InAs slab. The equations that describe the TM propagation waves are:

$$\partial_y H_z = i\omega\varepsilon_0 \bar{\varepsilon} E_x \tag{2.64}$$

$$\partial_x H_z = -i\omega\varepsilon_0 \bar{\varepsilon} E_y \tag{2.65}$$

$$\partial_x E_y - \partial_y E_x = -i\omega\mu_0\bar{\mu}H_z \tag{2.66}$$

The central coefficient for the TM-polarization is H_z:

$$\partial_x(\frac{1}{\varepsilon}\partial_x H_z) + \partial_y(\frac{1}{\varepsilon}\partial_y H_z) + k^2 H_z = 0 \tag{2.67}$$

In TM polarization, the resolution consists in calculating the Toeplitz matrix, as presented in the TE-polarization case. The difference resides in the use of the Fourier series of the function $1/\epsilon(x)$ [98] as follows:

$$\frac{1}{\epsilon(x)} = \bar{\epsilon}(x) = \sum_{p=-\infty}^{\infty} \bar{\epsilon}_p e^{-i\frac{2\pi p}{d}x} \tag{2.68}$$

In this scenario, the Toeplitz matrix for the TM-polarization is given by:

$$T = [\bar{\epsilon}]^{-1}([I] - [\alpha_d][\epsilon]^{-1}[\alpha_d]) \tag{2.69}$$

where the Toeplitz matrix belongs to the following equation:

$$\partial_y^2 H_z = T H_z \tag{2.70}$$

thus, we can resolve this equation by following the same reasoning as the one used for TE polarization. Nevertheless, the interface relation from one medium to another medium is different. It can be explained by the fact that if we note that $U = E_z$ or $U = H_z$ and in each medium (i) we consider that:

$$\Delta U_i + k_0^2 n_i^2 U_i = 0 \tag{2.71}$$

The interface relation imposes that: U_i and $(1/P_i)(\partial U_i/\partial y)$ are continuous with:

$$P_i = \begin{cases} \varepsilon_i & \text{in H}_\text{z} \\ 1 & \text{in E}_\text{z} \end{cases} \tag{2.72}$$

This difference modifies the scattering matrix or S-matrix presented in the appendix A.

With our multi-physics code based on the finite element method (FEM) coupled to rigorous coupled wave analysis (RCWA) that simultaneously solves the ambipolar transport equation and the electromagnetic problems at the IR and THz frequencies [98, 93], we analyze the electromagnetic properties of the InAs slab as a function of the pitch d, the thickness h, the pump fluence Φ_0 and the polarization of the THz wave. In order to correctly simulate the complex spatial distribution of $\varepsilon_{THz}(x, y)$, the InAs slab is divided into a subset of layers (of thickness $L_a/5$). Before conclusing, we restrict this study to the normal incidence for the THz plane wave.

2.5 Results and discussion

The electromagnetic properties of the photo-generated metasurfaces are studied for 3 thicknesses of $0.1L_a$, $1L_a$, and $3L_a$ in order to reveal the impact of the carrier diffusion within the InAs slab. The efficiency of the structures is evaluated by calculating the absorption coefficient for the THz radiations. When the pump is turned on, electromagnetic losses are introduced for the THz waves. However, when

the pump is turned off, the THz absorption is null since InAs is a dielectric. In the following theoretical results, a high-speed modulation rate of 10MHz (for the THz absorption) is expected due to the InAs recombination time $\tau_r = 1\text{x}10^{-7}(s)$.

2.5.1 Thin films

We start with photo-generated gratings into a thin InAs slab of thickness $h = 1.5\,\mu m$ $(0.1L_a)$ which is very small compared to the ambipolar diffusion length and to the wavelength of the THz plane wave that lies in the range of $120\,\mu m$ to $400\,\mu m$. We first consider a low pump fluence $\Phi_0 = 10\,W.cm^{-2}$. Figure2.8 represents the photo-generated carrier density for a pitch $d = 153.2\,\mu m$ $(10La)$ and the optically induced real part of the relative permittivity calculated at $\lambda = 230\,\mu m$ $(15L_a)$. The maximum carrier density of $3.1 \times 10^{16}\,cm^{-3}$ is reached where the electric field of the pump is maximum. We observe that the relative permittivity $\epsilon_{THz}(x, y)$ only varies along the x-direction as the pump modulation.

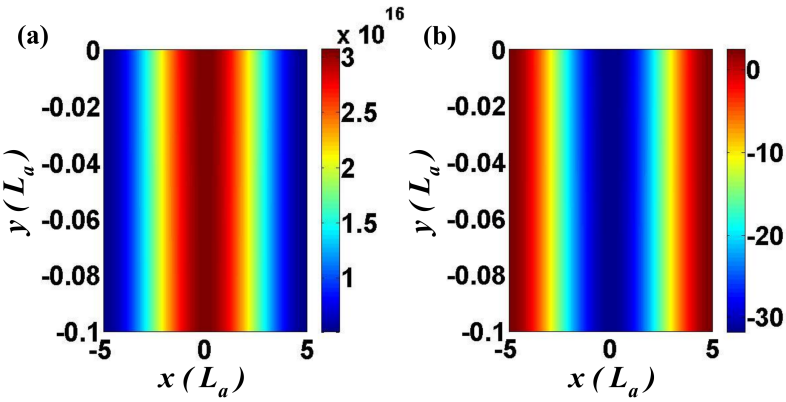

Figure 2.8 – *Maps of the carrier density (a) and of the real part of the relative permittivity (b) for a pitch $d = 10L_a$, a thickness $h = 0.1L_a$ at $\lambda = 15L_a$ and for a pump irradiance of $10\,W.cm^{-2}$.*

In contrast, $\epsilon_{THz}(x, y)$ is almost constant in the y-direction since for a slab thickness smaller than the ambipolar diffusion length L_a the gradient of the carrier density in the y-direction is weak. The lateral pump modulation induces nevertheless a modulation of $\epsilon_{THz}(x, y)$ in the x-direction that critically depends on the scale of the pitch d compared to L_a. To understand the electromagnetic response at THz frequency, we calculate the real parts of the average permittivity $\bar{\epsilon}$ (first term of the Fourier series) and the permittivity variation $\Delta\bar{\epsilon}$ (second term of the Fourier series (x2)) defined by:

$$\bar{\epsilon} = \frac{1}{h}\int_0^h \epsilon_0(y)dy, \tag{2.73}$$

$$\Delta\bar{\epsilon} = \frac{1}{h}\int_0^h \Delta\epsilon(y)dy \tag{2.74}$$

These parameters are plotted as a function of the normalized wavelength λ/L_a and the pitch d/L_a, Fig.2.9. The average permittivity map shows that the InAs slab behaves like a metallic layer for wavelengths larger than $10L_a$ regardless of the pitch

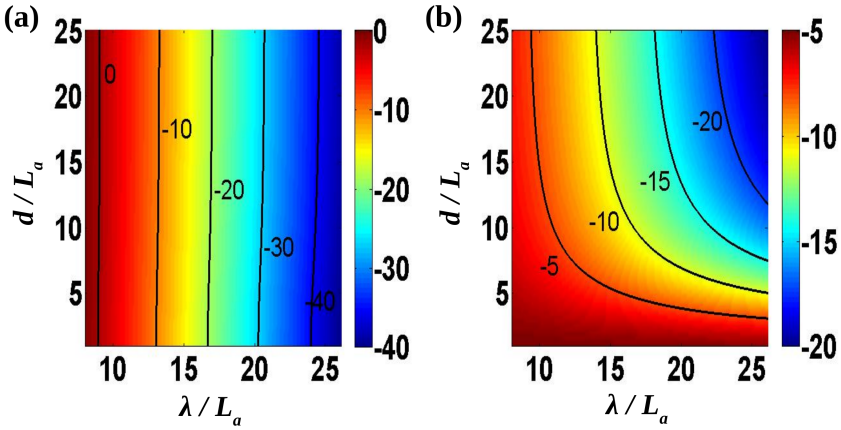

Figure 2.9 – *(a) Average relative permittivity $\bar{\epsilon}$ and (b) permittivity variation $\Delta\bar{\epsilon}$ with respect to the normalized wavelength and the pitch d for a thin slab of $h = 0.1L_a$ and a pump irradiance of $10\,W.cm^{-2}$*

of the grating, Fig.2.9-(a). In parallel, the permittivity variation $\Delta\bar{\epsilon}$ increases at large wavelengths and is sensitive to the pitch d because of the free carriers lateral diffusion, Fig.2.9-(b). When d is small enough, typically $d < 5L_a$, $\Delta\bar{\epsilon}$ decreases and saturates since the carriers diffuse between consecutive pump spots. In that case, the permittivity is almost homogeneous within the InAs slab. These results suggest that two kinds of photo-generated structures can be realized in a thin InAs layer: homogeneous metallic slabs (HS) are obtained for a pitch $d < 5L_a$ while metallic grating structures (GS) are generated when $d > 5L_a$. To verify this assertion, we plot the THz absorption spectra for several pitches, Fig.2.10. The maps of the absorption coefficient calculated with respect to the normalized wavelength and the pitch show that the THz absorption strongly depends on the polarization of the THz waves. For the TE polarization case (the electric field is perpendicular to the x-y plane), an absorption between 30% to 40% is reached for the HS ($d < 5La$) and for a broadband wavelength range spanning from $15L_a$ ($225\,\mu m$) to $26L_a$ ($400\,\mu m$), Fig. 2.10-(a). For the TM polarization case (the magnetic field is perpendicular to the x-y plane), the absorption coefficient attains 45% when a metallic GS is optically induced, Fig.2.10-(b).

These results demonstrate that for a weak pump irradiance, a thin InAs films is equivalent to a metallic slab. An increase of the pump irradiance results in realizing a metallic layer of very high negative real and imaginary parts for the permittivity. In that case, the THz waves are strongly reflected by the InAs slab which decreases its absorption. To circumvent this limitation, we consider a thicker InAs slab in order to decrease the carrier density, and to increase the electromagnetic wave interaction with the InAs slab.

2.5.2 Thick films

In this section, we study InAs slab of thickness $h = 15\,\mu m$ which is equivalent to one diffusion length L_a. A pump fluence of $50\,W.cm^{-2}$ is used to maintain a sufficient carrier density. In this framework, the carrier density calculated for a pitch $d = 10L_a$

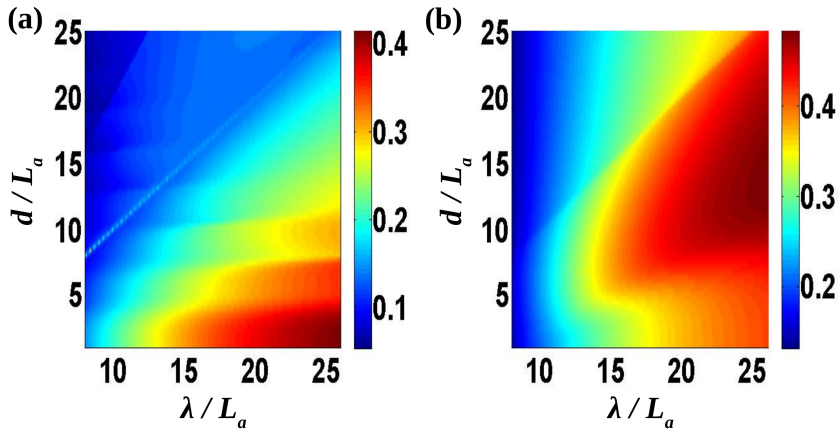

Figure 2.10 – *Absorption spectra calculated for TE (a) and TM (b) polarization cases with respect to the normalized wavelength and pitch. The InAs thickness is* $h = 0.1L_a$ *and the pump fluence is* $10\,W.cm^{-2}$.

and at $\lambda = 15L_a$ presents gradual variations in both x and y-directions and attains a maximal value of $2.2 \times 10^{16} cm^{-3}$, Fig.2.11-(a). This value is comparable to that observed for the thin layer but is now obtained for a pump fluence 5 times larger. When h is increased, the photocarriers are indeed able to diffuse into the InAs layer which in turn decreases their density. The photo-generated permittivity calculated at $\lambda = 15L_a$ varies in both directions and shows that the InAs layer is mostly a metal laterally sandwiched between two dielectric areas, Fig.2.11-(b). The average permittivity and its variation with respect to the wavelength and the grating pitch are plotted to identify the different kind of structures that can be photo-generated, Fig.2.12.

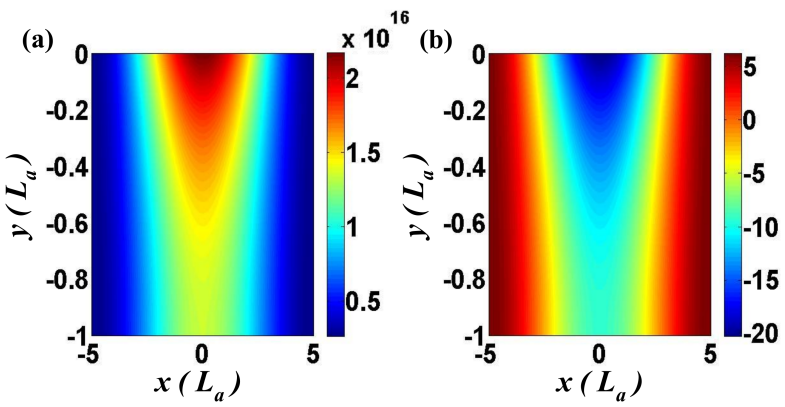

Figure 2.11 – *Maps of the carrier density (a) and of the real part of the relative permittivity (b) for a pitch* $d = 10L_a$*, a thickness* $h = L_a$ *at* $\lambda = 15L_a$ *and for a pump irradiance of* $50\,W.cm^{-2}$.

The average permittivity is shown to vary from positive to negative values when the wavelength increases. This transition arises around $\lambda = 183.84\,\mu m$ $(12L_a)$ where the real part of the average permittivity is near-zero: $\Re(\bar{\epsilon}) = 0$. The permittivity

variation $\Delta\bar{\epsilon}$ shows again that the InAs slab behaves as a HS or a GS when d is either smaller or larger than $5L_a$. However, according to the wavelength, several types of HS can be optically induced ranging from lossy dielectrics, epsilon-near-zero (ENZ) layers to metallic layers. When $d > 5L_a$, dielectric or metallic grating structures are respectively obtained for wavelengths respectively lower or larger than $12L_a$.

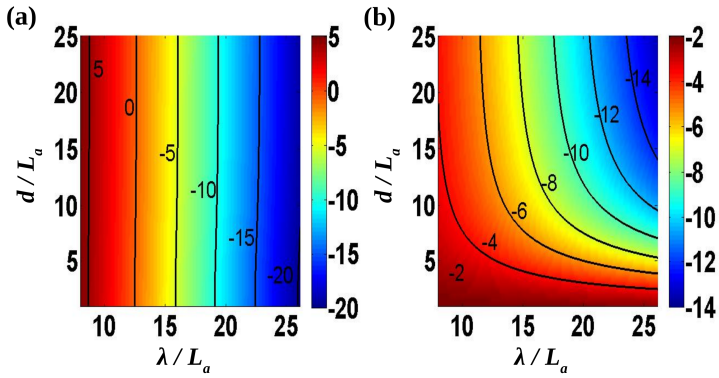

Figure 2.12 – *(a) Average relative permittivity $\bar{\epsilon}$ and (b) permittivity variation $\Delta\bar{\epsilon}$ with respect to the normalized wavelength and the pitch d for thick thickness material $h = L_a$, and a pump irradiance $50\,W.cm^{-2}$*

This variety of structures engenders several absorption mechanisms for the THz waves which depends on their polarization, Fig.2.13. For the TE-polarization case, the grating regime (GS) allows in particular to monitor an absorption line over a wide range of wavelengths ($12L_a$-$25L_a$) by varying the pump period d and for a constant fluence, Fig.2.13-(a). At shorter pitches, for $d < 5L_a$ when HS are photo-generated, a 50% absorption peak is reached around $\lambda = 12L_a$ for both polarizations. In this regime, a Fabry-Perot resonance traps efficiently the THz waves within an ENZ homogeneous slab which boosts the absorption. This effect occurs for a wavelength close to the average plasma wavelength denoted $\bar{\lambda_p}$ and defined by $\Re(\bar{\epsilon}(\bar{\lambda_p})) = 0$.

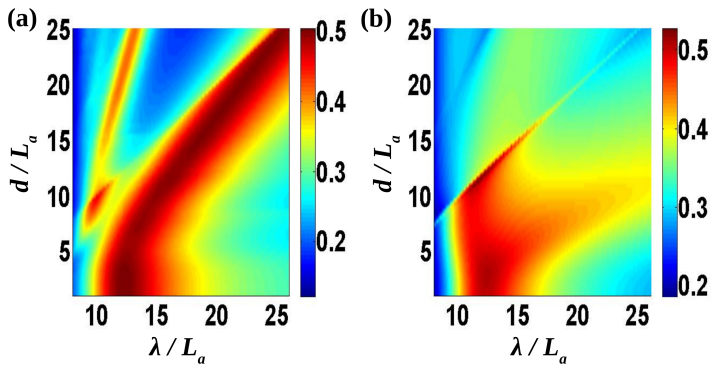

Figure 2.13 – *Absorption spectra calculated for TE (a) and TM (b) polarization cases with respect to the normalized wavelength and the pitch. The InAs thickness is $h = L_a$ and the pump irradiance is $50\,W.cm^{-2}$.*

It can be seen from equation (2.52) that $\bar{\lambda_p}$ is linked to the average carrier density $\bar{N_0}$ which is driven by the pump irradiance. We deduce that $\bar{\lambda_p} = C/\Phi_0$ where C is

a constant that depends on material parameters. This property allows to control the spectral position of the ENZ absorption line by varying the pump irradiance. For example, for $d = 2.5L_a$, the ENZ absorption peak varies from $8L_a$ to $26L_a$ with a constant efficiency of 50% when the pump irradiance varies from $25\,W.cm^{-2}$ to $100\,W.cm^{-2}$, Fig.2.14.

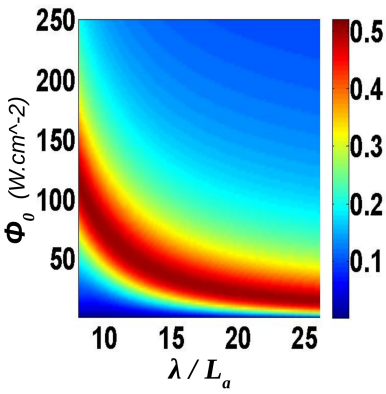

Figure 2.14 – *Absorption spectra calculated with respect to the pump irradiance and the normalized wavelength. The InAs thickness is $h = L_a$ and the pitch $d = 2.5L_a$.*

It is worth noting that this ENZ absorption mechanism is particularly well suited to realize a broadband dynamic THz absorber. From a practical point of view it can be realized with a uniform pump since it does not stem from the spatial modulation of the permittivity. To conclude this section, InAs layers of thicknesses settled about one ambipolar diffusion length offer a wide control over the THz radiations by means of the modulation of the period of the optically induced grating and by the variation of the pump power.

2.5.3 Ultra-thick films

Let us consider an ultra-thick InAs layer whose thickness $h = 45.96\,\mu m$ $(3L_a)$ is larger than the ambipolar diffusion length. For a pump irradiance of $50\,W.cm^{-2}$, a pitch $d = 10L_a$ and $\lambda = 15L_a$, the carrier density presents strong gradual variations in the y-direction and reaches a maximal value about $1.9 \times 10^{16} cm^{-3}$, Fig.2.15-(a). This carrier spatial distribution generates a metallic inclusion into a dielectric host, Fig.2.15-(b). This permittivity map resembles a metallic grating whose footprint is limited to a thickness of L_a within the InAs layer.

The average relative permittivity and permittivity modulation maps confirm that ultra-thick InAs layer exposed to a low pump are dielectric structures presenting a small metallic area, Fig.2.16.

The spectra obtained for both TE and TM polarized THz waves show that high absorption up to 67% is reached for a small range of wavelength restricted between $13L_a$ and $15L_a$, Fig.2.17. We again remark that the same efficiency is obtained for both polarization cases when HS are formed for $d < 5L_a$. This absorption peak appears close to the average plasma wavelength derived for a $h = L_a$ thick layer. This suggest that the THz waves interact with a ENZ layer whose thickness is restricted to a distance of about L_a where the permittivity presents a noticeable modification.

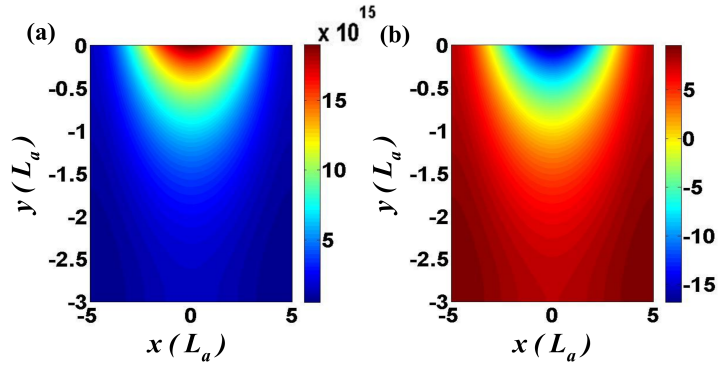

Figure 2.15 – *Maps of the carrier density (a) and of the real part of the relative permittivity (b) for a pitch* $d = 10L_a$*, a thickness* $h = 3L_a$ *at* $\lambda = 15L_a$ *and for a pump irradiance of* $50\,W.cm^{-2}$*.*

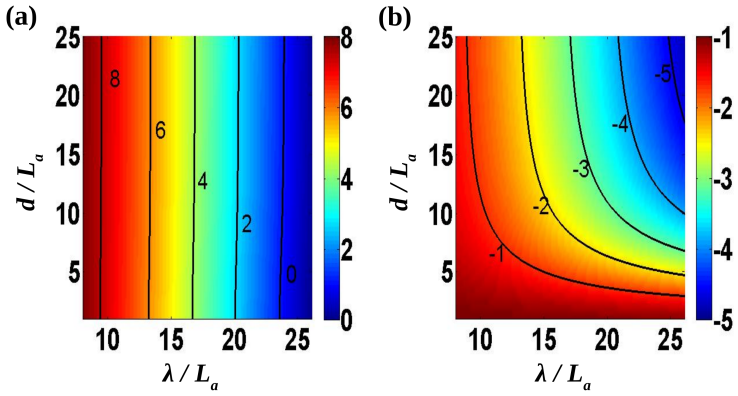

Figure 2.16 – *(a) Average relative permittivity* $\bar{\epsilon}$ *and (b) permittivity variation* $\Delta\bar{\epsilon}$ *with respect to the normalized wavelength and the pitch d for ultra-thick thickness material* $h = 3L_a$*, and a pump irradiance of* $50\,W.cm^{-2}$*.*

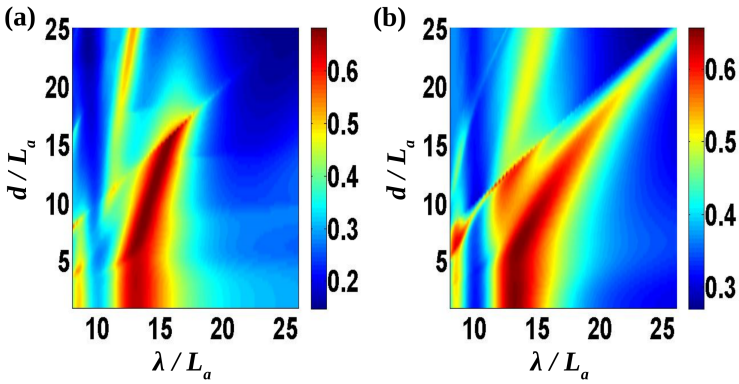

Figure 2.17 – *Absorption spectra calculated for TE (a) and TM (b) polarization cases with respect to the normalized wavelength and the pitch. The InAs thickness is* $h = 3L_a$ *and the pump irradiance is* $50\,W.cm^{-2}$*.*

To evaluate the dynamic control of the ENZ absorption which arises for unpolarized THz waves, we calculate the absorption spectra for $d = 2.5L_a$ and for a varying pump irradiance, Fig.2.18. The fundamental Fabry-Perot resonance appears in a small range of wavelengths between $12L_a$ and $15L_a$ when the pump irradiance increases from $25\,W.cm^{-2}$ to $100\,W.cm^{-2}$.

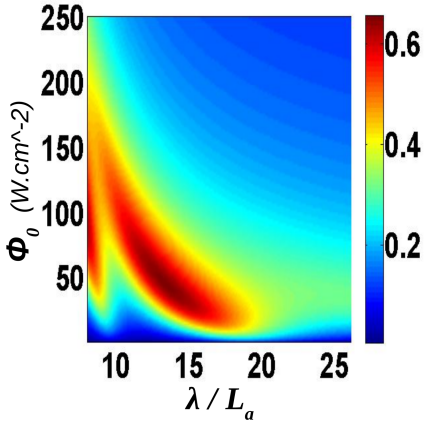

Figure 2.18 – *Absorption spectra calculated with respect to the pump irradiance and the normalized wavelength. The InAs thickness is $h = 3L_a$ and the pitch $d = 2.5L_a$.*

Finally, an increase of the InAs layer thickness beyond L_a enhances the absorption of the THz wave but lowers the spectral dynamic control of the absorption lines.

2.6 Summary

We have investigated photo-generated metasurfaces for realizing fast and efficient dynamic THz absorbers. Indium Arsenide is demonstrated to be a promising material that tackles the actual limitations of this approach. The diffusion of the photocarriers plays a crucial role for realizing grating or homogeneous structures when a spatially modulated pump is considered. The study of the electronic and electromagnetic properties of an InAs layer shows that resonant absorption lines are monitored by the pump irradiance and by the spatial period of the pump. These properties drastically depend on the InAs layer thickness compared to the ambipolar diffusion distance. For a $45\,\mu m$ thick InAs layer, the modulation of the THz absorption coefficient is demonstrated to increase with the thickness and attains 67% for a CW pump irradiance of only $50\,W.cm^{-2}$. In contrast, thin layers of about $1.5\,\mu m$ present an absorption of 40% for a very low irradiance of $10\,W.cm^{-2}$. However, the best dynamical control for monitoring the absorption lines is obtained for a thickness of $15\,\mu m$ which corresponds to an ambipolar distance. In that case, a Fabry-Perot resonance arises close to ENZ regime and boosts the absorption to 50%. This ENZ-absorption can be optically actuated over a broad frequency band ranging from 1 THz to 3 THz when the pump fluence is increased from $25\,W.cm^{-2}$ to $100\,W.cm^{-2}$. These results open promising avenues for realizing on chip active THz components based on InAs since low pump powers of only $500\,mW$ can be easily delivered by integrated CW lasers.

In the following chapters, we devoted our efforts to experimentally demonstrate the main theoretical statements established in this chapter, which are the ambipolar diffusion length and the active control of the THz radiation at low-pump irradiances, both at room-temperature. These demonstrations will be carried out in the NanoMIR group at the Université de Montpellier.

Chapter 3

Technological fabrication

3.1 Photo-conduction devices 47
3.1.1 TLM substrate composition 48
3.1.2 Fabrication - TLM 49
3.1.3 Results and discussion 51
3.2 THz modulation samples: InAs membranes 53
3.2.1 Fabrication process 54
3.2.2 Wet chemical etching : Calibration of the etching rate for InAs using (H_3PO_4: H_2O_2 : H_2O) 56
3.2.3 InAs membranes made by epitaxy growth 56
3.2.4 Results and discussion 57
3.3 Summary 59

This chapter is dedicated to the procedure carried out to fabricate the samples of the two main studies: Photoconduction devices and Photomodulation of the THz waves. The photoconduction device is fabricated in order to extract the diffusion length of the photogenerated carriers. Once the diffusion length value is obtained, it is possible to estimate the thickness of the InAs membrane that will give the most efficient photomodulation of the THz waves. Two different approaches to reveal the real impact of photogenerated metasurfaces based on an undoped-InAs slab are presented.

3.1 Photo-conduction devices

The objective is to measure the ambipolar diffusion length in the undoped InAs material that has been established theoretically. The two main challenges are: first, to study and fabricate a structure allowing to measure the diffusion length without perturbation by the conductive substrate. Secondly, to ensure that the excess carriers can be collected efficiently with ohmic contacts.

The best solution to overcome this approach is to implement Transmission Line Measurement or Transfer Length Measurement (TLM) [99]. TLM gives us the advantage to know the geometry of the distances that we are measuring, which is crucial to estimate the carrier diffusion length. However, the main limitation of the manufacturing process is the ohmic contact. The tiny ohmic contacts are bonded with a gold thread whose diameter is the same than the ohmic contacts groove, which leads to the fact that the gold thread detaches easily to the welding.

The TLM is fabricated in a structure [100, 101] where the barrier has been intentionally Te-doped to avoid carriers (electrons-holes pairs) leakage in the substrate. More details about this follows in study of the substrate composition (below).

3.1.1 TLM substrate composition

In this work, the role of the substrate composition structure is to prevent the photo-generated electron-hole pairs switching from the contact layer to the substrate. First, to confine the space charge zone in the barrier it is necessary to have the same doping type. The barrier structure is directly dependent on the thickness and its doping level. In this case, the material which composes the barrier structure have to be intentionally Te-doped in order to cut the passage of the holes towards the contact layer. In this form we are able to collect the photo-generated carriers; (electrons and holes), created in the contact layer by an IR irradiance.

In the search of the structure geometry composition Nextnano simulation tool has been used. Nextnano is a software which models the bands diagram. The structure simulated in Nextnano is composed of: an $InAs$ substrates, a layer of $AlAsSb$ which has been intentionally Te-doped followed by a layer $InAs$ material. The arsenic (As) content allows lattice to match to the InAs substrate because the small quantity of arsenic ($As_{0.16}$) allows the $AlSb$ alloy to have the same lattice parameters that InAs, as it can be inferred in Fig.3.1. Then, the barrier content is $AlAs_{0.16}Sb_{0.84}$.

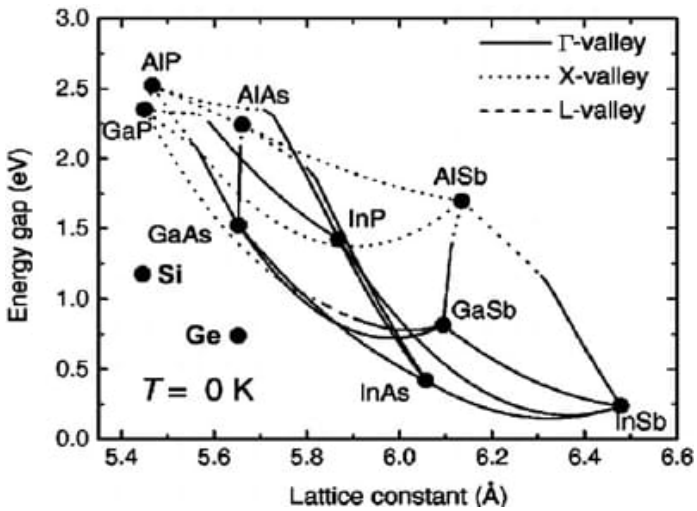

Figure 3.1 – *Band gap and lattice constant for various III-V and group-IV material alloys [102].*

The alignment of the bands due to the concentration of the materials, locates the barrier in the conduction band. In this case, the barrier composition is $AlAs_{0.16}Sb_{0.84}$ and its bands diagram is presented in Fig.3.2. In the figure, the barrier prevents the photo-generated electrons from passing towards the substrate zone and the passage of the holes towards the contact layer. In that case, the offset of the conduction band at the contact-barrier interface must be as large as possible in order to limit the photonic current (see the red line in Fig.3.2) and, on the other hand the offset

of the valence band must be the highest possible in order to cut the passage of the thermionic current (see the blue line in figure3.2).

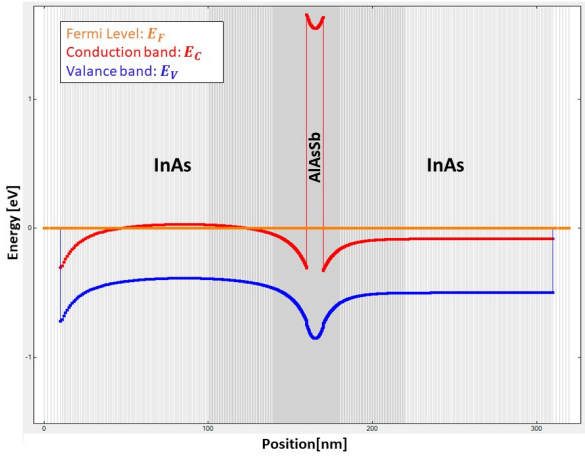

Figure 3.2 – *Schematic of the bands diagram of the nBn structure composed of InAs, AlAsSb, and InAs modeled with the software Nextnano.*

After having validated the structure by Nextnano software, the structure is grown by using solid source molecular beam epitaxy (MBE) in growth chamber Riber 412. An undoped-InAs substrates of crystalline orientation (1 0 0) is used. First, a layer of $AlAs_{0.16}Sb_{0.84}$ of ($200nm$) thickness and followed by a non-intentionally doped $InAs$ layer of around ($1.5um$) thick is used. The MBE growth was performed by the researchers Alexei BARANOV and Laurent CERUTTI from the group NANOMIR at IES.

3.1.2 Fabrication - TLM

The TLM samples are subjected to different steps of realization mainly by optical lithography and chemical etching process [103, 104]. To enlighten this fabrication steps, a process flow has been carried out where it details the steps to follow. The process flow for sample fabrication consists in the following steps.

1. Substrate preparation: After having grown the sample $InAs(1.5um)$, $AlAsSb(200nm)$, and $InAs(500um)$ by using MBE, the surface quality is inspected by optical microscopy and the sample is successively rinsed with acetone, ethanol and isopropanol bath and dried under a nitrogen flow (Fig. 3.7.A).
2. Photoresist deposition (1): the sample is covered with AZ-5214 photo-resist, spread and spun at 4000rpm for 30s with 4s acceleration ramp. Then, the solvent is expelled by a postbake at 110°C for 2min (Fig. 3.7.B).
3. Photolithography (1): Nanomir group has a mask E256-L3 with different TLM patterns, circular and rectangular (presented in figure3.3-A). The expected pattern is aligned in the center of the sample. To bring the sample and the mask in closest contact, a hard contact is applied [105]. The sample is exposed during $6.5s$ to UV exposure (Fig. 3.7.C).
4. Resist development (1): the AZ-5214 photoresist is developed during 50s using AZ-726 developer (Fig.3.7.D).

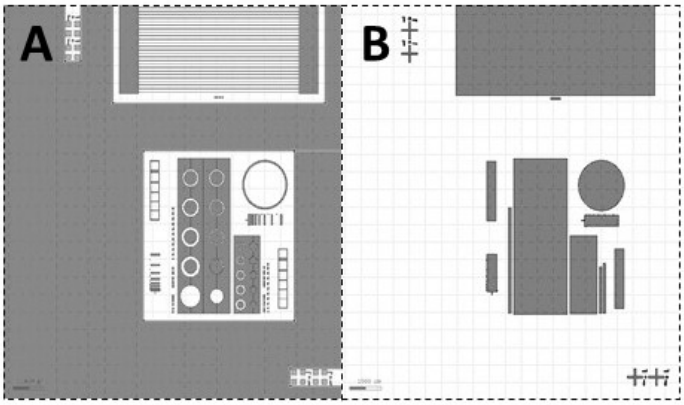

Figure 3.3 – *(A) Set-up of the ohmic contact mask name: E256-L3. (B) Set-up of the mesa mask name E256-L1. The set-up shows the alignment marks on the mask for the mesa fabrication.*

5. Metal deposition: a previous desoxidation of the sample is carried out before the metal deposition. The sample is put into a solution of hydrochloric acid (HCl) diluted in H_2O with a concentration of $1:5$. Then, a metal deposition is made by Joule evaporation in a vacuum chamber. A layer of titanium (Ti) of $50nm$ thick is deposited which act as an adhesive layer on the semiconductor and then a layer of gold (Au) of $350nm$ thick is also deposited (Fig.3.7.E).

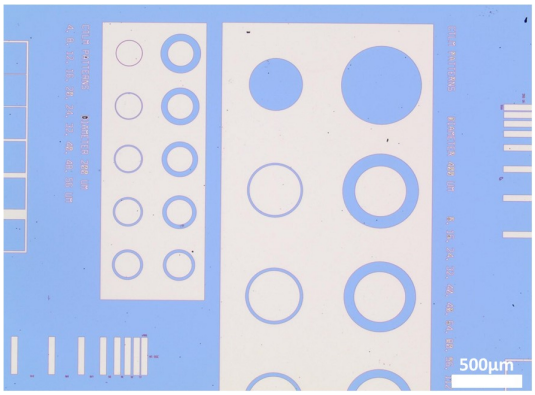

Figure 3.4 – *Optical microscope image of EQ443.4 TLM sample after Lift-Off manufacturing process step.*

6. Lift-Off: the AZ-5214 photoresist must be removed by a step of lift-off and the metal deposited on it, we use for it a bath of acetone. Then, a metallization reinforcement is performed on a hotplate at 110℃ during 5min. It is an important step to solidify the ohmic contacts allowing a better adhesion to the semiconductor for a future welding step (Fig.3.7.F).

7. Photoresist deposition (2): a layer of AZ-1518 photoresist is applied at 4000rpm for 30s with 2s acceleration ramp. Then, the solvent is evaporated by a postbake at 110℃ for 1min (Fig.3.7.G).

8. Photolithography (2): Nanomir group has a mask E256-L1 with the corresponding mesa for the different TLM patterns, circular and rectangular (presented in figure3.3-B). The expected pattern is aligned with alignment marks of the mask and the sample [105]. The sample is exposed during 6.5s using soft contact mode (Fig.3.7.H).
9. Development (2): the AZ-1518 photoresist is developed during 30s using AZ-726 developer (Fig.3.7.I).

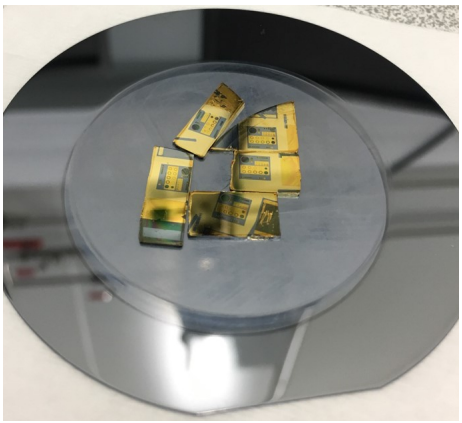

Figure 3.5 – *Caption of the EQ*443.1,2,3,4 *and* 5 *TLM samples at the end of plasma etching.*

10. Dry chemical etching: an Oxford instruments ICP-RIE reactor is used to etch the InAs layer. The standard recipe "Sputt-Ar-50W" of the NanoMir group is followed for the etching of InAs. The process gas is Argon (Ar). The laser interference signal is applied to control the etching process and it stops oscillating on the AlAsSb layer. Fig.3.5 presents the samples at the end of this process step (Fig.3.7.J).
11. Final Cleaning: The TLM sample is successively rinsed with acetone, ethanol and isopropanol (to remove the oil for the thermal contact from the bottom side) and dried under a nitrogen flow (Fig.3.7.K).

The photo-conduction devices (TLM) are stuck to the chip carrier ($To-8$) by using Silver A_g lacquer which is a cold welding usual technique for joining metal pieces. Then are welded with golden threads as presented in figure3.8. The golden threads of $50\mu m$ diameter are welded on the areas of contact transfer in the photo-conduction devices (TLM metal grooves composed of titanium and gold $50\mu m$ and $350\mu m$ thick) and reported on the To-8 pins themselves connected to contacts.

3.1.3 Results and discussion

The fabrication process is done at the Central Technologique de Montpellier (CTM). We present some examples of the samples fabricated. Laboratory microscope and Scanning Electron Microscope (SEM) images are acquired by using a FEI SEM INSPECT S50 with high resolution. Here, the presentation of the results is related to the structural fabrication process, the optical characterization of the photo-conduction devices follows in chapter 4.

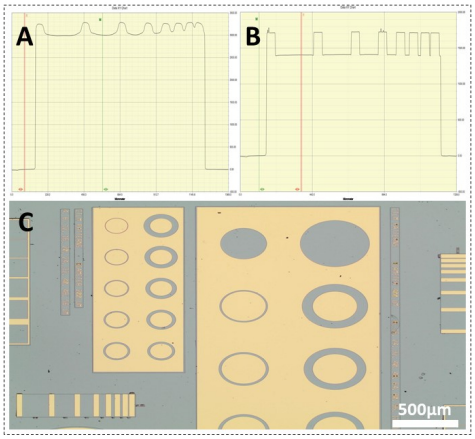

Figure 3.6 – *EQ443.4 TLM sample: A)Dektak measurement at the end of Ar plasma etching. The vertical distance from AlAsSb material to the photo-resist between the TLM grooves is 3µm. B)Dektak measurement at the end of Final Cleaning. The vertical distance from AlAsSb material to the InAs material is 1.5µm. C) Optical microscope image of the sample after the Final Cleaning. The Mesa isolates devices between them. So the conduction is done between the contact close to each TLM structure. The electron and holes barrier assures that no conduction through the substrate is possible between TLM structures.*

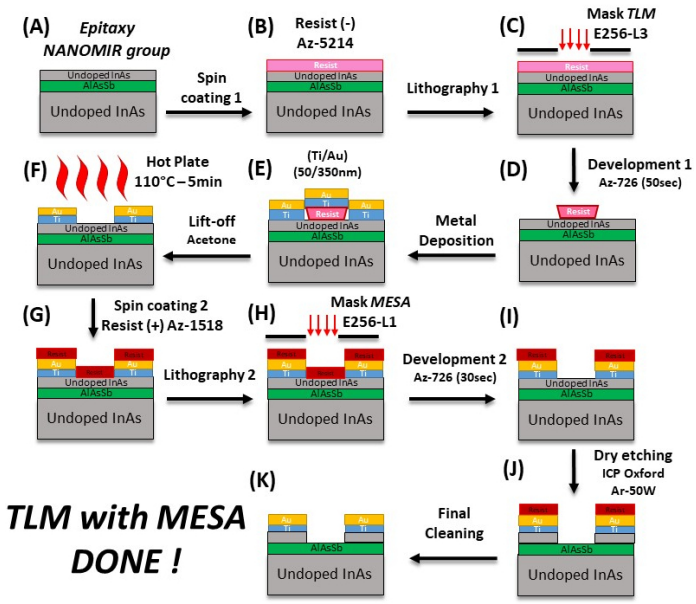

Figure 3.7 – *Process flow for the TLM sample fabrication with mesa. A. Substrate preparation. B. Photoresist deposition (1). C. Photolithography (1). D. Resist development (1). E. Metal deposition. F. Lift-Off and Metallization reinforcement. G. Photoresist deposition (2). H. Photolithography (2). I. Development (2). J. Dry chemical etching. K. Final Cleaning.*

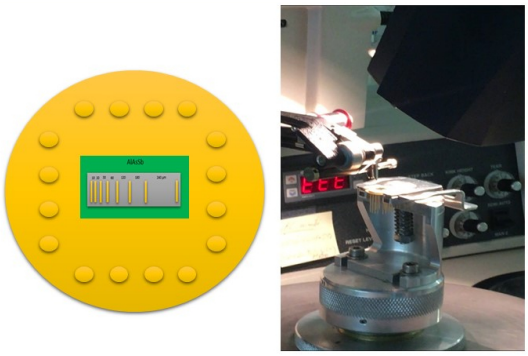

Figure 3.8 – *Schematic of the photo-conduction device on the To-8 chip carrier (Left-image). Picture of welding station (right-image), gold threads welded on metal groove reported on the To-8 pins.*

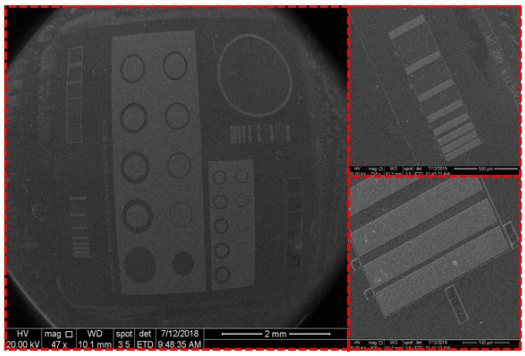

Figure 3.9 – *SEM images of EQ443.4 photo-conduction device fabricated at CTM.*

Figure3.9 illustrates the TLM sample inspected by SEM images. The top views shows in detail the geometry of the TLM built, which is composed of eight gold grooves of width $50\mu m$, located at distances $10\mu m$, $20\mu m$, $30\mu m$, $60\mu m$, $120\mu m$, $180\mu m$ and, $240\mu m$. At last, an inspection has been made in Dektak indicating that the thickness of the undoped InAs material is $1.5\mu m$, the gold contact thickness is $400nm$ (Ti/Au($50nm/350nm$))and that each TLM is isolated with a respective mesa.

Figure3.10 shows the photoconduction device stuck to the $To-8$ and welded. The golden threads of $50\mu m$ diameter are welded on the areas of contact transfer in the photoconduction devices and reported on the $To-8$ pins.

In the following section, we deals with the fabrication process of the intrinsic InAs membranes. Thanks to the Physical Review B [75] results we know that the InAs membranes have to be thin enough (a few micro-meters) to perform a versatile control of the THz waves radiation.

3.2 THz modulation samples: InAs membranes

To demonstrate experimentally the efficient modulation of the THz waves, we fabricate membranes based on undoped InAs. The objective is to produce the optimal thickness of InAs membranes that has been established theoretically.

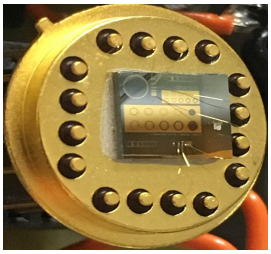

Figure 3.10 – *Picture of photo-conduction device stuck to the To-8 chip-carrier ready to be characterized. It is welded with gold threads on the TLM metal groove reported on the To-8 pins.*

The main challenge of fabrication is the small thickness (10 to 1um) of these membranes. The best solution to overcome this issue of manufacturing is linked with wet chemical etching. The wet chemical etching enables to smooth the surface, which is crucial for the optical characterization, however, the main limitation of the manufacturing process is its brittleness due to the fact that at the end of the procedure, the brittle sample is successively rinsed with acetone, ethanol and isopropanol and dried under a nitrogen flow.

We worked on two different kind of samples: InAs wafer and InAs epitaxial layer.

3.2.1 Fabrication process

The InAs wafer is acquired commercially. The InAs membranes are subjected to different steps of realization. The process flow for sample fabrication consists of the following steps.

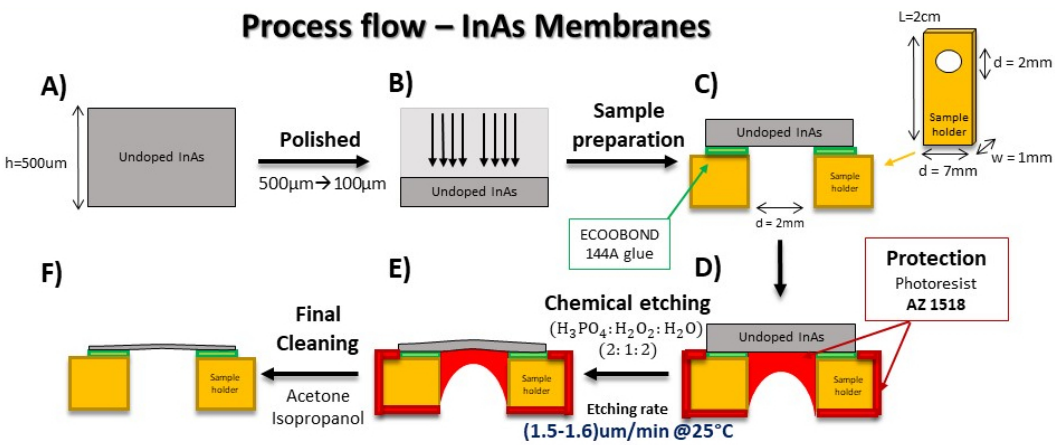

Figure 3.11 – *Process flow for the sample fabrication by polishing and chemical etching. A. Sample preparation. B. Polished. C. Substrate Preparation. D. Protection. E. Chemical Etching of InAs in phosphoric acid. F. Photoresist removal and final cleaning.*

1. Sample preparation: clean with acetone and isopropanol and afterwards cut the sample in four pieces. The pieces of undoped InAs have a thickness of

500μm (Fig.3.11.A).

2. Polished: the InAs thickness of 500μm corresponding to the substrate must be reduced to obtain membranes between 10 to 1μm. It has been reduced by using adhesive abrasive discs type M ϕ200 MM P2400 in a mechanical polishing to achieve a thickness lower than 100μm. The thickness has been measured by using a precision thickness measurement gauge tool. Then, an optical polish is carried out by using Mecaprex self-adhesive polishing disc with powders of aluminum grains of different sizes (20um, 12um, 5um, 1um) (see figure3.12) to ensure an InAs surface without roughness (Fig.3.11.B).

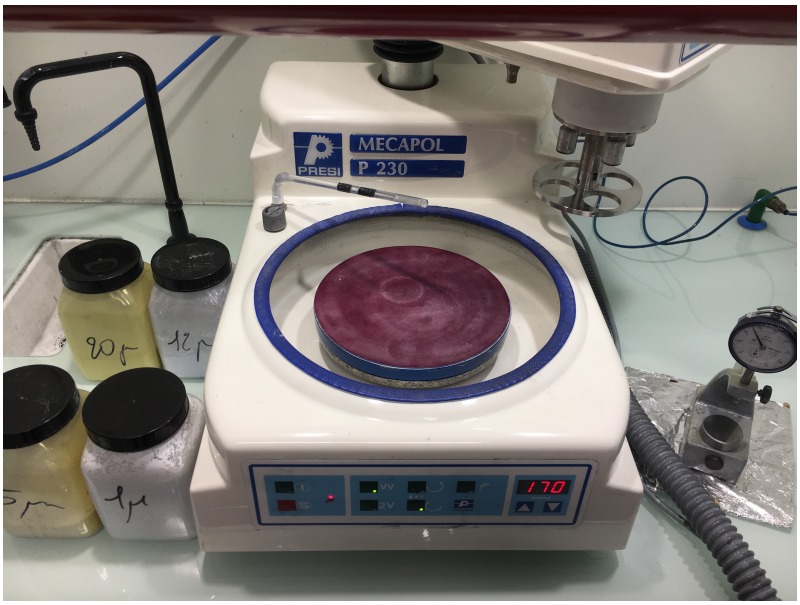

Figure 3.12 – *Picture of the mechanical polishing station. We observe on the left, the powders of aluminum grains of different sizes, on the center a Mecaprex self-adhesive polishing disc with powders of aluminum grains and on the right, the precision thickness measurement gauge tool, instruments that have been used to polish the sample.*

3. Substrate preparation: after having polished the sample, the quality of the surface is inspected by optical microscopy. Then, the sample is cut with a scalpel to obtain a membrane geometry larger than an area of 2mm diameter, corresponding to a hole located 3.5mm from one of the sides of the sample holder. Afterwards, the sample is stuck to the sample holder using the epoxy adhesive ECCOBOND 144A. The sample holder is always a piece of copper covered with a thin layer of gold of dimensions ($Length = 7mm$ (L) x $Width = 1mm$ (B) x $Height = 2cm$ (H)) (Fig.3.11.C).
4. Protection: AZ-1518 photoresist is applied to protect the inside of the hole support holder. To reduce corrosion of the sample holder, it is necessary to cover it with the same product. Then, the photoresist is hardened by a postbake of 110°C during 1 min (Fig.3.11.D).
5. Wet chemical etching: a solution of phosphoric acid diluted in hydrogen peroxide and water (H_3PO_4: H_2O_2 : H_2O (2 : 1 : 2)), is implemented to reduce the InAs

Solution	Material	Speed
(H_3PO_4:H_2O_2:H_2O (2:1:2))	InAs	1.5-1.6 $\mu m/min$ @25

Table 3.1 – *Etching rate parameter for InAs using a solution of phosphoric acid diluted in hydrogen peroxide and water.*

thickness (Fig.3.11.E). Then, the sample is put in the solution and the etching rate is indicated in Table3.1.

6. Final Cleaning: The brittle sample is successively rinsed with acetone, ethanol and isopropanol bath and dried under a nitrogen flow. This is a delicate process since the surface tension of the solvents or the water and especially the drying under a nitrogen flow often can crack the sample (Fig.3.11.F).

3.2.2 Wet chemical etching : Calibration of the etching rate for InAs using (H_3PO_4: H_2O_2 : H_2O)

Etching of InAs is possible using a solution of phosphoric acid diluted in hydrogen peroxide and water (H_3PO_4: H_2O_2 : H_2O). The process is limited by the chemical reaction rate, which means that the material removal rate depends on the rate of the chemical reaction at the surface. The reaction rate is characterized by a proportionality relation between the etch depth and the etch time. In this case, the objective of chemical etching is to reduce the thickness of around 100um to a thickness of (10 to 1um). Clean-room records indicate an etching rate of 1.5-1.6 $\mu m/min$ 25°C for InAs substrate using a solution of H_3PO_4:H_2O_2:H_2O indicated previously in Table 1.1. As a consequence of this etching rate, the sample remains for a long time in the solution. To reduce the thickness of the material in a shorter time, the temperature of the solution is increased from 25°C to 60°C in order to accelerate the etching rate [104, 106, 107]. The InAs etching rate at 60°C is presented in Appendix C.

3.2.3 InAs membranes made by epitaxy growth

Separately from the membranes manufactured with InAs wafer, we also worked on InAs epitaxial layer. The epitaxial membranes samples with a thickness of around 17μm are presented in figure3.13.

The InAs epitaxial membranes are also subjected to a thickness reduction in order to obtain the optimal thickness that has been established theoretically (between 10 to 1um). To reduce the thickness of the InAs epitaxial material, a chemical etching 25°C is used (See Table3.1). Following the membranes fabrication process (see section 3.1.1) the samples were put in a solution where the etching rate is 1.5$\mu m/min$ during 9min and 10min30s obtaining membranes with a thickness of 6.2μm and 5.7μm. Finally, the brittle samples are successively rinsed with acetone, ethanol and isopropanol and dried under a nitrogen flow.

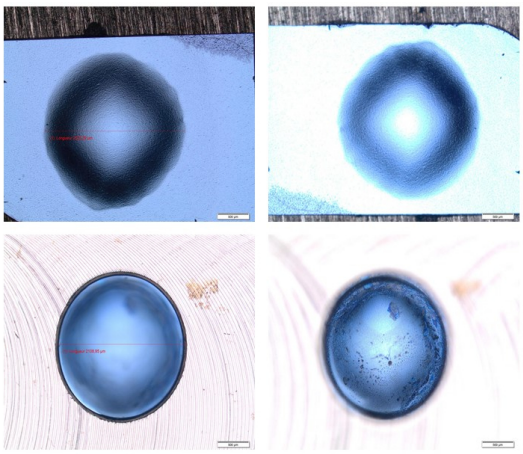

Figure 3.13 – *InAs epitaxial membranes. Both samples with a thickness of around* 17*um.*

3.2.4 Results and discussion

In the following section, some examples of samples fabricated mainly by wet chemical etching process are presented. Laboratory microscope and SEM images were acquired with high resolution at the CTM. Here, the presentation of the results is related to the structural fabrication process.

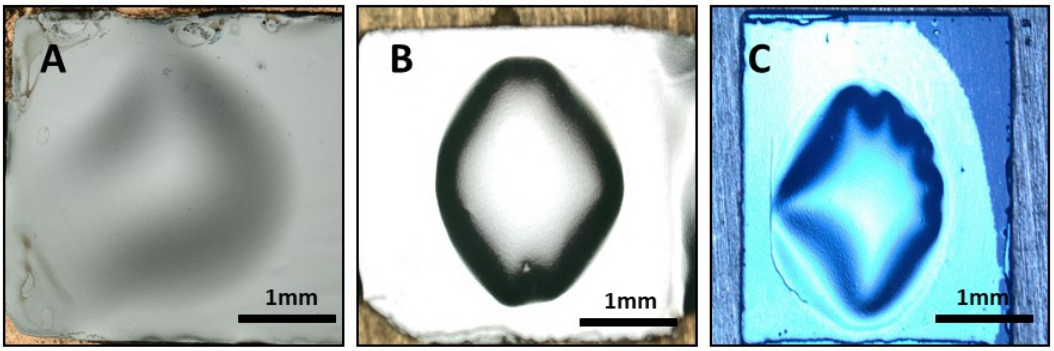

Figure 3.14 – *Laboratory microscope images of undoped InAs membranes fabricated by: A) Material acquired by polishing a substrate and wet chemical etching obtaining a thickness of around* 8.8*um. B) Material acquired by epitaxy growth and wet chemical etching obtaining a thickness of around* 6.2*um and C)* 5.7*um.*

Figure 3.14.A illustrates an undoped InAs membrane acquired by polishing an InAs wafer and wet chemical etching obtaining a thickness of around 8.8μm. The high-resolution image indicates that the wet chemical etching does not smooth completely the surface due to the mechanical polishing. On the contrary, in the figure3.14.B and in the figure3.14.C, the materials are acquired by an InAs epitaxial layer and wet chemical etching obtaining a thickness of around 6.2μm and 5.7μm.

The InAs epitaxial sample of 5.7μm thick is inspected by SEM displayed in Figure3.15. The side views illustrates in figure3.15.A and figure3.15.B show that the InAs epitaxial membrane has been deformed in a concave shape. This concave shape

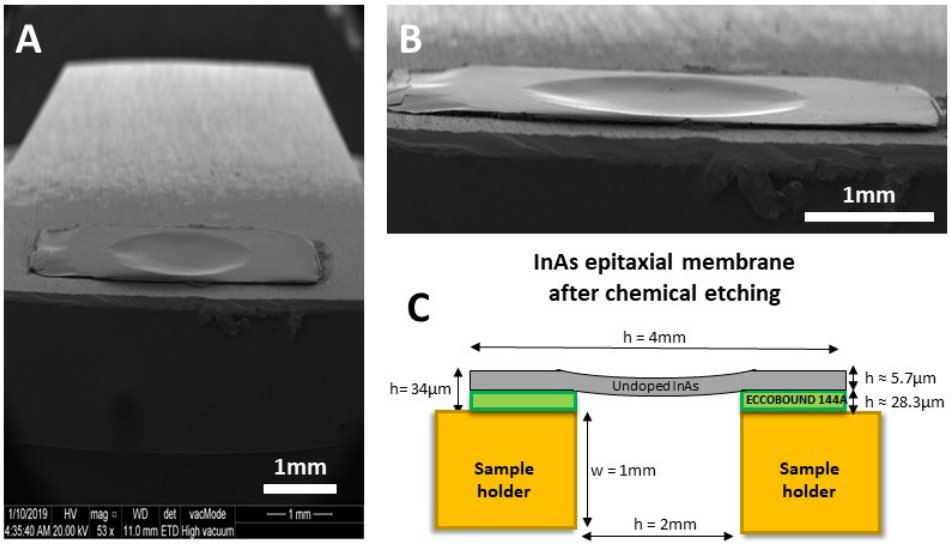

Figure 3.15 – *SEM images of an intrinsic InAs epitaxial membrane fabricated at CTM ready to be photo-generated.*

deformation in the InAs material is probably due to mechanical forces produced by the wet chemical etching on the material. After the wet chemical etching, the material remains in compressive strength due to the liquid surface tension into the hole when we dry the InAs epitaxial sample. An inspection was made in Dektak indicating that the thickness is 34μm and not 5.7μm as expected (see figure3.15.C). The difference in thickness is due to the presence of the adhesive epoxy ECCOBOND 144A with a thickness of around 28.3μm illustrated in figure3.15.C.

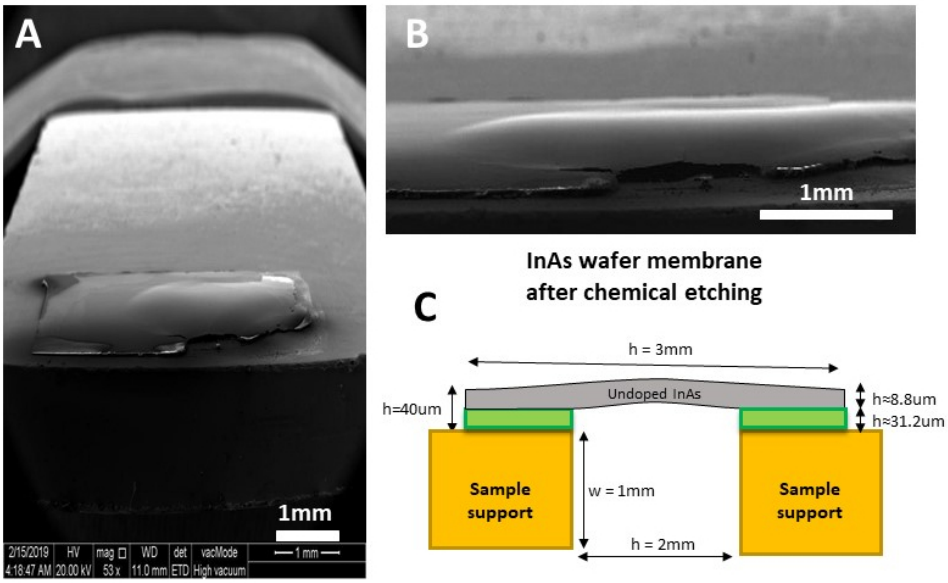

Figure 3.16 – *SEM images of an intrinsic InAs wafer membrane fabricated at CTM ready to be photo-generated.*

The InAs wafer sample of $8.8\mu m$ thick is inspected by SEM displayed in Figure3.16. The side views illustrates the InAs wafer membrane has been deformed in a convex shape. This convex shape deformation in the InAs slab is probably due to the wet chemical etching. The material remains in decompressive strength due to the liquid surface tension into the hole when we dry the InAs wafer sample.

3.3 Summary

In this chapter, two complementary recipes for the fabrication of Photoconduction devices and THz modulation samples were presented.

First, a photo-conduction device fabrication based on optical photolithography and dry chemical etching, applicable for the manufacturing process of TLM devices was presented. The substrate structures was simulated by using Nextnano software, which demonstrates that the selected structure is a configuration able to collect the photogenerated carriers in the layer of undoped InAs of $1.5\mu m$ thick obtained by epitaxy growth. Then, the fabrication process to adapt the standard photolithography process and dry chemical etching in the substrate has been presented. Once all these fabrication steps have been completed to weld the TLM on the To-8 without being detached from the contact part of the semiconductor, we use a metallization reinforcement, which is an important step to solidify the ohmic contact allowing a better adhesion to the semiconductor. This first part of this chapter finished with some SEM images of the TLM. The images show in detail the geometry of the device and the isolation of each TLM. To conclude, it is shown a picture of one of the photo-conduction fabricated device stuck to the To-8 and is ready for optical characterization.

Secondly, THz modulation samples process based on mechanical polishing and wet chemical etching is presented, applicable for the manufacturing process of undoped InAs membranes of 10 to $1\mu m$ thick. The major achievements were to adapt the standard industrial polishing to reduce the thickness of conventional undoped InAs acquired commercially. Two complementary etching rate for the undoped InAs have been studied at 60℃ by considering the influence of the size of the sample holder hole of $2mm$ by using the solution (H_3PO_4:H_2O_2:H_2O (2:1:2)). All these data have been integrated to the IES clean-room database. This second part of this chapter finished with some laboratory microscope images of the undoped InAs membranes. The images shows in detail the geometry of the fabricated InAs membranes and that each InAs membrane has been deformed in a concave shape due to mechanical forces produced by the wet chemical etching on the material. It is also enclosed some SEM images of one undoped InAs membrane stuck to the sample holder and ready to be photo-generated.

Chapter 4

Optical Characterization

4.1 Physical properties of InAs material 61
4.1.1 Photo-luminescence at low-temperature 62
4.1.2 Photo-luminescence at different temperatures 64
4.1.3 Photo-luminescence at room-temperature 67
4.1.4 Numerical simulation of PL at room-temperature 68
4.1.5 Results and discussion 73
4.1.6 Conclusion 73
4.2 Photo-conduction devices 74
4.2.1 Theory and model 74
4.2.2 Optical characterization set-up 79
4.2.3 Results and discussion 82
4.2.4 Conclusion 86
4.3 Summary 87

In the previous chapters, we theoretically studied the THz electromagnetic properties of photo-generated metasurfaces in an InAs slab. Furthermore, the technological process to fabricate the photo-conduction devices and photo-modulated THz devices have been presented. In this chapter, the optical characterization will serve to study the physical properties of the undoped-InAs material. The carrier injection is analyzed by using the fabricated photo-conduction devices in order to estimate the effective carrier lifetime of the photo-carriers. In the following sections, the optical properties of the InAs are investigated experimentally and compared to numerical simulations.

4.1 Physical properties of InAs material

The optical characterization of the InAs material was performed by using photo-luminescence (PL) in the available set-up in NANOMIR-Group at the University of Montpellier. PL is a non-destructive measurement. It is performed by using a cryostat to monitor the sample temperature, a laser pump with a wavelength of $790nm$ to photo-generate free carriers and a FTIR (FTIR: Fourier Transform InfraRed) spectrometer to analyze the emitted light [108, 109, 110]. The FTIR spectrometer is composed of a Michelson interferometer and a high sensitivity detector which measures the interferogram $\mathrm{I}(\Delta x)$. The interferogram contains therefore the entire information of all the wavelengths emitted by the sample. The interferogram is Fourier transformed to obtain the spectrum of the sample [111]. The PL measurement requires

a sufficient resolution. Typical resolutions in FTIR spectroscopy are ranging from 32 to $0.5cm^{-1}$, where $0.5cm^{-1}$ is the highest resolution. The resolution calibration is related to the longer optical retardation, which corresponds to the maximum oscillation amplitude of the movable mirror located in the Michelson interferometer. We used a step scan process to discriminate the PL from the black body radiation.

In the PL measurement, the surface of a crystal semiconductor; (in this case: the undoped-InAs material), is illuminated by a visible laser creating electrons-holes pairs due to the absorption of photons with an energy superior to the energy gap (E_g) (figure4.1(1)). The energy of the IR photons of the laser pump is equal to $1.56eV$. Then, the spontaneous emission spectrum takes place when the photo-excited electron and hole thermalize to the band extrema and recombine spontaneously (figure4.1(2)). The PL experiment proves the fundamental states of the semiconductor. It gives access to the band to band recombination, or more generally to the localized electronics states into the band gap of the semiconductor.

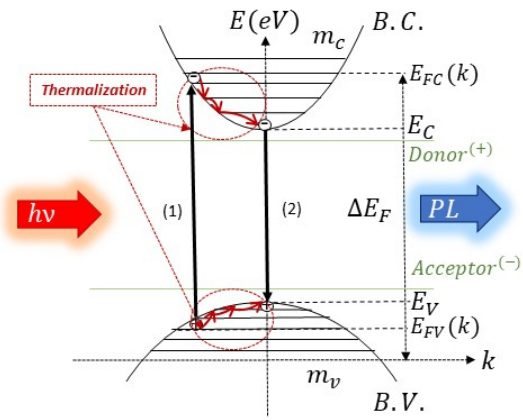

Figure 4.1 – *Schematic of the absorption(1) - emission(2) processes of PL. The PL measurement allows to characterize the spontaneous emission of a material optically pumped. The optical transitions between the valence band and the conduction band are performed with constant k. In other words, they are vertical transitions.*

In the following section, we start with the PL at low-temperature ($10K$) of an InAs wafer. This results are performed by using different pump irradiances in W/cm^2.

4.1.1 Photo-luminescence at low-temperature

This section presents the PL spectra obtained at low-temperature ($10K$) of an undoped-InAs material made by different pump fluences in W/cm^2 (see figure4.2). Figure4.2 shows two PL peaks for each spectra. The first peak located at high-energy corresponds to the band to band free carrier recombination and the second one at low-energy is related to Urbach-Tail [112]. The Urbach-tail corresponds to the absorption coefficient at the photon energy below the optical gap. It corresponds to the material defects that can be observed at low-temperature. These material defects are related to the trap of electron or holes in the energy gap which leads to states in the gap that can be observed in the emission spectra at low-temperature. While most of these defects origin from the material surface, other defects come from

the lack of an atom in the mesh, and impurities in the material. This states in the gap can be observed at low-temperatures because the carriers are trapped in the impurity level. When the temperature increases, the impurities ionize and release the carriers.

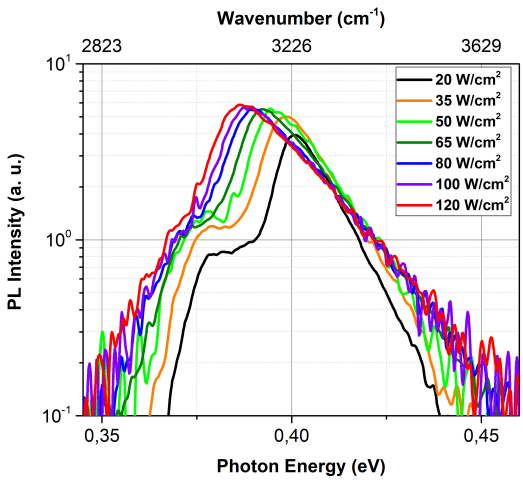

Figure 4.2 – *PL spectra made at low-temperature of an undoped InAs material under laser irradiance spanning between 20W/cm^2 to 120W/cm^2*

We can calculate the temperature of the photo-generated carriers using the high energy part of the PL spectra at low-temperature. This temperature relates to the distribution of the photo-excited carriers in the allowed band. The estimation is given by the Boltzmann distribution presented in the following equation:

$$f(E) = Ae^{\frac{-E}{kT}} \tag{4.1}$$

where A is the PL amplitude, E is the photon energy, k is the Boltzmann constant and T the temperature. To compute electronics temperature of the photo-generated carriers we consider different IR-pump irradiance in W/cm^2. Then, a Boltzmann distribution slope (BDS) is computed by using a nonlinear curve fit which is calculated by using the relation: $A\exp(-x/BDS)$, where A is the PL amplitude. Then, the BDS is divided by kT which give us an estimation of the electronics temperature.

Before computing the electronics temperature, it is necessary to determine the irradiance of the IR pump. It has been performed using a power-meter to monitor the power in mW. The irradiance in W/cm^2 has been obtained by considering an IR-spot diameter of around 200μm. The experimental determination of the spot's geometry of our facilities has been performed by scanning the beam using an infra-red camera (Windowless USB2.0 Monochrome 1.3MP CMOS Cameras (8-bits)). The IR-spot geometry of the incident beam is illustrated in the figure4.3. The gaussian waist in the X-directions is around 100um and in the Y-directions is around 350um which allows us to estimate and IR-spot diameter of around 200μm. The laser divergence is different for the direction due to the diffraction effect produced by the shape of the laser facet. This IR-spot region must be related to the IR-laser power made over this area in W/cm^2. The same procedure has been carried out for different pump fluences at low-temperature presented in Table4.1.

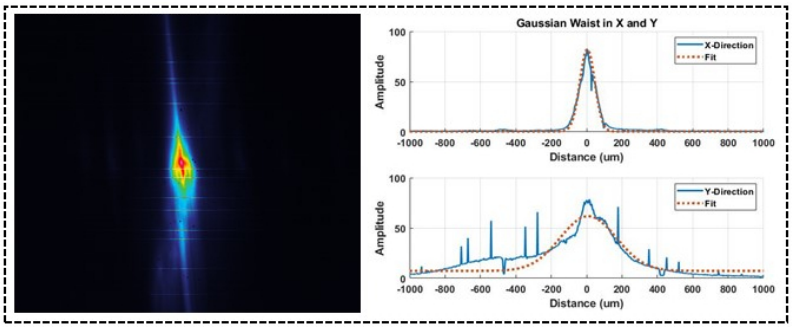

Figure 4.3 – *Gaussian waist in X and Y measurement to determine the IR-spot size by using an infra-red camera. We consider that the IR-spot has a diameter of around* $0.2mm$.

Φ_0 (W/cm^2)	Power-Meter (mW)	BDS $(a.u.)$	Electronics Temperature (K)
20	7	0.0105	122 (Increment in T is $112K$)
35	11	0.0124	144 (Increment in T is $134K$)
50	16	0.0133	155 (Increment in T is $145K$)
65	21	0.0154	179 (Increment in T is $169K$)
80	26	0.0173	201 (Increment in T is $191K$)
100	32	0.0174	203 (Increment in T is $193K$)
120	37	0.0177	205 (Increment in T is $195K$)

Table 4.1 – *Electronics temperature obtained by using Boltzmann distribution slope in the PL at low-temperature (*$10K$*) using different pump fluences in* W/cm^2.

As illustrated in table4.1, the electronics temperature increases by a regular increment of $20K$ until it approximately reaches $193K$ from which it began to plateau despite a very high irradiance of over $80W/cm^2$. It can be explained by the thermalization effect, where $1.2eV$ are dissipated in the form of heat. The cryostat is not able to remove the heat. The important point is at $10K$ the electronic temperature is $100K$ higher due to the thermalization of the photo-generated carriers.

In the following section, we present the PL using different temperatures spanning from $10K$ to room-temperature ($300K$) and a constant laser irradiance. We study the dynamic of the E_g according to the different temperatures and how is it affects the electronic temperature of the photo-generated carriers.

4.1.2 Photo-luminescence at different temperatures

This section deals with the PL spectra obtained at different temperatures of an undoped-InAs material for a laser irradiance of $15W/cm^2$. Figure4.4 shows the evolution of the energy gap (E_g) with the temperature dependence and the increase of its intensity. At high temperatures, the PL allows a reduced E_g. This potential value is low because the increased thermal energy increases the interaction of the inter-atomic spacing due to the increment in amplitude of the atomic vibration (stress). On the contrary, if the PL is at low-temperature, the interaction of the inter-atomic spacing is decreasing due to the weak amplitude of the atomic vibration

which remains the E_g with an increased value. Figure4.4 also shows two maximum intensity of PL when it is at low-temperature. The first peak located at high-energy corresponds to the band to band free carrier recombination and the second one at low-energy is related to material defects that can be observed at low-temperature, as previously explained in section4.1.1.

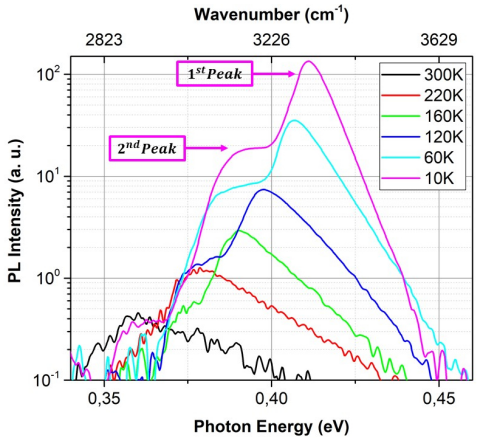

Figure 4.4 – *Evolution of the shape of band-to-band emission spectra with temperature dependence from* $10K$ *to* $300K$ *using an undoped-InAs material and a fixed laser irradiance of* $15W/cm^2$*. When the temperature increases, the* E_g*, the recombination lifetime* τ_r *and the carrier diffusion length* $L_{n,p}$ *decrease in value due to the thermal energy rise.*

4.1.2.1 Varshni's Law

The variation of E_g with the temperature T is given by the Varshni's law [113]

$$E_g(T) = E_g(0) - \frac{\alpha T^2}{T + \beta} \tag{4.2}$$

where, α is a fit parameter and β is the Debye temperature which corresponds to the characteristic temperature of the behavior of the heat capacity and the hardness of the solids. E_g is expressed in eV and T in K. $E_g(0)$ in that case is the gap at $0K$. Figure4.5 presents the dependence between the PL's energy peak and the temperature. Table4.2 indicates the Varshni coefficient values found in the state of the art [114] and its computed coefficient values obtained for the PL $1^{st}Peak$ of the undoped-InAs material. The PL $2^{nd}Peak$ which is related to material defects reports the same Varshni coefficient values. They are in quite good agreement despite the laser heating.

To understand how the energy of the PL-$2^{nd}Peak$; (related to the trap of electron or holes in the gap), is emptied at the PL-$1^{st}Peak$; (band-to-band free carrier recombination), we study the activation energy (E_a). E_a corresponds to the distribution law of electrons both in contact with another state and separated by an energy barrier [115], in that case the E_a. The E_a can be estimated by to the following equation: $exp^{(E_a/kT)}$ where, k is the Boltzmann constant. To compute E_a, it is necessary to calculate the integral of PL at different temperatures in (K^{-1}), presented in

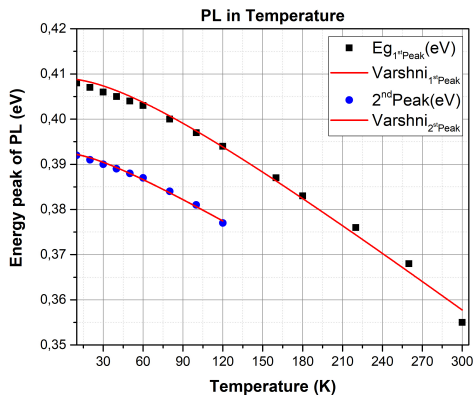

Figure 4.5 – *Estimation of the variation of E_g with the temperature T computed by using the Varshni law presented in table4.2.*

$\alpha(meV.K^{-}1)$	$\beta(K)$	Reference
0.276	93	[114]
0.223	92.21	Linear-fit PL-1$^{st}Peak$ figure4.5.

Table 4.2 – *Varshni coefficient values for the undoped InAs material.*

figure4.6. Moreover, it is also possible to obtain the electronics temperature of the photo-generated carriers by using in this case an irradiance equal to $15W/cm^2$. The estimation is given by the Boltzmann distribution presented in the equation4.1 as presented above. The BDS is also calculated by using a non-linear curve fit which gives an estimation of the electronics temperature.

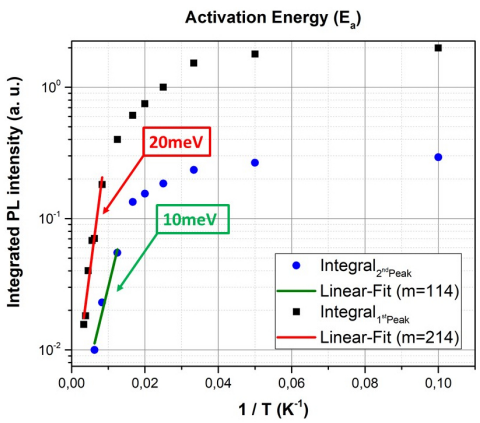

Figure 4.6 – *The E_a is computed by using linear-fit. In this case, the E_a for the PL-1$^{st}Peak$ is around $20meV$ and for the the PL-2$^{nd}Peak$ is around $10meV$. This $10meV$ is close to the energy needed to ionize the impurity band.*

The increase of the electronics temperature when decreasing the sample temperature can be explained by the fact of the thermalization, presented in section4.1 in figure4.1. In that case, the surface of the material that has an $Eg = 0.354eV$ it

Temperature (K)	BDS ($a.u.$)	Electronics Temperature (K)
300	0.027	313 (Increment in T is 13)
160	0.0151	181 (Increment in T is 21)
60	0.00942	109 (Increment in T is 49)

Table 4.3 – *Electronics temperature obtained by using Boltzmann distribution slope in the PL at different temperatures. As the temperature in the PL decreases, the electronic temperature increases.*

is illuminated with a laser with an energy of $1.56eV$ which provokes that $1.2eV$ to be dissipated in the form of heat. Then, when the sample temperature decreases the thermalization energy can be observed with a higher visibility in the electronics temperature. Table4.3 indicates an estimation of the electronics temperature at different PL temperatures, ranging from $313K$ to $109K$.

In the following section, the optical characterization of the PL at room-temperature and its comparison with the theoretical simulation performed at at room-temperature ($300K$) using different pump irradiances in W/cm^2.

4.1.3 Photo-luminescence at room-temperature

This section covers the PL spectra at room-temperature ($300K$) made by different irradiances in W/cm^2. Figure4.7 shows the peak of PL is located at $E_g = 0.354eV$ as the irradiation of the IR-pump increases. The BDS estimation which gives an approximation of the electronics temperature, is calculated from the Boltzmann distribution presented in the Eq.4.1 as illustrated above. The evolution of the electronics temperature depicted in Table4.4. It has similar values (around $320K$) as it is induced for different laser irradiance on the undoped-InAs material at $300K$.

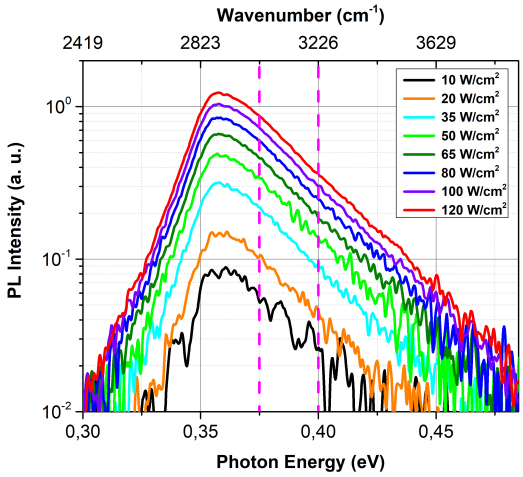

Figure 4.7 – *PL spectra made at room-temperature ($300K$) of an undoped InAs material under IR optical pumping using different irradiance in W/cm^2*

In the following section, we perform the numerical simulation of the PL at $300K$ to estimate the photo-generated carrier density created in the PL using different

Φ_0 (W/cm^2)	Power-Meter (mW)	BDS $(a.u.)$	Electronics Temperature (K)
10	3.5	0.0271	315 (Increment in T is $15K$)
20	7	0.0272	316 (Increment in T is $16K$)
35	11	0.0273	317 (Increment in T is $17K$)
50	16	0.0274	318 (Increment in T is $18K$)
65	21	0.02748	319 (Increment in T is $19K$)
80	26	0.02755	320 (Increment in T is $20K$)
100	32	0.02758	320 (Increment in T is $20K$)
120	37	0.02762	321 (Increment in T is $21K$)

Table 4.4 – *Electronics temperature obtained by using Boltzmann distribution slope in the PL at room-temperature (300K) using different laser irradiance in W/cm^2. The electronics temperature is constant (with a temperature around 320K) as the pump irradiance increases in the PL spectrum.*

pump irradiance in W/cm^2.

4.1.4 Numerical simulation of PL at room-temperature

This section is dedicated to the theoretical study of PL at room temperature ($300K$). The main idea is to have access to more information because the PL process has the same configuration implemented when photo-generated carriers are created in an undoped-InAs slab at $300K$ to modulate the THz waves efficiently. Therefore, this PL study plays a key role in providing us access to an estimation of the radiative carrier lifetime (τ_R) and the radiative recombination coefficient (B).

The surface of the material is illuminated by a laser of a wavelength of $790nm$, which degenerates the surface of the material due to the creation of electron-hole pairs. This degeneration actives two pseudo-Fermi levels (one for the electrons and the other for the holes). In order to estimate the difference in the pseudo-Fermi levels, a home-made multiphysics code has been done. This code requires a creation of an important quantity of photo-generated carriers out of equilibrium Δn and Δp in a way that the pseudo-Fermi levels are given by:

$$E_{Fc} = E_c + kTF^{-}_{1/2}(\frac{n}{N_c}) \tag{4.3}$$

$$E_{Fv} = E_v - kTF^{-}_{1/2}(\frac{p}{N_v}) \tag{4.4}$$

where for the InAs material the effective density of states in the conduction band is: $N_c = 8.7\text{x}10^{16}cm^{-3}$ and in the valence band is: $N_v = 6.6\text{x}10^{18}cm^{-3}$. The $F^{-}_{1/2}$ is the inverse function of $F_{1/2}$, the integral of the Fermi-Dirac function of order 1/2 defined by:

$$F_{1/2} = \frac{1}{\Gamma(3/2)} \int_0^{\infty} \frac{x^{1/2}}{1+e^{x-u}} dx \tag{4.5}$$

where $\Gamma(3/2)$ is the gamma function. Figure4.8 outlines the difference E_{Fc}-E_{Fv} in relation to the carrier density (N) out of equilibrium. InAs material does not absorb more photons of energy hv=E_g when the carrier density out of equilibrium (n_{trans}) is larger than the transparency's threshold. In other words, the transparency

threshold density is the limit of carriers absorption in the InAs material. When this transparency threshold is reached, the material no longer absorbs photons of energy smaller or equal to the considered one. The transparency threshold of the undoped-InAs material is equal to $N = 1.8\text{x}10^{17}(cm^{-3})$.

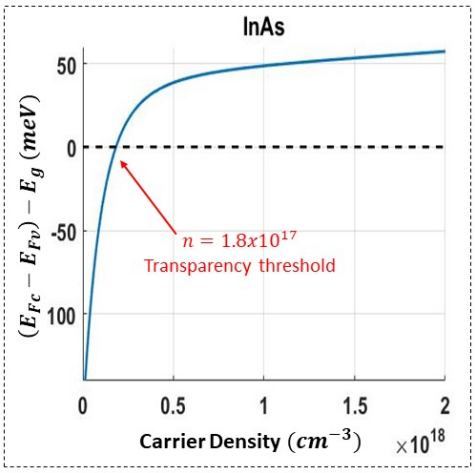

Figure 4.8 – *Evolution of the difference of the pseudo-Fermi level ΔE_F=E_{Fc}-E_{Fv} as a function of the density of carriers out of equilibrium in the undoped-InAs material. The density of transparency is obtained when E_{Fc}-E_{Fv}=E_g.*

The evolution of the difference of the pseudo-Fermi level ΔE_F=E_{Fc}-E_{Fv} allows to compute the photon energy K_{spon} that can be modeled by the following relation:

$$K_{spon} = \frac{(2m_r)^{3/2}}{\pi\hbar^2\tau_R} e^{\frac{\Delta E_F - E_g}{kT}} \tag{4.6}$$

where $\hbar$ is the Planck constant and m_r is the value of the reduced effective mass computed by using m_c=0.023m_0 which is the effective mass of the conduction band; (where m_0 is the electron mass in the vacuum), and m_v=0.41m_0 the effective mass of the valence band as it is presented below:

$$m_r = (\frac{1}{m_c} + \frac{1}{m_v})^{-1} \tag{4.7}$$

The spontaneous lifetime τ_{Rm} is a parameter related to the properties of the material that can be estimated with the following equation:

$$\frac{1}{\tau_{Rm}} = \frac{q^2 n_{op} E_g E_P}{2\pi c^3 \hbar^2 \varepsilon_0 m_e} \tag{4.8}$$

where q is the electron charge, n_{op} is the InAs optical refractive index, E_P is the Kane's energy that corresponds to an element in the dipole matrix of transition from the valence band to the conduction band [89], ε_0 is the vacuum permittivity and m_e is the electron mass. The pseudo-Fermi levels variations are calculated under a high laser irradiance which links radiative recombination mechanisms where B is the bimolecular radiative recombination coefficient that can be estimated by the following equation:

$$B = \frac{1}{\tau_{Rm} N_c} (\frac{m_c}{m_v})^{3/2} \tag{4.9}$$

Numerical calculations of PL has been carried out to have access to the pseudo-Fermi levels variation by using the obtained PL experimental values at room-temperature presented in figure4.7. The theoretical results leads to new approximations values of the bimolecular radiative recombination coefficient equal to $B = 7.28 \times 10^{-11}(cm^3 s^{-1})$ estimated by using equation4.9 considering a $\tau_{Rm} = 2(ns)$. These values are extremely close to reference values obtained in the literature [89] where $B = 8.5 \times 10^{-11}(cm^3 s^{-1})$.

To theoretically determine the spectral distribution $R_{spon}(hv)$ of the spontaneous emission rate in an undoped-InAs material, we use the following equation:

$$R_{spon}(hv) = K_{spon}((hv - E_g)^{1/2} * \frac{1}{\sigma\sqrt{2\pi}} e^{-1/2(\frac{hv-u)}{\sigma})^2})e^{\frac{-(hv-E_g)}{kT}} \tag{4.10}$$

where a convolution operation was added between the density of states; $((hv - E_g)^{1/2})$, and a Gaussian curve with expected value u and variance σ to realize the numerical simulation of the low-energy part of the PL peak which is related to Urbach-Tail.

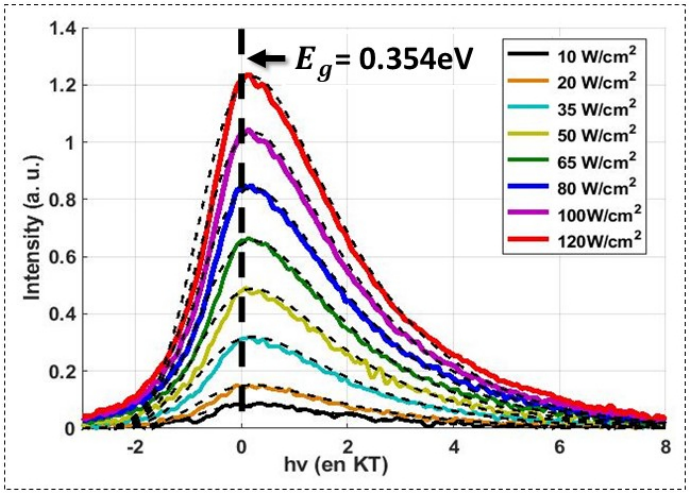

Figure 4.9 – *The comparison between the simulated results (dashed lines) and the experimental ones (full lines) of the spectral distribution of the spontaneous emission rate $R_{spon}(h\nu)$ in $(cm^{-3}.s^{-1}.J^{-1})$.*

Figure4.9 illustrates the PL at room-temperature extracted from the FTIR spectrometer by using a Michelson interferometer measurements for different pump fluences ($\Phi_0 = 10, 20, 35, 50, 65, 80, 100, 120 W/cm^2$) for the InAs material. The comparison between numerical simulation (dashed-lines) and the experimental ones (full-lines) shows very good agreement in the displacement of the pseudo-Fermi levels variation when the InAs material is photo-excited by an IR plane wave. We can also observe the PL maximum intensity which gives us an idea of the material gap size. In this case, the gap of the InAs material is $E_g = 0.354eV$.

The numerical simulations allow us to adjust the physical parameters to fit the experimental data. To find a good fit agreement between the theoretical and the experimental lines, we first normalized the theoretical curve to obtain the same intensity than in the experimental one. Then, we applied a second normalization regarding the Boltzmann's distribution, the density of states and the Urbach-Tail.

The distribution that guides the total normalization is the Boltzmann's distribution since the Urbach-Tail has been computed by an approximation using a convolution operation between the density of states and a Gaussian curve to acquire the low-energy part of the PL peak.

In the following section, we use the parameters obtained in the PL optical characterization under different conditions in order to study the non-linear evolution of the InAs effective recombination life-time according to the injection-level (N).

4.1.4.1 Effective recombination life-time (τ_{eff})

In the undoped-InAs material under a low-injection regime, the minority carriers are metastable and will exist on average only for a time equal to the life-time τ_{eff}. It corresponds to the average elapsed time between the creation of an electron-hole pair and its recombination as previously presented in chapter 2.

To compute the effective life-time curve, we consider an intrinsic InAs slab, where $n_0 = p_0 = n_i = 0.5\text{x}10^{15} cm^{-3}$, $n = n_o + \Delta n$ and $p = p_o + \Delta p$, with $\Delta n = \Delta p$ when we illuminated the sample. We assume that the deep trap of the SRH recombination is located at an energy equal to intrinsic energy level, it means $n' = p' = n_i$. In this context, the SRH recombination is:

$$R_{SRH} = k_r(np - n_i^2) \approx \frac{np - n_i^2}{\tau_{no}(p + p') + \tau_{po}(n + n')} \tag{4.11}$$

where $\tau_{no} \approx \tau_{po} \approx 7.5\text{x}10^{-7} s$. In this scenario, we can determine the τ_{SRH} for an undoped-InAs sample as it follows:

$$\tau_{SRH} = \frac{\Delta n}{R_{SRH}} = \tau_{no} + \tau_{po} \tag{4.12}$$

We also assume that the radiative recombination is given by the following equation:

$$R_{Radiative} = k_r(np - n_i^2) \approx Bnp \tag{4.13}$$

where $B = 0.1\text{x}10^{-11} (cm^3 s^{-1})$ value is very close to the state of the art values presented above. Then, we can determine the $\tau_{Radiative}$ for an undoped-InAs sample as it follows:

$$\tau_{Radiative} = \frac{\Delta n}{R_{Radiative}} = \frac{\Delta n}{B({n_i}^2 + 2n_i\Delta n + \Delta n^2)} \tag{4.14}$$

We also can assume that the Auger recombination may be written by:

$$R_{Auger} = k_r(np - n_i^2) \approx C_n n^2 p + C_p p^2 n \tag{4.15}$$

where $C_n \approx C_p \approx 0.25\text{x}10^{-27} (cm^3 s^{-1})$. These values are close to reference value [96]. We can determine the τ_{Auger} for an undoped-InAs sample as it follows:

$$\tau_{Auger} = \frac{\Delta n}{R_{Auger}} = \frac{\Delta n}{C_n(n_i + \Delta n)^3 + C_p(n_i + \Delta n)^3} \tag{4.16}$$

Before concluding, to determinate the effective lifetime for an undoped-InAs slab at different injection level by the following equation:

$$\frac{1}{\tau_{effective}} = \frac{1}{\tau_{SRH}} + \frac{1}{\tau_{Radiative}} + \frac{1}{\tau_{Auger}} \tag{4.17}$$

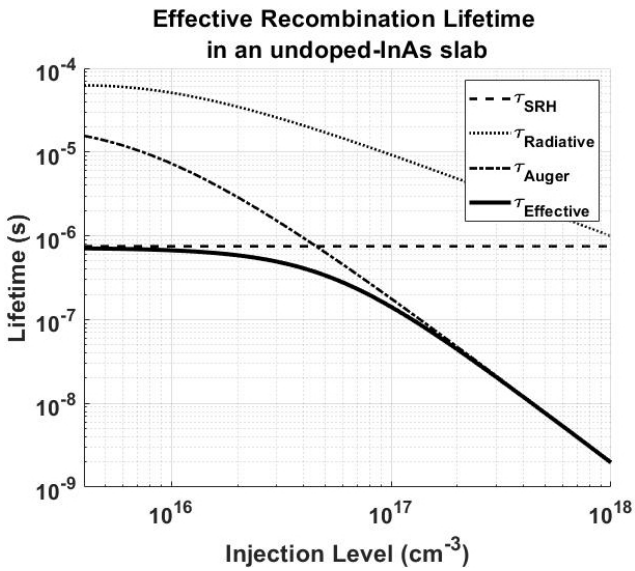

Figure 4.10 – *Evolution of the effective life-time of the InAs material according to the injection-level. The theoretical life-time of SHR, Radiative and Auger are used to model the effective recombination lifetime.*

The carrier recombination life-time is driven by the injection level as shown in the figure4.10. Figure4.10 shows the evolution of the effective life-time (τ_{eff}) with the injection level dependence. We can observe that the non-linear effect modify τ_{eff} in a range of variation [$\tau_{eff} \approx 7 \times 10^{-7}(s)$ - $\tau_{eff} \approx 2 \times 10^{-9}(s)$].

4.1.4.2 Photo-generated carrier density (N)

The PL graph presented in figure4.9 shows the pseudo-Fermi levels variation when the material is illuminated at different pump irradiances. Each pump irradiance level can theoretically be associated with a photo-generated carrier density (N) presented in Table4.5. This numerical calculation of N represents how the conduction and valence band are filled due to the photo-generation process.

In order to perform the numerical calculation of N, we used a laser spot diameter equal to $0.2mm$. We can thus estimate the IR-spot intensity (in W/cm^2) on the laser spot region. It allows to deduce the number of photons projected on this region considering that the photon energy equals to $1.56eV$ according to the PL laser pump wavelength, in this case $\lambda = 790nm$, which leads to a value in $cm^{-2}s^{-1}$. Here, we assume that a photon generates an electron-hole pair. Afterwards, the photo-excited carrier density is located in an InAs slab of a variable thickness (h), which will be distributed by diffusion mechanism through the thickness of the material in $cm^{-3}s^{-1}$. Finally, the obtained value has to be pondered with the effective recombination lifetime τ_{eff} (s) due to the different pump fluences implemented in the PL to obtain the induced photo-generated carrier concentration in cm^{-3}. The same procedure has been carried out for different pump irradiances at room-temperature presented in Table4.5.

Φ_0 (W/cm^2)	Power-Meter (mW)	N (cm^{-3})
10	3.5	N $\approx$ 2.6x10^{15}
20	7	N $\approx$ 5.3x10^{15}
35	11	N $\approx$ 9.3x10^{15}
50	16	N $\approx$ 1.3x10^{16}
65	21	N $\approx$ 1.7x10^{16}
80	26	N $\approx$ 2.1x10^{16}
100	32	N $\approx$ 2.6x10^{16}
120	37	N $\approx$ 3.2x10^{16}

Table 4.5 – *Theoretical estimation results of the photo-generated carrier density N being induced in the undoped-InAs material of thickness ($h = 15\mu m$) in PL experiment at 300K. These N values depend on the diffusion length.*

4.1.5 Results and discussion

In this section, experimental and theoretical results concerning the optical characterization of PL by using the experimental technique FTIR spectroscopy to study the optical properties of the undoped-InAs material in temperature, at low-temperature and, at room-temperature ($300K$) were presented. Using Varshni's law, the maximum energy of the PL peak in different temperatures, and under a specific IR-optical pump (at $15W/cm^2$); is directly related to the E_g. This impacts the recombination and the diffusion length values. Analyzing the PL at low-temperature ($10K$), E_g does not increase when different pump irradiances are applied in the material. Furthermore, in the three optical characterization cases, the electronics temperature of the photo-generated carrier have been computed to study the thermal behavior of the undoped-InAs material when it is photo-generated.

Moreover, the photo-generated carrier density created in the PL at room-temperature has been theoretically estimated using the effective recombination lifetime τ_{eff} which is driven by the injection level N. We can observe that the non-linear effect modify τ_{eff} in a range of variation [$\tau_{eff} \approx 7\times10^{-7}(s)$ - $\tau_{eff} \approx 2\times10^{-9}(s)$]. It means that, we can expect a range of speed modulation rate for the THz absorption from 2.6MHz (considering $N \approx 10^{16}(cm^{-3})$) to 0.5GHz (considering $N \approx 10^{18}(cm^{-3})$).

We must insist more on the variation of the PL rather than the absolute value, because we cannot estimate accurately the value of τ_{eff} for the numerical calculation of N in the Table4.5. To have a better estimation and validation of the τ_{eff}, it will be important to perform photoconduction experiments in order to estimate more precisely the effective lifetime of the minority carriers in the InAs material.

4.1.6 Conclusion

In this section, experimental and theoretical results concerning the optical characterization of PL by using the experimental technique FTIR spectroscopy and numerical simulations to study the optical properties of the undoped-InAs material at different temperatures, at low-temperature and, at room-temperature were presented. We experimentally verifies the behavior of the InAs material under different

conditions when it was photo-excited by an IR laser pump. Furthermore we have theoretically study the excess carrier lifetime τ_r showing that the evolution of the effective lifetime τ_{eff} varies according to the level injection $N(\tau_{eff})$.

In the following section, we are interested in studying the minority carriers diffusion length applied in the PL in order to estimate more precisely the effective lifetime of the minority carriers in the InAs material. To have a better estimation and validation of τ_{eff}, we carried out the photoconduction experiments. The objective is to determinate an estimation of the ambipolar diffusion length under different injection levels.

4.2 Photo-conduction devices

This section is devoted to the experimental determination of the ambipolar diffusion length in an InAs slab. It was performed by the laser beam induced current (LBIC) [116] technique applied to a transmission line measurement (TLM) [99]. Measurements of minority-carrier diffusion length have potential use in material characterization for quality assessment and device design [117].

This section starts with the presentation of the theory and model to establish simple expressions of the photo-current decay induced by the scanning of a laser light in an InAs slab. Based on numerical simulations, we show different photo-current regimes by using different injection levels controlled by the pump and the procedure to extract the diffusion length of the minority carriers in an InAs slab.

4.2.1 Theory and model

The technique used for measuring the diffusion length consists of a laser beam focused at the surface of an InAs slab. The photo-generated carriers created in the semiconductor diffuse in all directions due to the free carriers concentrations gradients. Then, the photo-generated carries are collected by the ohmic contacts when a weak voltage is applied between both contacts of the TLM device. The complete geometry and composition of the TLM devices has been previously presented in chapter technological fabrication. Figure4.11 illustrates the TLM structure fabricated for measuring the laser beam induced current.

4.2.1.1 Photo-carriers distribution

The study of the photo-carriers distribution is carried out by considering a non-intentionally n-doped InAs sample ($n_i = 10^{16}(cm^{-3})$), of $2L$ length and thickness d. The InAs slab undergoes to an external voltage (V_a), and a normal incident laser illumination with a wavelength of $\lambda = 790nm$ or an energy equal to $1.5eV$ and an irradiance $I(W/cm^2)$. A mask limits the illuminated region to a window of width ($2l$) which covers the whole width of the InAs sample, as presented in figure4.12. In this analysis, the intensity of the IR irradiation is given by $I = \Phi_0 h\nu$, where Φ_0 is the incident photon flux and $h\nu(eV) = 1.24\lambda(\mu m)$. Hence, the incident photon flux can be estimated by:

$$\Phi_0 = \frac{W/cm^2}{h\nu(J)} = 5 \times 10^{18} I(W/cm^2)\lambda(\mu m) \tag{4.18}$$

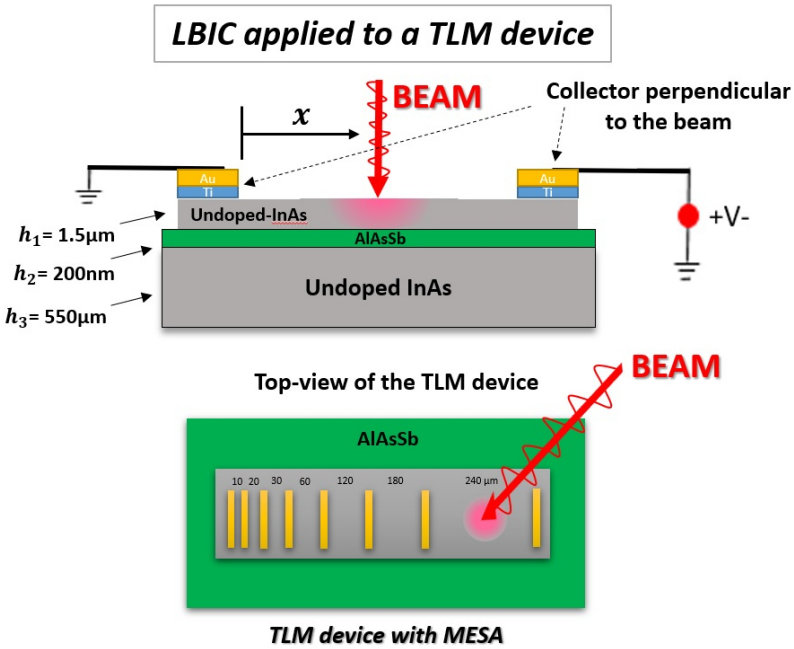

Figure 4.11 – *Schematic of the TLM device with mesa based on InAs material.*

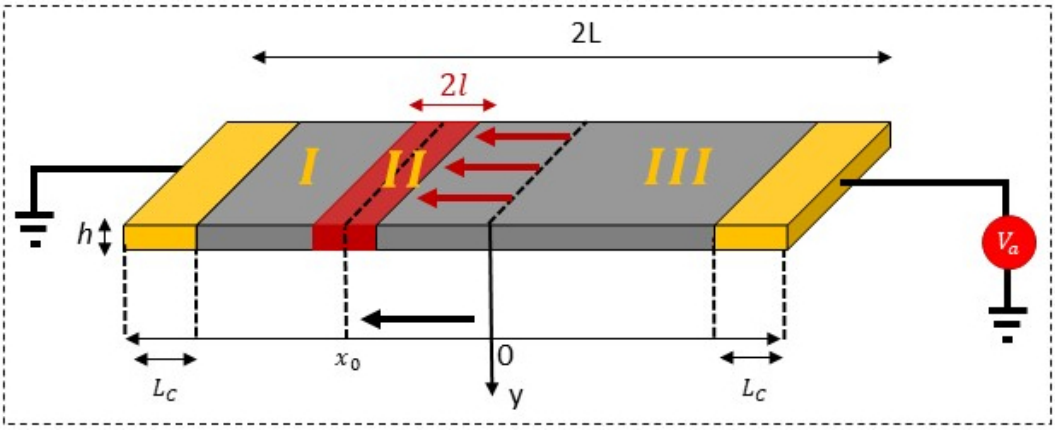

Figure 4.12 – *Schematic of the geometry used to perform numerical simulations of the photo-conduction device.*

The pump illumination is constant when the window moves over the entire surface of the TLM. Here, we consider a stationary regime, hence: $\frac{\partial \Delta N}{\partial t} = 0$. The analytic expression of the diffusion equation which describes the photo-generated carriers induced by the irradiation of a focused infra-red laser beam can be established by :

$$L_n{}^2 \frac{d^2 \Delta N}{dx^2} + L_E \frac{d\Delta N}{dx} - \Delta N = -G^{opt} \tau_n \tag{4.19}$$

with $L_n = \sqrt{D_n \tau_n}$ which is the diffusion length, τ_n the recombination lifetime and the length L_E resulting from the electric field E_a due to the the applied voltage V_a is:

$$L_E = \mu_n E_a \tau_n \tag{4.20}$$

where $E_a = V_a/(2(L - L_c))$ where L_c is the contact length. G^{opt} is the optical generation rate which is given by:

$$G^{opt}(y) = (1 - R)\Phi_0 \alpha e^{-\alpha y} = \Phi\alpha \tag{4.21}$$

We can assume a homogeneous excitation throughout the thin thickness of the InAs sample ($h = 1.5\mu m$) because the diffusion length is larger than h and the surface recombination can be neglected and we can say that $G^{opt} = (1 - R)\Phi_0\alpha$ where R is the reflection coefficient of the IR light ($R_\Phi = 0.34$), and α is the absorption coefficient of the InAs material ($\alpha = 75100cm^{-1}$ at $790nm$ [97]). The general solution of the equation4.19 is determined by the conditions of continuity of ΔN and its derivative in $x = \pm l$. Thus, we obtain the following expressions:

$$\Delta N_I = \Phi\alpha\tau_n \frac{2L_2}{(L_1 + L_2)} sh(l/L_2) e^{\frac{x}{L_2}} \tag{4.22}$$

$$\Delta N_{II} = \Phi\alpha\tau_n (1 - \frac{L_1}{L_1 + L_2} e^{(-x-l)/L_1} - \frac{L_2}{L_1 + L_2} e^{(x-l)/L_2}) \tag{4.23}$$

$$\Delta N_{III} = \Phi\alpha\tau_n \frac{2L_1}{(L_1 + L_2)} sh(l/L_1) e^{\frac{-x}{L_1}} \tag{4.24}$$

where L_1 and L_2 are the expressions of the effective diffusion length correlates to L_n and L_E. It occurs when the InAs sample is polarized by a voltage (Va). These expressions are written as follows:

$$L_1 = \frac{2L_n^2}{{L_E}^2 + \sqrt{{L_E}^2 + 4{L_n}^2}} \tag{4.25}$$

$$L_2 = \frac{2L_n^2}{-{L_E}^2 + \sqrt{{L_E}^2 + 4{L_n}^2}} \tag{4.26}$$

In equation4.25 and equation4.26, it must be considered the condition that ($L_E << L_n$) in order to minimize the influence of the E-field in the diffusion length of the photo-excited carriers. Figure4.13 shows the effect of V_a induced over the photo-generated carrier distribution. The numerical simulation result of the photo-carrier distribution will be presented in the next section.

In general, the photo-excited carriers (ΔN) created by the laser are obtained by the integration of the photo-carrier decay linked to the normal carrier diffusion over the entire collector surface (L_c).

$$\Delta\bar{N}(x) = \frac{1}{L_c} \int_L^{(L+L_c)} \Delta N(x) dx \tag{4.27}$$

where (L_c) is the length of the fabricated ohmic contact whose size is $L_c = 50\mu m$.

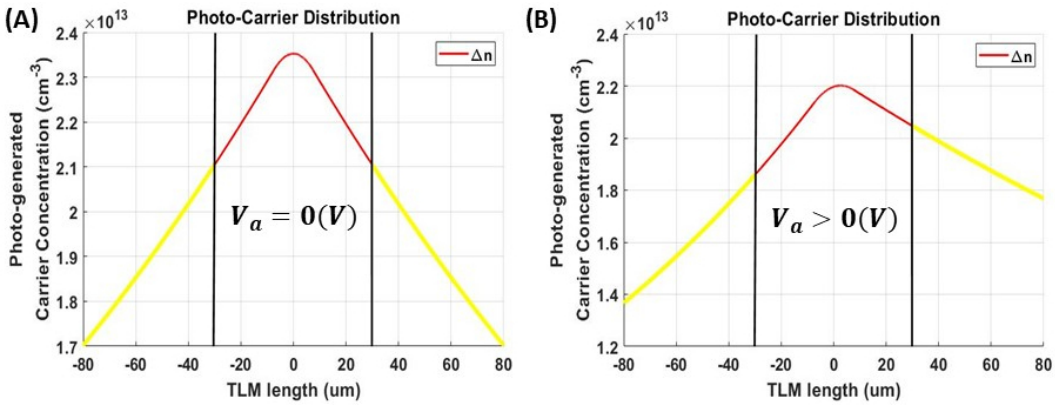

Figure 4.13 – *Electric field influence in the diffusion length of the photo-generated carrier distribution: (A)* $V_a = 0(V)$ *and (B)* $V_a > 0(V)$*. IR spot diameter* $2l = 15\mu m$

4.2.1.2 Numerical simulation of the photo-carrier distribution

The numerical simulations allow us to adjust the physical parameters to fit the experimental data. The experimental parameters are: the wavelength laser, its spot size, the illumination, the doping and geometry of the InAs slab, the InAs carrier mobilities at room-temperature (μ_n - μ_p), the applied E-field resulting from the applied voltage ($E_a = 70V/cm$), and the ohmic contact geometry ($L_c = 50\mu m$). The photo-carrier distribution is traced according to the position of the laser spot spanning over the entire surface of the n-doped InAs material.

The simulation results of the photo-carriers distribution induced by using different pump irradiances are presented in figure4.14. Figure4.14 shows the electrons (red-color) and holes (blue-color) distribution in the InAs material which has an intrinsic carrier concentration of $n_i = 10^{16} cm^{-3}$ (green-color), and the photo-carrier underneath the ohmic contact (yellow-color). The illustration of the photo-carriers distribution is complex to calculate since τ_{eff} gives a non-linear behavior by using different pump irradiances. Under this assumption, a rough description is presented for the photo-generated electrons and holes distribution. At high-pump irradiance (see figure4.14-C), the carrier distribution is governed by the radiative recombination mechanism where the effective recombination life-time is very short, around $\tau_{eff} = 10^{-8}(s)$. It illustrates the small amount of minority carrier density, (in this case the holes); that arrives at the contact and the photo-current signal observed by the ohmic contact is very low. On the contrary, when the pump irradiance is reduced (see figure4.14-B), the photo-carrier distribution shows that a major amount of holes are collected by the ohmic contact due to the fact that the effective lifetime is larger around $\tau_{eff} = 10^{-7}(s)$. However, when low-pump irradiance is applied (see figure4.14-A), a big amount of minority carriers reach the contact due to the larger life-time $\tau_{eff} = 6.5 \times 10^{-7}(s)$. This fact shows that when the n-type InAs material is irradiated with a low-pump injection, the photo-carriers distribution is controlled by the minority carriers concentration (holes $< p >$).

The fact of applied an E-field on the ohmic contacts, control the position of the minority carriers (holes). Therefore, the E_a application must be very small in order to not influence the electron and holes diffusion length ($L_n + L_E \approx L_n$ and

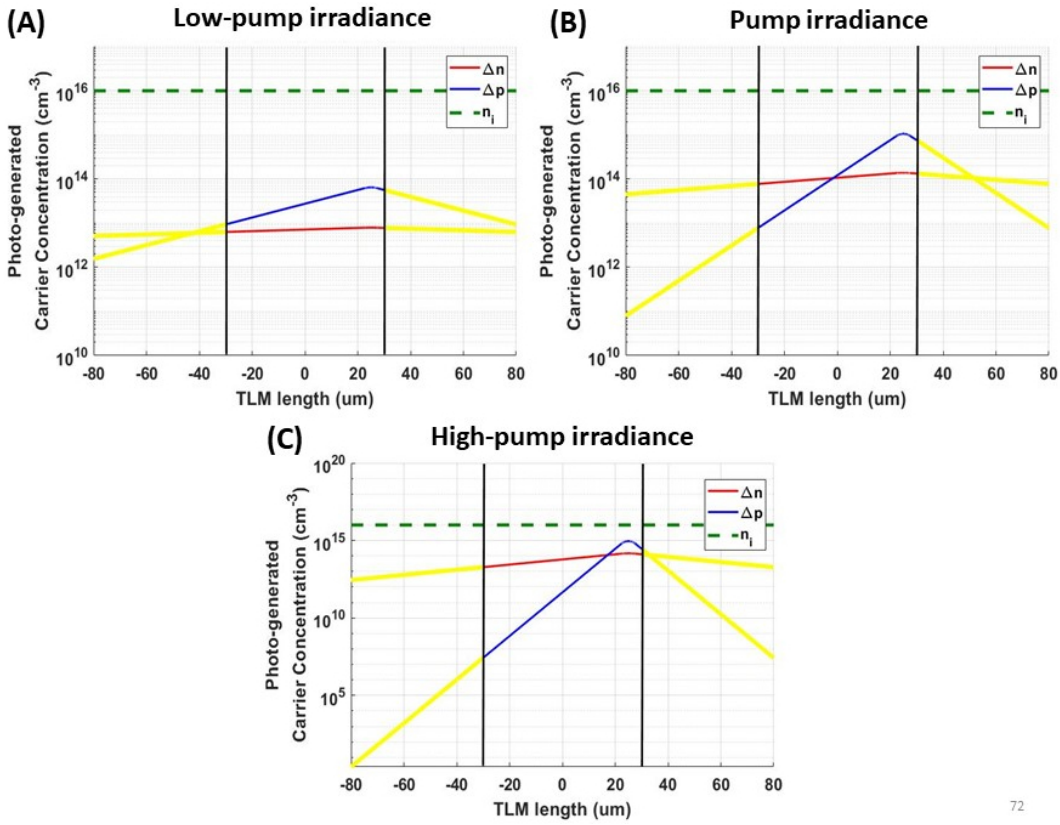

Figure 4.14 – *Simulation results of the photo-carriers distribution under different laser pump illuminations at low-pump irradiance, medium-pump irradiance and high-pump irradiance.*

$L_p + L_E \approx L_p$).

At last, figure4.14 shows that the photo-generated carrier density (N) is much lower than expected when the InAs material is irradiated with high, medium and low-pump injections. This is due to the electrons and holes diffusion mechanisms makes them move much fast. Therefore, the optically excited carriers can not exceed the intrinsic carrier density of the InAs material equal to ($n_i = 10^{16} cm^{-3}$), as presented in figure4.14.

4.2.1.3 Theory of the measurements

To determine the effective diffusion length (L_{eff}), we apply a constant voltage at each side of the TLM structure. The voltage is low enough (for example $V = 7V$) to guarantee a L_E smaller compared to L_{eff}:

$$L_{eff} >> L_E \tag{4.28}$$

We limit the influence of the applied internal electric-field in the TLM structure. Then, the addition of the average excess carrier concentration by the laser beam induced current (LBIC) technique in the InAs material provokes an excess current in

the InAs slab. This excess current is equivalent to a resistivity modification Δp or a conductivity modification $\Delta\sigma$ that we will measure [118].

LBIC measurement is a non-damaging technique for determining various semiconductor parameters, including minority carrier diffusion length [119]. The LBIC curves depend on the sample geometry, thickness, and on the surface recombination velocity s of the scanned surface. In this context, Oliver and Dixon [117] expressed the laser beam induced current as a function of the distance between the beam and a perpendicular collector (see figure4.15) to determine the diffusion length. The model required a thin sample semiconductor of thickness h and with infinite recombination rate at the surfaces. In this situation, there is always an exponential decay of the LBIC that can be expressed by the following relation:

$$I \approx I_0 e^{-x/L_{eff}} \tag{4.29}$$

where I_0 is a constant and L_{eff} is the effective diffusion length. Since the fabricated TLM devices have a thin InAs sample of $1.5\mu m$, the decay of the LBIC; (which corresponds to the average excess carrier concentration) follows a decreasing exponential law immediately beyond the illuminated area with decay constant L_{eff} as the beam is scanned from the ohmic contact to the consecutive one located at the opposite side of the TLM structure [120].

This simple form of diffusion length extraction suggests that measuring the slope of a $ln(LBIC)$ curve would yield $1/L_{eff}$, a very straightforward and practical method of analysis [117]. The extraction of the effective diffusion length L_{eff} is driven by the effective recombination lifetime (τ_{eff}) that has been previously presented in the PL section, which relates the injection-level vs the recombination carrier-lifetime with all its recombination mechanisms (SRH - Radiative - Auger) [121, 90]. In this work, the surface recombination related to the ohmic contact is neglected since the extraction of L_{eff} is limited to the slope of a $ln(LBIC)$ curve.

4.2.2 Optical characterization set-up

The optical characterization of the TLM devices was performed by using a home-built microscope combined with a focusing system to obtain a very small laser spot diameter [122]. The optical set-up is presented in figure4.15.

The experimental set-up is similar to a standard optical microscope. The only differences are a laser pump with a wavelength of $\lambda = 785nm$ and a webcam CCD. The laser has an adapted focusing system to obtain a spot of $5\mu m$ diameter or more, and it will be observed by using the adapted camera. In this scenario, it is possible to perform the scanning method of an infrared spot over the entire surface of the TLM device thanks to the spatial resolution. The photo-current is measured by using a Lock-In amplifier. It has been digitized by using a computer.

The figure4.15 illustrates the basic principle of the home-built optical set-up. The TLM sample is photo-excited using a laser beam focused by a microscope objective (20X provided by Newport: 20x magnification, 0.4 numerical aperture, $1.56mm$ working distance, $9mm$ of effective focal length and infinity corrected). The laser beam is filtered by a beam expander (2 lens of focal length of $25.4mm$ and $100mm$) and a pin-hole of $50\mu m$ diameter. The beam expander enter the 20x objective. This optical arrangement allows to reduce the size of the laser beam to $5\mu m$ diameter but considering lens aberrations around $15\mu m$ diameter. The illumination of the TLM

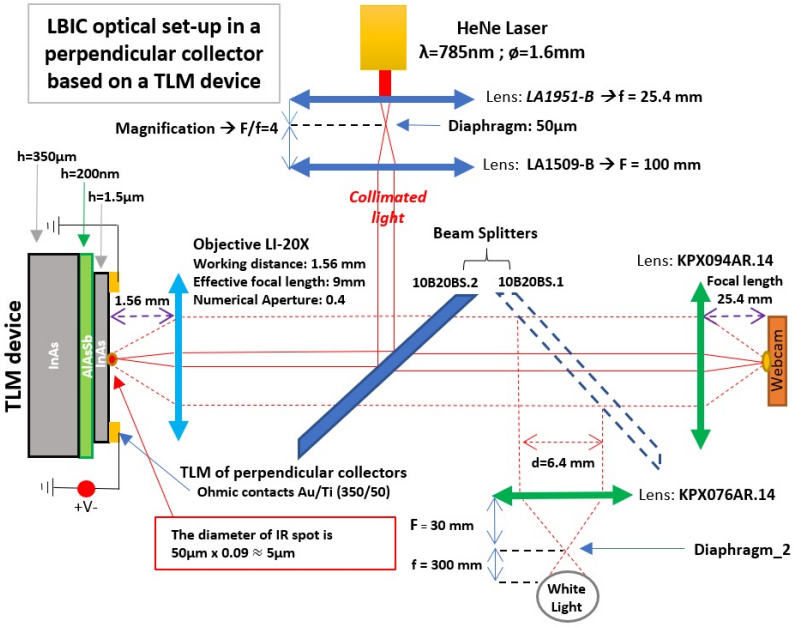

Figure 4.15 – *Schematic beam path of the home-built experimental optics set-up.*

surface is performed by white-light lamp source through the microscope objective. The CCD camera images the surfaces where we performed the photo-conduction measurements.

The TLM devices are mounted on a TO-8 holder chip-carrier, presented in figure4.16-A. A specific electronic platform has been designed to allow the photo-conduction measurement, as illustrated in figure4.16-B. The TLM device is connected to a voltage supply in serie with a resistance $R_{Lock-In}$ of known value as schematized in figure4.17.

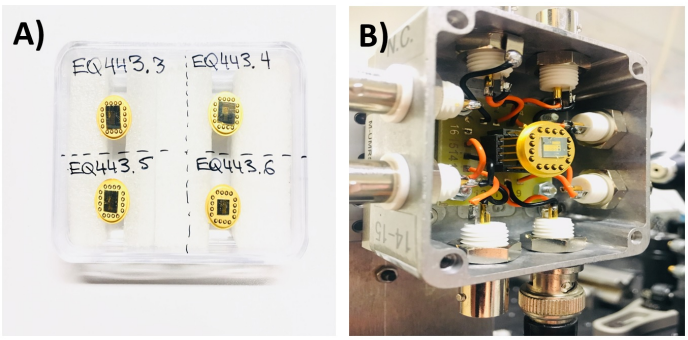

Figure 4.16 – *(A) TLM devices on the TO-8 chip-carrier. (B) Electronic platform created to measure the photo-current signal received by the photo-conduction device.*

The resistance of the TLM device is equal to $(R_{TLM} - 2R_c)$. Therefore, it is important to know the real value of the contact resistance (R_c) and the value of each TLM distance (R_{TLM}).

We use (I-V) measurements in the photo-conduction devices to extract an estimated value of the (R_c). It has been done in the clean-room for different distances

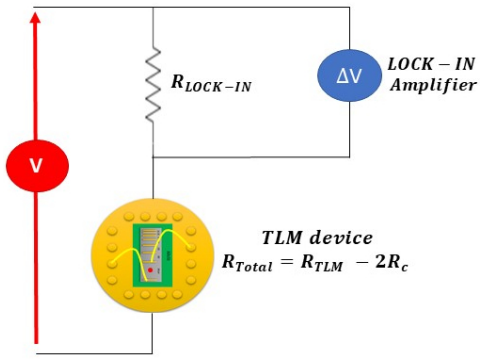

Figure 4.17 – *Schematic of the electrical circuit implemented to measure the photo-current.*

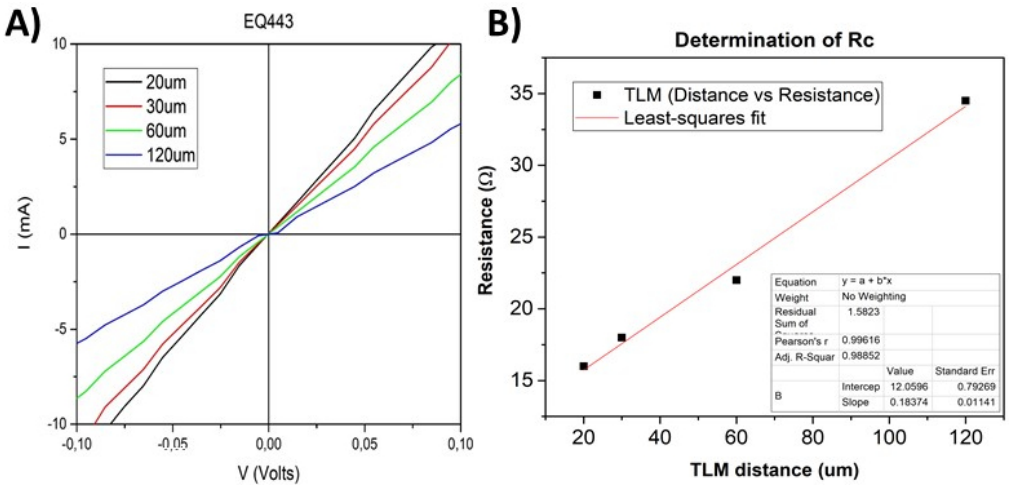

Figure 4.18 – *(A) I-V curves of the TLM devices with different distances (20μm - 30μm - 60μm - 120μm) between both contacts. (B) Linear-fit performed by using the resistance results. The interception with the y-axis corresponds to* $(2R_c)$. *Here Rc=6Ω.*

($20\mu m$ - $30\mu m$ - $60\mu m$ - $120\mu m$) between the TLM contacts. Figure4.18-A shows the I-V curves obtained for each TLM devices varying the distance between both contacts. They correspond to ohmic devices. The table4.6 presents the results of the respective resistance in (Ω). To determine the TLM contact resistance (R_c), a linear-fit curve has been performed by using the previous results presented in table4.6. The y-axis intersection value of the linear-fit curve presented in figure4.18-B is equivalent to $2R_c$ which correspond to the contact resistance. The intersection value is equal to 12, therefore the value of Rc=6Ω.

At last, to monitor the carrier density that is being photo-generated in the InAs slab, we use an infrared power-meter to measure the pump power illumination at the end of the microscope objective in (mW). The laser power has been measured out of the focus plan of the objective of the microscope to avoid any degradation of the power meter. The values are gathered in Table4.7. The irradiance is calculated considering the spot size ($5\mu m$ or more). It is then possible to calculate the photo-generated

TLM length (μm)	ΔI (V)	ΔI (mA)	R_{Total} (Ω)
20	0.16	10	16
30	0.18	10	18
60	0.2	8.9	22
120	0.2	5.76	34.5

Table 4.6 – *Experimental results of the respective resistance in (Ω) performed for different distances (20μm - 30μm - 60μm - 120μm) between the TLM contacts.*

carrier density (N) (Table4.7).

To perform the numerical calculation of N, we used the power-meter values in mW (presented in the first row of Table4.7) and we consider an IR-spot diameter equal to 15μm due to the lens aberrations. Thus, we estimate the IR-spot intensity in W/cm^2 (presented in the second row of Table4.7) on the laser spot region. It allows to deduce the number of photons projected on this region considering that the photon energy equals to 1.56eV according to the laser wavelength, in this case $\lambda = 790nm$, which leads to a value in $cm^{-2}s^{-1}$. Here, we assume that a photon generates an electron-hole pair which leads to a photo-generated carrier density (we consider a 30% of reflection photons on the InAs material). Afterwards, the photo-excited carrier density is distributed through the InAs slab of thickness of $h = 1.5\mu m$ in $cm^{-3}s^{-1}$. Finally, the obtained value has to be pondered with the effective recombination lifetime $\tau_{eff}(s)$ due to the different pump injection implemented in the laser beam to obtain the induced photo-generated carrier concentration in cm^{-3}. The same procedure has been carried out for different laser irradiances at room-temperature presented in Table4.7.

4.2.3 Results and discussion

In order to extract the effective diffusion length results, the pump fluence is limited in order to keep the carrier density lower than $N = 3 \times 10^{16}(cm^{-3})$ where the diffusion length and the minority carriers lifetime are relatively independent of the injection level. It is considered according to the results obtained in the photo-carrier distribution.

The TLM resistance of 60μm length was monitored by an multimeter and it is equal to 16.2Ω, therefore, the $R_{TLM} = 4.2\Omega$ due to the contact resistance $R_C = 12\Omega$. In this work, we consider a maximum carrier density in the order of $N = 3 \times 10^{16}(cm^{-3})$ according the experimental values extracted from the table4.7.

Figure4.19 shows a room temperature plot of different voltages V applied over the TLM device of 60μm length. $R_{LOCK-IN}$ is a resistance of 50Ω and allows to measure a ΔV due to the modulated photo-generated current. The photo-excited carriers has been created by a modulated irradiation $\Phi_0 = (6W/cm^2)$ at 500Hz which corresponds to a carrier density $N = 1.5 \times 10^{16}(cm^{-3})$. Figure4.19 illustrates that when a low voltage V is applied, the distribution of the photo-current is homogeneous. On the contrary, when a larger voltage is applied, the photo-current is peaked at one end of the ohmic contact. This is due to the increased electric field, E_a, that appears into the TLM device (Table4.8). When E_a increases, the photo-carrier distribution is moved to the ohmic contact that collect the minority carriers. However, as the

Power-Meter (mW)	Φ_0 (W/cm^2)	N (cm^{-3})
0.008	4	$N \approx 7.0 \times 10^{15}$
0.01	6	$N \approx 1.1 \times 10^{16}$
0.02	12	$N \approx 2.1 \times 10^{16}$
0.1	60	$N \approx 1.1 \times 10^{17}$
0.15	85	$N \approx 1.8 \times 10^{17}$
0.2	115	$N \approx 2.1 \times 10^{17}$
0.3	160	$N \approx 2.8 \times 10^{17}$
0.5	265	$N \approx 4.9 \times 10^{17}$
0.65	375	$N \approx 6.7 \times 10^{17}$
0.7	400	$N \approx 7.0 \times 10^{17}$
0.85	475	$N \approx 8.4 \times 10^{17}$
0.97	550	$N \approx 9.8 \times 10^{17}$
1.0	580	$N \approx 1.1 \times 10^{18}$
1.2	680	$N \approx 1.3 \times 10^{18}$

Table 4.7 – *Experimental values for monitoring the photo-generated carrier density N that is being photo-generated in the photo-conduction device (last row). We use a power-meter (first row, in mW) and the calculated irradiance in W/cm^2 (second row).*

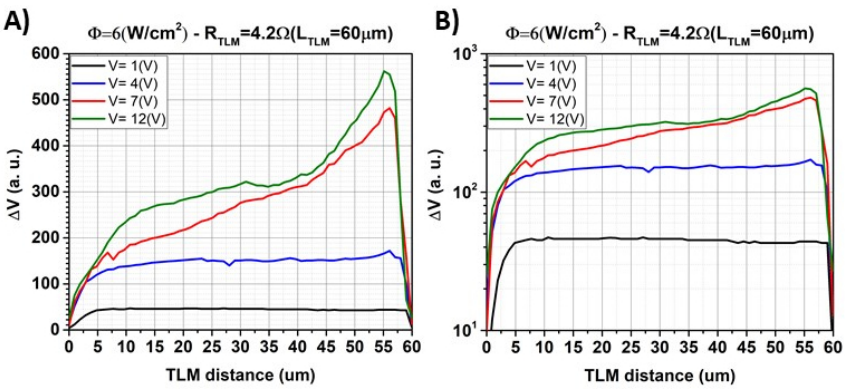

Figure 4.19 – *(A) Experimental results of the minority carrier distribution when the InAs slab is under a low-pump irradiance. Different voltages (V) have been applied to observe the influence in the photo-carrier distribution. (B) Presentation of the same results with y-axis in Log scale.*

voltage increased the plot used to determine the effective diffusion length became increasingly non-linear, as is shown in figure4.19-A. For example, for $V = 12(V)$, the increased electric field moves the photo-carrier distribution to the ohmic contact that collect the minority carriers. The same situation of increased electric-field is observed when high pump irradiances are applied, however, we concentrated our work in low-pump irradiance because it is counterproductive to illuminate the InAs sample with high pump injection due to the τ_{eff} became very short, as we mentioned earlier.

Figure4.20 shows the voltage signal ΔV in (mV) obtained when spanning the

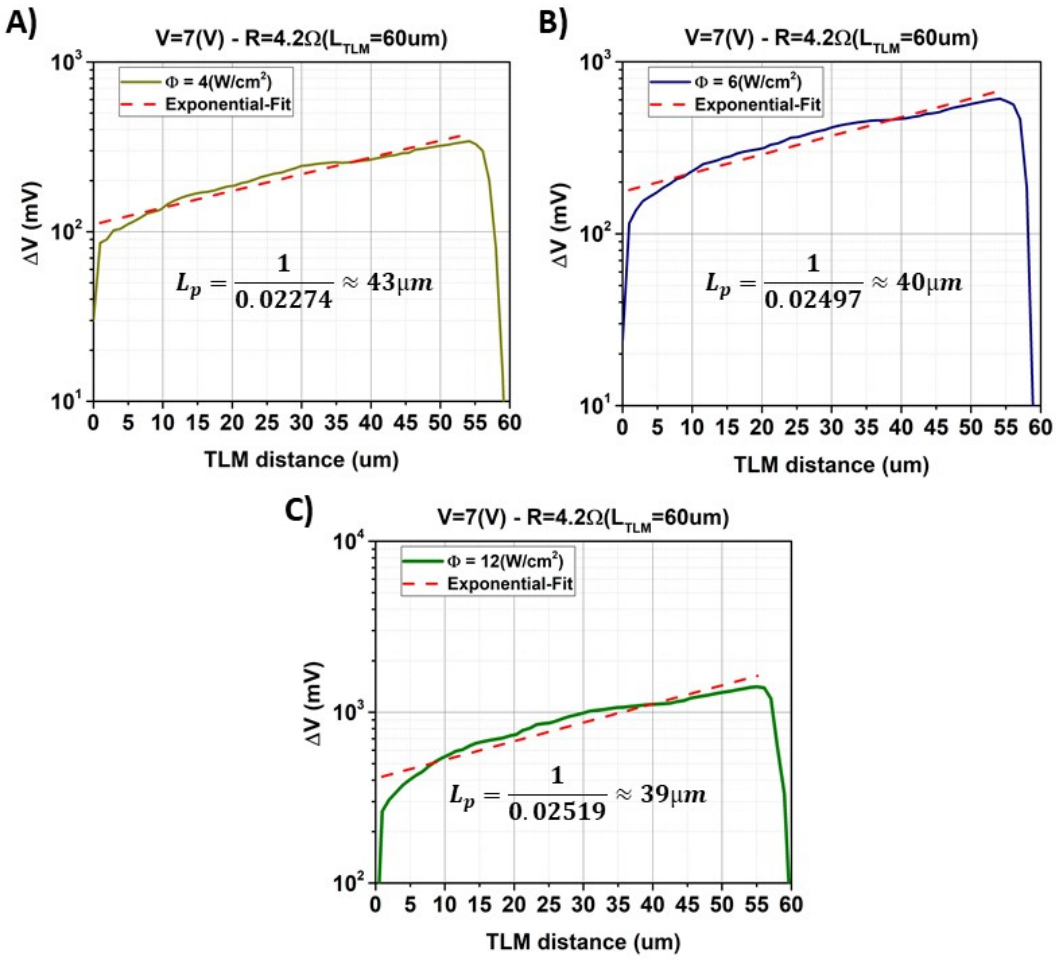

Figure 4.20 – *Experimental results of the minority carrier diffusion length collected by the ohmic contacts. A linear fitting of the exponential decay of the data yields an experimental effective diffusion length* $L_{eff} \approx 40\mu m$. *The vertical axis is in log scale.*

distance of the illuminated spot over all the TLM devices. A linear fitting curve of the experimental data with a log function yields an effective diffusion length L_{eff} of around $40\mu m$.

The comparison between numerical simulations presented in figure4.21, and the experimental ones presented in figure4.20 shows a good agreement in the value of the effective diffusion length. In the numerical result, the parameter that we use to fit the values between the experimental and the numerical simulations was the carrier lifetime recombination. At low-pump irradiation regime the τ_{eff} is controlled by the minority carriers (holes-τ_p) as studied in the carrier-distribution section, therefore, the value of the $\tau_{eff} = 6.5 \times 10^{-7}(s)$. In the theoretical calculations, we consider a slightly n-doped InAs slab of $n_i = 10^{16}(cm^{-3})$, which corresponds to the intrinsic carrier concentration of the InAs slab used in the experimental determination of L_{eff}.

To evaluate the influence of the E-field applied to the TLM structure we use equation4.20. We obtained an additional diffusion length for the electrons L_{En}

V (V)	I (A)	V_{TLM} (V)	E-field (V/cm)
1	0.01	0.042	7
4	0.05	0.21	35
7	0.1	0.42	70
12	0.17	0.714	119
15	0.24	1	167

Table 4.8 – *The TLM device of $L_{TLM} = 60\mu m$ and $R_{TLM} = 4.2\Omega$ allow us to monitor theoretically the electric current value that is circulating in the structure (last row, in V/cm). We use different voltages (first row, in V) to estimate the amount of current circulating in the TLM device (second row, in A) and the calculated voltage that undergoes in the TLM device V_{TLM} (third row, in V).*

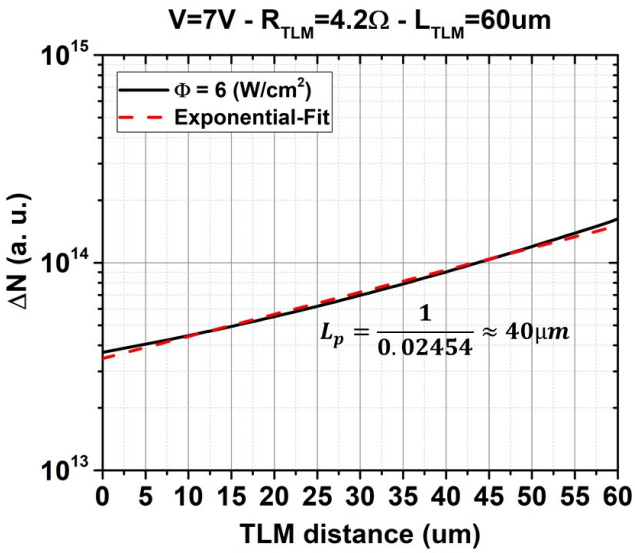

Figure 4.21 – *Theoretical result of the minority carrier diffusion length. A exponential fitting curve to the theoretical data yields an theoretical minority carrier diffusion length $L_p \approx 40\mu m$.*

and the holes L_{Ep}. They are $L_{En} = 3\mu m$ and $L_{Ep} = 41nm$. These diffusion length can be neglected compared to the diffusion length due to the carrier diffusion $L_n \approx 200\mu m$ and $L_p \approx 40\mu m$. Therefore, we have respected the condition presented in equation4.28 as we know that $L_{eff} \approx 40\mu m$.

Before concluding, we study the determination of the minority carriers diffusion length according to the injection-level and the doping of the InAs material. The minority carrier diffusion length for the holes and for the effective diffusion length (or ambipolar diffusion length L_a) are driven by the effective carrier lifetime (τ_{eff}). The τ_{eff} curve has been implemented to know how the value of the minority carrier diffusion length has changed regarding the doping of the material.

To compute theoretically the minority carrier diffusion length, we consider the InAs material diffusion coefficient at room-temperature (300K) for electrons $D_n = 854(cm^2/s)$, for the holes $D_p = 11.9(cm^2/s)$ and for the ambipolar diffusion $D_a =$

$23.5(cm^2/s)$. The minority carrier diffusion length can be obtained by using the following equation:

$$L = \sqrt{D\tau_{eff}} \tag{4.30}$$

When we consider an undoped-InAs material ($n_i = n = p$) and if we applied photo-generation process ($\Delta n = \Delta p$), the ambipolar diffusion coefficient is equivalent to

$$D_a = \frac{(n+p)D_nD_p}{pD_p + nD_n} \approx 2D_p \tag{4.31}$$

However, if we consider n-doped InAs slab with an intrinsic carrier concentration ($n_i = n \gg p$). It means that, when we applied photo-generation process the quantity of holes is much lower than the electrons. In this scenario, the ambipolar diffusion coefficient is equivalent to

$$D_a = \frac{(n+p)D_nD_p}{pD_p + nD_n} \approx D_p \tag{4.32}$$

Figure4.22 shows the theoretical determination of the minority carriers diffusion length according to the injection-level and the doping of the InAs material. The $L_{Ambipolar}$ curve is considers an intrinsic InAs material ($n_i = n = p$). The L_p curve is considering a n-doped InAs slab ($n_i = n \gg p$). This results demonstrate that the ambipolar diffusion length is also driven by the material doping level. The comparison between experimental and theoretical results shows good agreement in the determination of the InAs ambipolar diffusion length.

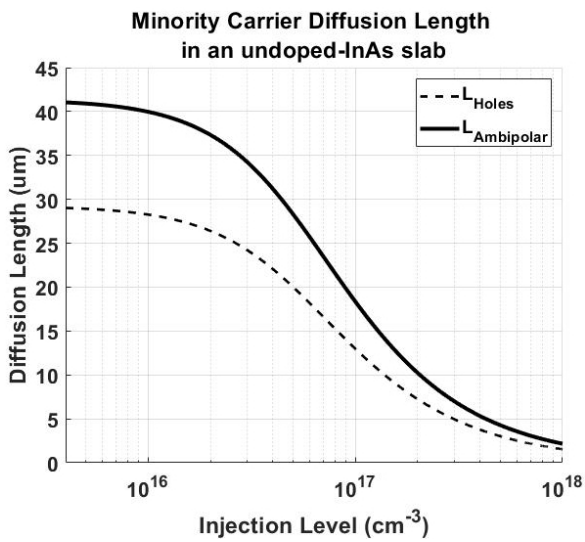

Figure 4.22 – *Estimation of the minority carrier diffusion length. The L_{eff} evolution allows to find an optimal $L_{eff} \approx 40\mu m$ which is in the order of an injection level $N \approx 10^{16}(cm^{-3})$ and for an effective life-time around $\tau_{eff} \approx 6.5 \times 10^7(s)$.*

4.2.4 Conclusion

In this section, experimental and theoretical results concern the optical characterization of the photo-conduction devices by using a new home-built platform.

The construction of this new experimental set-up in our laboratory, as well as the implementation of specific experimental techniques, such as the use of TLM to measure the diffusion length of minority carriers, have been an essential part of this work.

We devoted this work to measure the holes diffusion length at low irradiance where the diffusion length and the minority carriers lifetime are relatively independent of the injection level. This fact allows us to compute the holes diffusion length. A linear fitting of the experimental data yields an holes effective diffusion length $L_{eff} \approx 40\mu m$. The comparison between numerical simulations shows very good agreement. We use the carrier lifetime recombination to fit the diffusion length values. In this scenario, the corresponding carrier lifetime that best fit the experimentally effective diffusion length with the numerical simulation was $\tau_{eff} \approx 6.5 \times 10^{-7}(s)$.

4.3 Summary

In this chapter, the experimental and theoretical results for the study of the optical characterization of the physical properties of InAs material, and the photo-conduction devices were presented.

Firstly, the optical characterization of PL by using the experimental technique FTIR spectroscopy and numerical simulations to study the optical properties of the undoped-InAs material at different temperatures, at low-temperature and, at room-temperature were presented. We experimentally verified the behavior of the InAs material under different conditions when it is photo-excited by an IR laser pump. Furthermore we have theoretically studied the excess carrier lifetime τ_r showing that the evolution of the effective lifetime τ_{eff} varies accordingly to the level injection $N(\tau_{eff})$.

Secondly, experimental estimation of the ambipolar diffusion length obtained by implementing optical characterization in photo-conduction devices (TLM). We carrier out experiments and numerical calculations of the optical characterization in photo-excited InAs membranes using a CW laser with an irradiance of only tens of W/cm^2. A linear fitting curve of the experimental data yields an experimental effective diffusion length $L_{eff} = 40\mu m$. We use the carrier lifetime recombination τ_{eff} to fit the diffusion length values L_{eff}.

In the following section, we are interested in performing the experiments concerning the THz transmission modulation by taking into account the measured L_{eff} and estimated τ_{eff}.

Chapter 5

Photo-driven THz modulator

5.1 THz modulation samples: InAs membranes 89
5.1.1 Experimental set-up 90
5.1.2 Optical characterization of the InAs membranes 91
5.1.3 Photo-modulation of the transmission of the InAs membranes 93
5.1.4 Conclusion 99
5.2 Photo-driven THz modulator 100
5.2.1 Optical characterization set-up 100
5.2.2 Static photo-driven THz modulator 101
5.2.3 Dynamic photo-driven THz modulator 109
5.2.4 Conclusion 114
5.3 Summary 115

After the presentation of the theoretical background in the Chapter 2, we theoretically studied the THz electromagnetic properties of photo-generated carriers in an InAs slab. In this chapter, we study the physical properties of the intrinsic InAs slab using optical characterization and the THz electromagnetic properties driven by the photo-generated carriers in an InAs slab. We show a high modulation of the THz transmission up to 100% from 0.75THz to 1.1THz at very low pump irradiance in the continuous wave regime. We also demonstrate a high-speed transmission modulation rate up to the MHz range with a modulated pump. In the following sections experimental and numerical results concerning the optical characterization of the photo-driven THz modulator are presented.

5.1 THz modulation samples: InAs membranes

This section deals with the optical characterization of the InAs membranes to study the THz electromagnetic properties of photo-generated carriers in an InAs slab. After demonstrating theoretically the efficient modulation of the THz waves [75], we now aim to prove it through experimentations. The optical characterization was performed using a Bruker Vertex 70 FTIR spectrometer, composed by a home-built transmission set-up with a fixed angle of incidence (perpendicular to the surface of the InAs slab), installed in the sample compartment of the FTIR. This set-up is used to realize the optical characterization of the InAs membranes stuck to the gold sample holder previously fabricated.

5.1.1 Experimental set-up

The experimental set-up consists of flat holder with two holes of $2mm$ diameter (one for the sample holder and the second for the reference calibration), mounted on a X and Y directions of translation arms presented in figure5.11-A. The collimated light beam emitted from the internal THz source of the FTIR spectrometer illuminates the InAs membrane located in the sample holder of the set-up, which in turns is traversed by an IR laser pump, as shown in figure5.11-B, which is focalized by using a flat mirror. Then, the signal transmitted from the InAs membrane is collected by the detector. This set-up is small enough to fit into the sample's compartment of the FTIR. It is mainly used to determine the very small thickness of the InAs slab and the THz modulation in transmission from 10THz to 1THz.

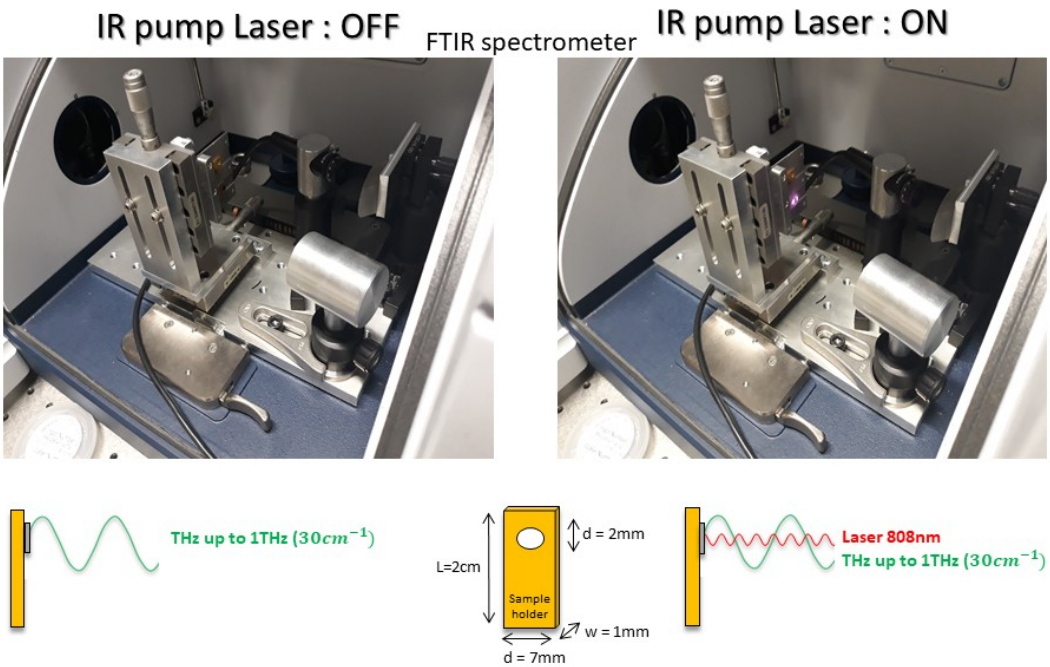

Figure 5.1 – *Home-built transmission set-up of the InAs membranes located inside of the FTIR internal sample chamber with (A) IR-pump laser tuned-off and (B) turned-on.*

Two different configurations of the FTIR spectrometer will be implemented for measurements in different spectral ranges and with different accessories [108]

• For FTIR measurements by using a globar middle-infrared (MIR) light source with a silicon beam splitter, a pyroelectric deuterated triglycine sulfate (DTGS) detector is used for the spectral range from $12000cm^{-1}$(359THz) to $125cm^{-1}$(3.75THz).

• For FTIR measurements by using a water cooler H_g lamp source for the far-infrared (FIR) with a silicon beam splitter, and a silicon bolometer detector cooled at 4.2K is implemented for the spectral range from $650cm^{-1}$(19.5THz) to $30cm^{-1}$(1THz).

5.1.2 Optical characterization of the InAs membranes

In the previous chapter, we performed the technological manufacturing for the fabrication of the THz modulation samples: InAs membranes with a micrometric-thick slab between ($5.7\mu m$ - $8.8\mu m$). We used wet chemical etching to reduce the thickness of the sample and to smooth the surface, which is crucial for the optical characterization, as presented below.

The objective of this section is to figure out the thickness of the InAs membranes. Then, the InAs membranes are spectrally characterized by using a Bruker Vertex 70 FTIR spectrometer with a MIR source, a silicon beam splitter and a DTGS detector. In this scenario, all the transmitted spectra have been performed in the spectral range from $125cm^{-1}$ to $3500cm^{-1}$ as presented in figure5.3. Since the laser is $\Phi_0 = 0W/cm^2$, the light is transmitted through the InAs membrane, as shown in figure5.2.

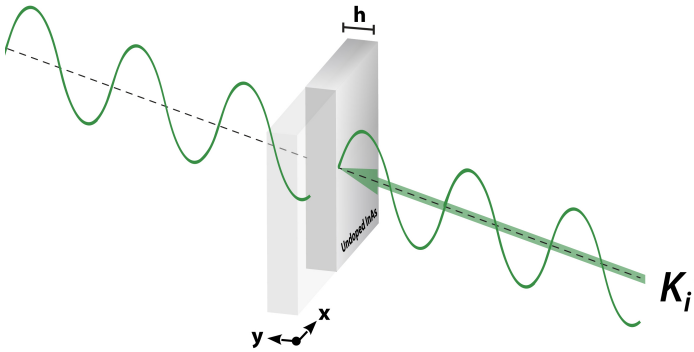

Figure 5.2 – *Schematic of the focused light beam;(green-color), emitted from the internal THz source of the FTIR spectrometer, which illuminates the InAs membrane. Then, the signal transmitted through the slab is collected by the DTGS detector.*

Figure5.3 shows that the transmission spectra corresponds to Fabry-Perot interferences. The fringes spacing is related to the thickness (h) of the InAs slab cavity by:

$$h = \frac{\Delta\lambda}{2\Re(n_\infty)} = \frac{1}{2\Re(n_\infty)\Delta\nu} \tag{5.1}$$

where $\Delta\lambda$ is the difference in wavelength, $\Delta\nu$ is the difference in wavenumber ($\nu \pm 2\delta\nu$) and $\Re(n_\infty)$ is the real part of the refractive index which at these frequencies can be approximated by a constant value. For the InAs material $\Re(\varepsilon_\infty) = 11.4$. The estimation of the InAs's thickness is calculated with the equation5.1 applied for four fringes (four in this case: e.g. $\Delta\nu/4 \pm 2\delta\nu/4$). Table5.2 shows the thickness of each InAs membranes. Remark, the results presented in table5.2 are only an estimated values because we do not know exactly the value of the refractive index at higher frequencies (after phonons's band). Notably the refractive index value is not constant [96]. To validate these thicknesses, it is necessary to model the optical characterization of the InAs membrane in the THz spectral range. We use the model previously developed in Chapter 2 to deduce the thicknesses of each one of the membranes with more accuracy.

The interference peak intensity is linked to the sample surface quality. The figure5.3 shows that the membranes manufactured by solid source MBE and wet chemical etching have a higher transmission intensity value than the sample manufactured by mechanical polishing and wet chemical etching. It can be explained by the fact that the wet chemical etching does not fully remove the roughness of the surface of the polished membrane: it leaves some scratches of the mechanical polishing on the relief of the surface. The roughness affects the amplitude of the interference effect due to the limited InAs thickness. At last, the figure5.3 illustrates that the interference are observed when the InAs has a dielectric behavior at a wavelength smaller than the bandgap $E_g = 2855cm^{-1}(0.354eV)$.

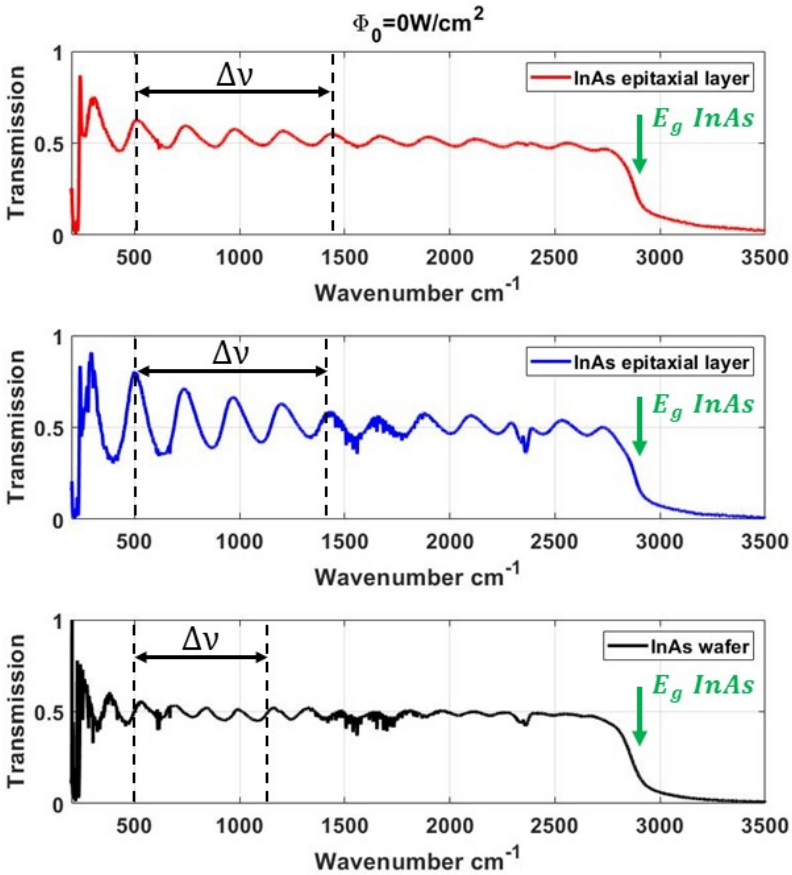

Figure 5.3 – *The InAs membranes optically characterized by using a FTIR spectrometer in transmission. The obtained transmission spectra corresponds to Fabry-Perot resonance which links the cavity's thickness of the InAs membrane; (h=5.7um(red-color),h=6.2um(blue-color) and h=8.8um(black-color)).*

In this section, the optical characterization consists in the fact that the surface of the InAs slab is illuminated by the THz wave and it is transmitted through the InAs membrane. To estimate the THz radiation transmitted through the sample, a new home-made multiphysics code have been created. The objective of this code is to validate the thickness of the InAs membrane (presented in Table5.2), implementing the refractive index values at THz frequencies. This code supposes that the InAs slab of thickness (h) is illuminated by a THz wave. Then, we can

$\nu \pm 2\delta\nu$ (cm^{-1})	h (μm)
259	5.7 ± 0.5 (red-color)
238	6.2 ± 0.5 (blue-color)
168	8.8 ± 0.5 (black-color)

Table 5.1 – *Experimental results of InAs slab thickness. Results obtained by using FTIR spectrometer with a MIR source and Fabry-Perot cavity resonance equation5.1.*

FTIR spectroscopy at MIR: $h(\mu m)$	THz transmission: $h(\mu m)$
5.7 ± 0.5 (fig.5.3-(red-color))	5.9 ± 0.2 (fig.5.4-A)
6.2 ± 0.5 (fig.5.3-(blue-color))	6 ± 0.2 (fig.5.4-B)
8.8 ± 0.5 (fig.5.3-(black-color))	8.3 ± 0.2 (fig.5.4-C)

Table 5.2 – *Higher accuracy result of the InAs slab thickness obtained by the transmission spectra at THz frequencies. The adequated fitting procedure in the THz range allows to estimate the thickness of the membranes with more accuracy than using Fabry-Perot interferences in the MIR.*

estimate a more accurate value of the InAs's thickness by using the THz transmission spectra. Moreover, to compare the numerical simulations results at THz frequencies, new optical characterization of the InAs membranes were performed. The InAs membranes are spectrally characterized by using the same FTIR spectrometer but with a FIR source to make the detection up to the THz range. In that case, a silicon beam splitter accompanied by a silicon bolometer detector cooled at $4.2K$ is implemented for the spectral range from $600cm^{-1}$ (18THz) to $30cm^{-1}$ (1THz).

The transmission spectra extracted from the FTIR measurements for different InAs membranes are shown in Figure5.4. The comparison between the simulated results (dashed-lines) and the experimental ones (full-lines) shows good agreement with a slight increase in the experimental transmission despite the geometrical imperfections in the InAs membrane surface. The difference between the experiment and the numerical simulation is mainly due to the roughness of the InAs surface that affects the amplitude of the FTIR measurement and the refractive index inaccuracy at this frequency range that affects the numerical simulation. Table5.2 presents a summary of the two techniques used to obtain a very accurate estimation of the thickness of each InAs membrane.

5.1.3 Photo-modulation of the transmission of the InAs membranes

This section is dedicated to the optical characterization of photo-excited InAs membranes as shown in figure5.5. The InAs membrane is photo-excited by using a laser of wavelength equal to $\lambda = 808nm$. The photon energy is around $1.53eV$. The laser diameter is $\phi = 3mm$ and the power $500mW$. The rest of the home-built transmission set-up is similar than the previous section5.1.2.

The InAs membranes are photo-excited at different pump irradiances and spectrally characterized by using the same Bruker Vertex 70 FTIR spectrometer with

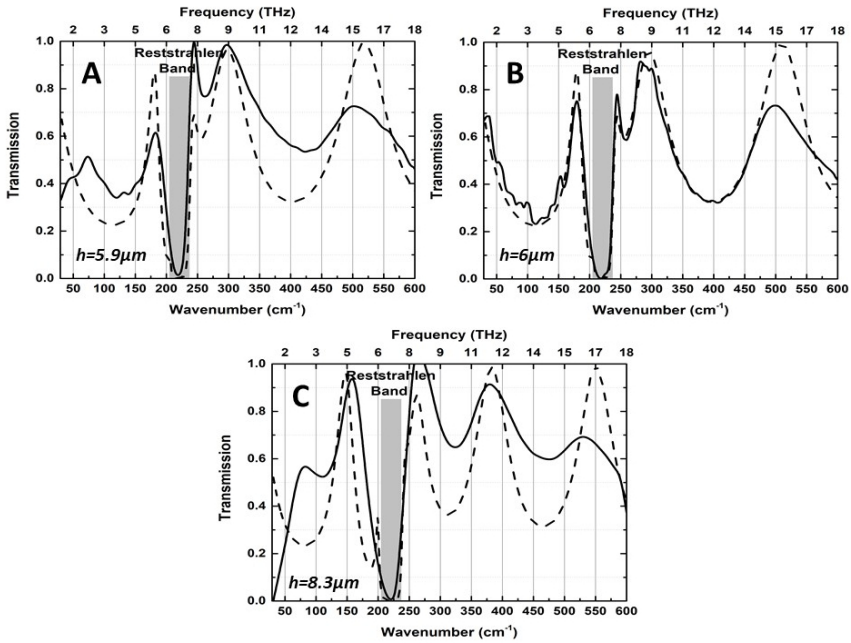

Figure 5.4 – *The comparison between the numerical simulations results (dashed lines) and the experimental ones (full lines) for different InAs membranes. The thickness of each InAs membrane is presented in Table5.2*

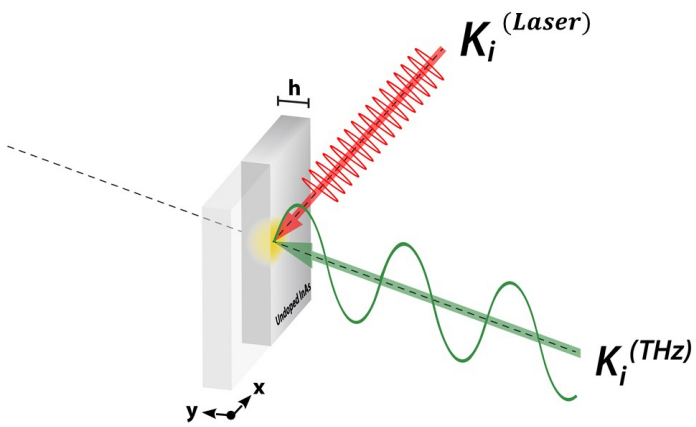

Figure 5.5 – *Schematic of the InAs membrane of thickness "h" illuminated by a focused THz beam; (green-color), emitted from the cooled Hg source of the FTIR spectrometer. The InAs slab is pumped by a collimated IR plane wave (red-color). Then, the signal transmitted is collected by the silicon bolometer detector at 4.2K.*

a water cooler H_g lamp source for the FIR, a silicon beam splitter and a silicon bolometer detector cooled at $4.2K$. In this scenario, all the transmitted spectra have been performed in the spectral range from $30cm^{-1}$ to $600cm^{-1}$ as presented in figure5.6. The THz radiation passes through the InAs membrane, some of the THz radiations are absorbed, reflected, or transmitted. The transmitted spectra of the InAs membrane of thickness h =$6\mu m$ obtained using different pump irradiances is

shown in figure5.6. This result illustrates the first experimental demonstration of THz waves modulation driven by photo-generated carriers in an InAs slab.

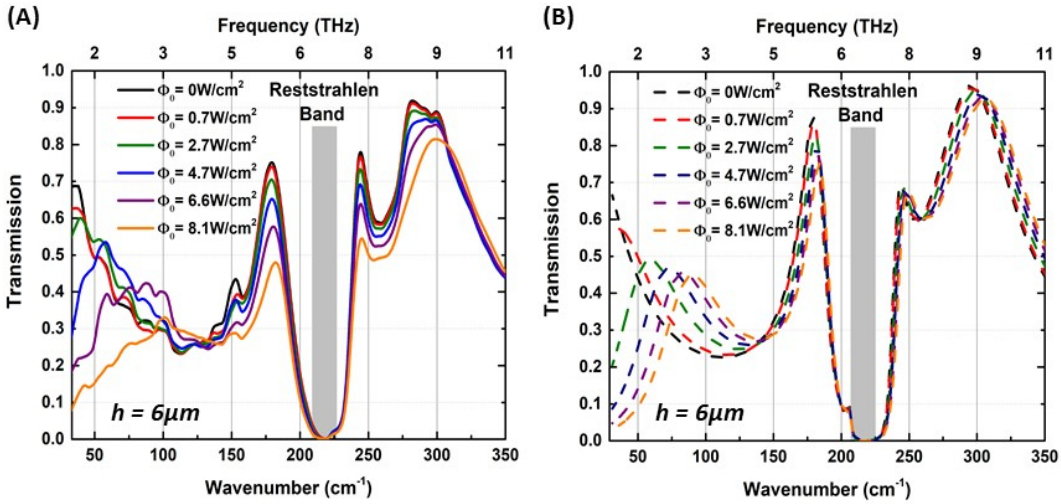

Figure 5.6 – *InAs slab of $h = 6\mu m$ (A) Experimental results of the THz transmission modulated by using different pump irradiances from $\Phi_0 = 0W/cm^2$ to $\Phi_0 = 8.1W/cm^2$. (B) Theoretical results of the THz transmission. It is observed good agreement between experiment and theory at different pump irradiances from $\Phi_0 = 0W/cm^2$ and $\Phi_0 = 8.1W/cm^2$.*

Figure5.6-A illustrates the THz transmission spectra using different pump irradiances from $\Phi_0 = 0W/cm^2$ to $\Phi_0 = 8.1W/cm^2$. The map of transmission coefficient obtained by using the FTIR measurements with respect to the wavenumber in cm^{-3} (or frequency in THz) and the THz transmission intensity show that the THz transmission is driven by the IR plane wave at different pump irradiance. When the laser is $\Phi_0 = 0W/cm^2$, a transmission between 25% to 70% is reached for a broadband frequency range spanning from 4THz ($125cm^{-1}$) to 1THz ($30cm^{-1}$). For a laser irradiance of $\Phi_0 = 8.1W/cm^2$, the transmission coefficient attains 5% at 1THz. To verify this assertion, we plot the numerical simulations of the THz transmission spectra with a laser irradiance of $\Phi_0 = 8.1W/cm^2$ and without laser pump ($\Phi_0 = 0W/cm^2$), as presented in figure5.6-B. The comparison between the numerical simulation (dashed-lines) and the experimental ones (full-lines) shown good agreement in the displacement of the transmitted spectra when the InAs membrane is photo-excited by an IR plane.

These results suggest that the photo-generated structure in the thin InAs membrane of $h = 6\mu m$ corresponds to a homogeneous metallic slab (HS). To verify this assertion, we plot the real part of the relative permittivity for the same spectral broadband. In this framework, the real permittivity of an un-pumped InAs slab is represented in figure5.7-A-1. The average real part of the relative permittivity is shown to be a dielectric constant value when the wavenumber increases. We observe a transition from 6.5THz ($217cm^{-1}$) to 7THz ($233cm^{-1}$), this is related to the Reststrahlen band where the real permittivity varies in a very strong manner. This dielectric constant value (see figure5.7-A-1) is accompanied of a null THz absorption since the InAs is a dielectric, as presented in figure5.7-A-2. For a laser

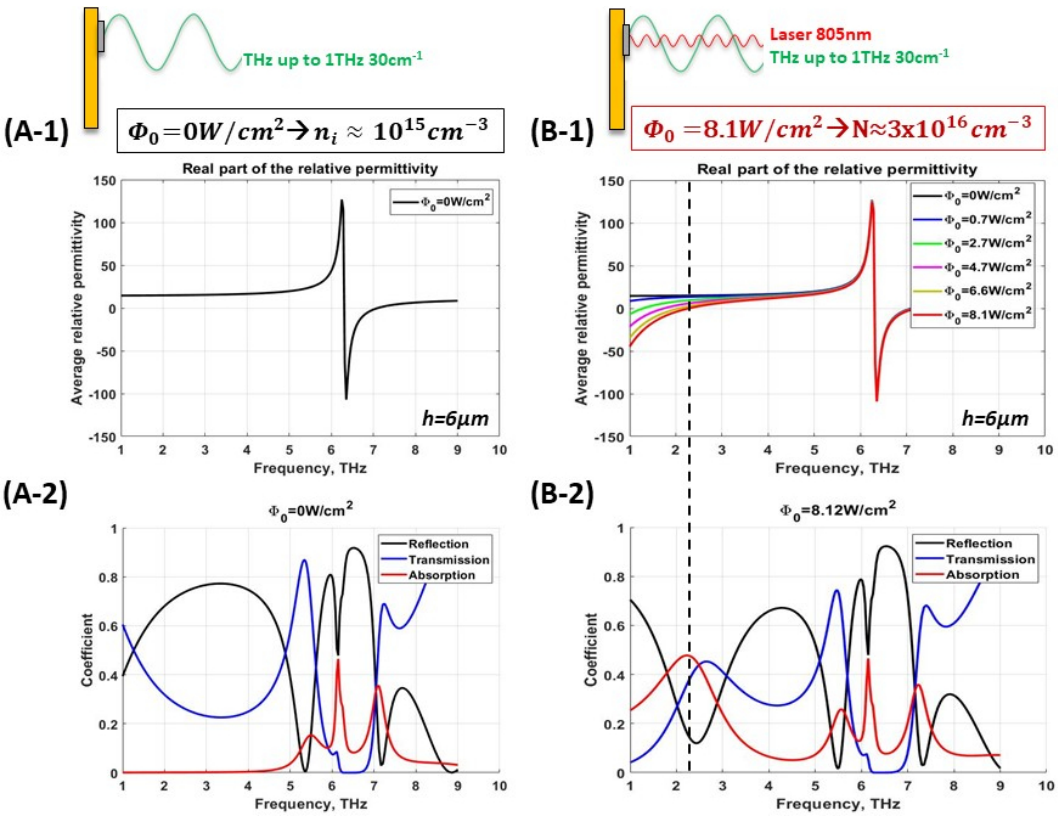

Figure 5.7 – *Theoretical results of the THz waves. (A-1) Real part of the relative permittivity distribution for an un-pumped InAs slab. (A-2) THz absorption, reflection and transmission spectra without laser irradiance. (B-1) Real part of the relative permittivity distribution at different laser irradiances in* W/cm^2*. (B-2) Real part of the relative permittivity distribution at different laser irradiances in* W/cm^2*.*

irradiance $\Phi_0 = 8.1W/cm^2$, the carrier density calculated attains a maximal value of $3 \times 10^{16}(cm^{-3})$. The average photo-generated permittivity is shown to vary from negative to positive values when the wavenumber increases (see figure5.7-B-1). This is due to the fact that when the pump is turned on, electromagnetic losses are introduced for the THz waves. This variety of structures engenders several absorption mechanisms for the active control of the THz waves. In figure5.7-B-2, we plot the THz absorption, reflection and transmission spectra to monitor the THz absorption that strongly depends on the polarization of the THz waves (as presented in Chapter 2). For the TE-polarization, a 50% absorption peak is reached around 2THz ($150\mu m$, $66.7cm^{-1}$). At this frequency, a Fabry-Perot resonance traps efficiently the THz wave within an epsilon-near-zero (ENZ) [85, 86] homogeneous slab which boosts the absorption, as is illustrated with a dashed-line between the figure5.7-B-1 and 2. This effect occurs for a frequency close to the average plasma frequency denoted $\bar{\omega_p}$ and defined by $\Re(\bar{\epsilon}(\bar{\omega_p})) = 0$. These results demonstrate that for a weak pump irradiance and according to the frequency, several types of HS can be optically induced in the InAs slab ranging from lossy dielectrics, ENZ layers to metallic layers. This THz transmission modulation result demonstrates that InAs is a suitable semiconductor

to realize active THz modulator that works at very low pump irradiances in the continuous-wave (CW) regime. A 50-fold decrease of the pumping irradiance is reached for a modulation of the THz transmission of about 60% (see figure5.6) when the InAs slab is pumped at $\Phi_0 = 8.1W/cm^2$ compared to photo-generated surfaces made of gallium arsenide (GaAs) which have been realized with pump irradiances attaining hundreds of kW/cm^2 [82] irradiances that are reached with pulsed lasers which are which are not compact and expensive.

In order to compare the THz transmission performance of each InAs membranes, we use a ratio of the THz transmission intensity because it is the easiest way to compare the experiment:

$$\frac{T_{\Phi_0}}{T_0} \tag{5.2}$$

where T_Φ is the laser-pump transmittance using different pump irradiances and T_0 is the reference measurement of the un-pumped transmittance ($\Phi_0 = 0W/cm^2$). The ration between the photo-driven transmittances (T_Φ/T_0) is a quantitative characteristic of the InAs membranes which allows us to determine their efficiency to modulate the transmission in the THz range.

Figure5.8 illustrates the ratio between the photo-driven transmittance (T_Φ) and the un-pumped transmittance (T_0). The map of the THz transmittance ratio is obtained for a broadband frequency range spanning from 1THz ($30cm^{-1}$) to 11THz ($380cm^{-1}$) and using different pump irradiances from $\Phi_0 = 0W/cm^2$ to $\Phi_0 = 8.1W/cm^2$. When the laser-pump is $\Phi_0 = 0W/cm^2$, a transmittance normalized to 1 is reached for all the analyzed spectra from 1 THz to 11 THz. For an increased laser-pump, the ratio between the photo-driven THz transmittance attains 95% at 1THz, as illustrated in figure5.6-(A-1) and figure5.6-(B-1). The ratio between the photo-driven transmittance also shows a 50% of modulation in the spectral range close to the Reststrahlen band. To verify this assertion, we plot the numerical simulations of the THz transmission spectra using different pump irradiances, as presented in figure5.6-(A-2) and figure5.6-(B-2). To correlate the experimental with the numerical simulations, we consider an effective carrier lifetime value equal to $\tau_{eff} = 6.5 \times 10^{-7}(s)$, where the effective diffusion length which becomes $L_{eff} = 39\mu m$ at $300K$. The comparison between the numerical simulation and the experimental ones shown good agreement in the displacement of the ratio between the photo-driven transmittance spectra when the InAs membrane is photo-excited with an uniform pump.

The surface quality of the InAs slab plays a major role when we compare the experimental results given by the ratio between the photo-driven transmittance ; (InAs epitaxial layer ($h = 5.9\mu m$ in fig.5.8-A-1 and $h = 6\mu m$ in fig.5.8-B-1) and InAs wafer $h = 8.3\mu m$ in fig.5.9-C-1). In the optical characterization of the InAs epitaxial layers we observe a THz modulation intensity with low scattering. However, in the spectral result of an InAs wafer slab (that has been subjected to a mechanical polishing) we observe a higher scattering influence [123] due to the roughness on the InAs surface.

Finally, we analyze the photo-generated carrier density (N), that is being creating in each of the photo-driven InAs membranes. Table5.3 presents the average value of the photo-carriers that are being photo-generated inside of the InAs slab. The numerical calculation of N has been performed by using our home-made multiphysics code. Thus, the photo-excited carrier density is located in an InAs slab with different

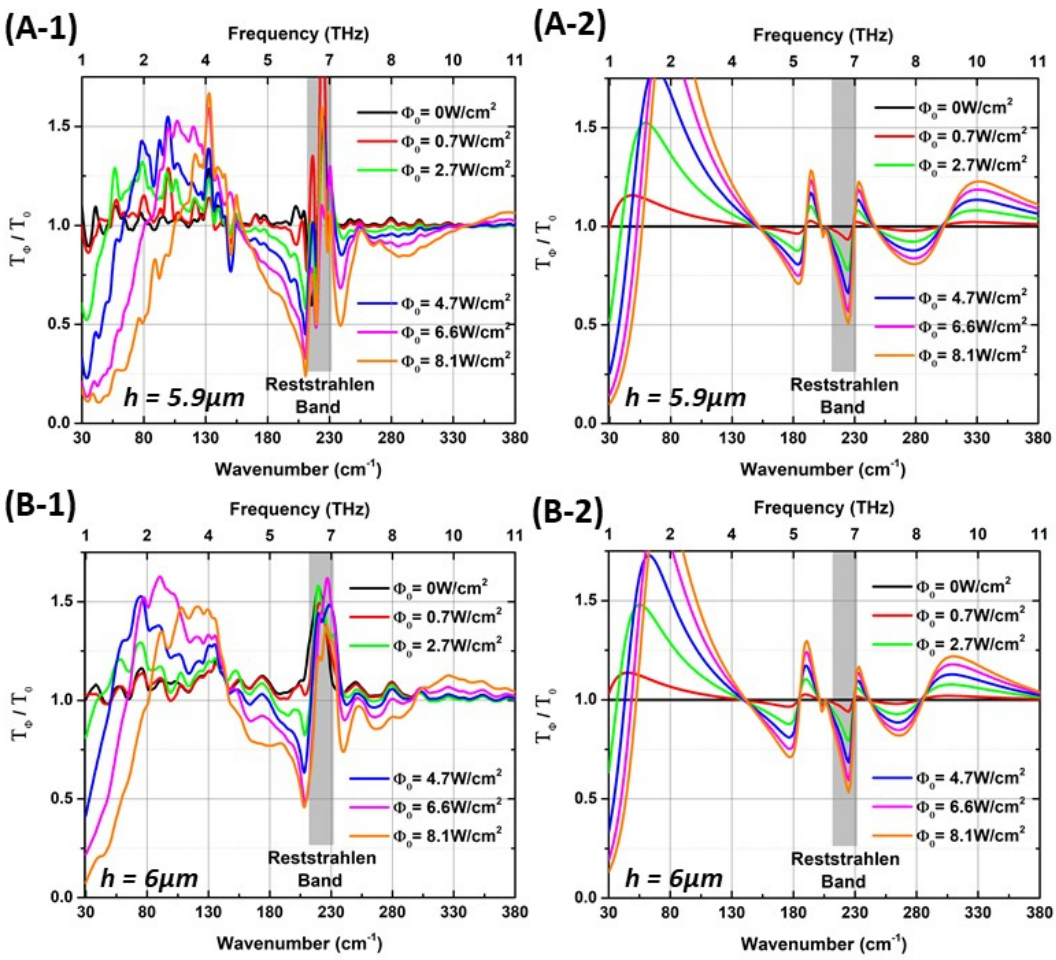

Figure 5.8 – *Experimental and numerical simulations results of the ratio between the photo-driven THz transmittance (T_Φ) and the un-pumped transmittance (T_0). (A) InAs epitaxial slab of thickness $h = 5.9\mu m$. (B) InAs epitaxial slab of thickness $h = 6\mu m$. The InAs are illuminated using different pump irradiances from $\Phi_0 = 0W/cm^2$ to $\Phi_0 = 8.1W/cm^2$. It is observed good agreement between the experimental and theoretical results.*

thicknesses is calculated according to the pump irradiance in W/cm^2. Finally, the obtained value has to be pondered with the effective recombination lifetime $\tau_{eff} = 6.5 \times 10^{-7}(s)$. The same procedure has been carried out for each InAs membrane of different thickness h ($5.9\mu m$ - $6\mu m$ - $8.3\mu m$).

The search of the estimation of the photo-generated carrier density is carried out to know the minimum N value to be able to begin to modulate the THz waves radiations. To modulate the THz wave radiations at 100% at 1THz($30cm^-1$), it is necessary to induce a photo-generated carrier density threshold (N_0). It must be higher than $N_0 = 10^{16}cm^{-3}$ according to the figure5.8 and the theoretical estimation of the photo-generated carrier density in Table5.3.

Different strategies can be considered to overcome this N_0 to begin to modulate the THz waves radiations, such as reducing the thickness of the InAs slab or increasing the τ_{eff} value or increasing the power of pump irradiances (in the case when larger

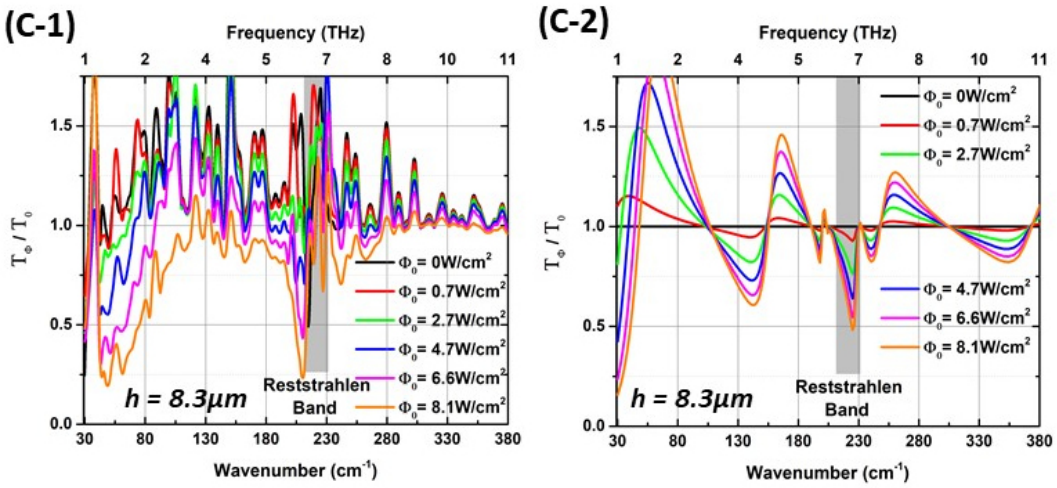

Figure 5.9 – *Experimental and numerical simulations results of the THz transmission modulation using an InAs wafer of $h = 8.3\mu m$ thickness which is irradiated using different pump irradiances from $\Phi_0 = 0W/cm^2$ to $\Phi_0 = 8.1W/cm^2$.*

$h(\mu m)$	$\Phi_0(W/cm^2) \rightarrow$	0.7	2.7	4.7	6.6	8.1
5.9	$N(cm^{-3}) \rightarrow$	3x10^{15}	1.2x10^{16}	2.1x10^{16}	3x10^{16}	3.7x10^{16}
6	$N(cm^{-3}) \rightarrow$	2.8x10^{15}	1.1x10^{16}	1.9x10^{16}	2.7x10^{16}	3.4x10^{16}
8.3	$N(cm^{-3}) \rightarrow$	2x10^{15}	8.5x10^{15}	1.4x10^{16}	2x10^{16}	2.5x10^{16}

Table 5.3 – *Photo-generated carrier density (N) in cm^{-3} estimation for the three InAs membranes at different pump irradiances from $\Phi_0 = 0W/cm^2$ to $\Phi_0 = 8.1W/cm^2$.*

thicknesses are considered), as presented previously. In fact, this is the reason why we have considered membranes with very small thickness between (10 to $1\mu m$), to overcome this N_0 to modulate THz waves radiations on a broadband frequency range.

5.1.4 Conclusion

In this section, experimental data obtained using the FTIR measurements and numerical simulations results for the optically characterized InAs membranes were presented. These experimentally and theoretically results shows the great potential of the InAs material to control THz electromagnetic radiation at room-temperature ($300K$) by using photo-generated carriers in InAs slab at very low-pump irradiances. The ration between the photo-driven transmittance demonstrates that the InAs is a suitable semiconductor to realize active THz modulator that works at very low pump irradiances in the continuous-wave (CW) regime at room-temperature. According to the state of the art, these results demonstrate a 50-fold decrease of the pumping irradiance is reached for a THz transmission modulation of 70% when the InAs slab is pumped at $\Phi_0 = 8.1W/cm^2$.

5.2 Photo-driven THz modulator

Recent developments of bright terahertz (THz) sources and efficient detectors accelerate the progress of non-destructive THz systems [124, 125]. However, the demand for versatile THz components able to address a wide range of frequencies is high [126, 127, 2, 4]. Among the envisaged approaches, artificial structures named metasurfaces based on subwavelength electromagnetic resonators were used to control THz waves [54]. Real-time and dynamical control have been demonstrated with photo-generated metasurfaces [59, 60, 61]. However, several issues must be bypassed in terms of modulation rate or pump irradiance before this approach might be implemented in the application domain.

In this section, we theoretically and experimentally study the THz electromagnetic properties of an undoped-InAs slab whose permittivity is optically modified by a photo-generation process. The modulation of the permittivity is calculated by solving the ambipolar rate equation for the free carriers. We have demonstrated that InAs is a promising semiconductor to manufacture fast and efficiently on-chip THz components [75, 76]. We show a high modulation of the THz transmission up to 100% from 0.75THz to 1.1THz at very low irradiance in the continuous wave (CW) regime. We also have demonstrated a high-speed transmission modulation rate up to the MHz range with a modulated pump.

This section starts with the presentation of the optical characterization set-up which is mainly composed of a frequency-multiplied chain driven by a synthesizer used as a source and a heterodyne-detection as a receiver. This set-up allows us to analyze the spectral range from 0.75 THz to 1.1THz. Based on numerical simulations, we will show the comparison between experimental and theoretical results at different pump irradiances in an InAs slab. In the following section, the experimental and numerical simulations results concerning the optical characterizations are presented.

5.2.1 Optical characterization set-up

We have demonstrated that photo-generated carrier into an InAs slab can modulate efficiently the transmitted light until the THz (1THz). However, because we are at the limit of detection of the FTIR set-up, we perform experiments with an experimental set-up adapted in the spectral range from 0.75 THz to 1.1THz. This set-up is used to evaluate the transmission of the THz-wave through a micrometric-thick slab of undoped-InAs using a continuous-wave and modulated by a laser of $805nm$ wavelength. All these THz experiments have been performed in the $T\acute{e}Ho$ group at IES with Drs. S. Blin and P. Nouvel.

The schematic of the experimental set-up is presented in figure5.10. In the THz characterization set-up, the focused THz wave passes through the InAs membrane located in the same sample holder hole which in turns is illuminated by a collimated laser pump. A second hole is used as a reference calibration. The whole is mounted on a X and Y translation stage presented in figure5.11-A. The maximum laser power is $500mW$ and the spot diameter is $3mm$ when it is collimated. The rest of the optic set-up is composed of two THz wave systems: source and receiver, as shown in figure5.11-C. The THz source system is composed of a synthesizer which is used as a source, then its signal is multiplied in frequency by diodes and other amplifiers by a factor (x81). The THz receiver system is composed of an electric spectrum analyzer

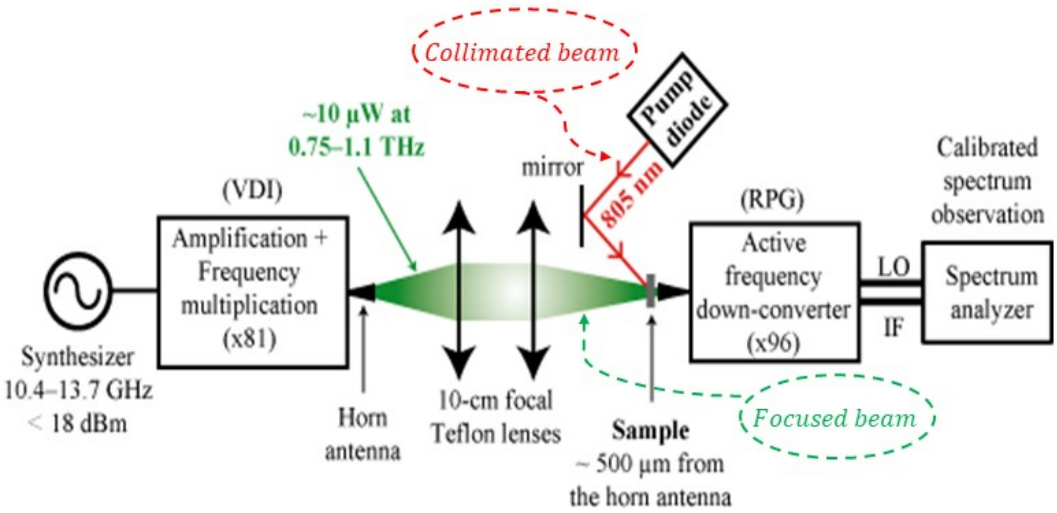

Figure 5.10 – *Schematic of the implemented optic set-up provided by the TéHo-group. It is composed of a THz generation source and a receiver system to optically characterize in transmission the InAs membrane which is irradiated by a laser pump at room-temperature.*

that sends its local oscillator (LO) on the head of an heterodyne detection located just after the InAs sample (see figure5.11-B), which is multiplied in frequency (x96) by diodes and other amplifiers in order to reach in the range 0.75THz to 1.1THz (RF signal). This signal is mixed with the signal measured on a diode which returns the frequency difference (IF frequency), that goes into the bandwidth of the electric spectrum analyzer, which displays this measurement. The measurement is calibrated in terms of system losses and frequency (factor x96). An overview of the experimental set-up is shown in figure5.11-D.

5.2.2 Static photo-driven THz modulator

We have carried out the experiments described in figure5.12 where the InAs membrane is photo-excited using a CW pump of wavelength equal to $\lambda = 805nm$. The maximum power that can illuminate the InAs sample is equal to $500mW$ and the laser-spot diameter is $\phi = 3mm$ when it is well collimated. The rest of the optic set-up corresponding to the THz generation source and the heterodyne-detection is used as previously presented. Then, the InAs membrane is photo-excited at different pump fluences with an irradiance of few W/cm^2.

Figure5.12 illustrates the THz characterization of the undoped-InAs epitaxial layer of thickness h=5.9μm, which corresponds to the static photo-driven THz modulator. Figure5.13-A illustrates the transmitted power (in dBm) for a frequency ranging from 0.75THz to 1.1THz with different pump irradiances. The spectrum shows that low-pump irradiance in the continuous regime of only few of W/cm^2 is sufficient to modulate the transmission of the THz waves up to $\approx$ 20dB. Figure5.13-B presents the normalized THz transmission, where the spectrum shows that low irradiance ($\Phi_0 = 6.6W/cm^2$) in the CW pump is enough to modulate the transmission of the THz waves from 60% to 0% on a broad band frequency range. It confirms the

Figure 5.11 – *Home-built optical set-up of the InAs membranes located at the TéHo-group. (A) InAs membrane positions. (B) Head of a heterodyne detection - Receiver system. (C) Caption of the entire optical THz and IR beam path. (D) Entire optic set-up with the synthesizer and the electrical spectrum analyzer.*

results obtained in previous experiments performed with the FTIR. To normalize THz transmission, we normalized the THz spectra according to the transmitted power through the sample holder without InAs slab, the resulting unit is dB. Then, we just change the unit from dB to linear transmission (no unit as it is a ratio of power). At last, figure5.13-C illustrates the ration between the THz transmittance T_{Φ_0}/T_0 in dB. It consists of the transmission ratio intensity between the InAs slab at different pump fluences T_{Φ_0} and the reference measurement T_0 (when the laser pump is turned-off $\Phi_0 = 0W/cm^2$). We show how the THz transmission is modulated when the InAs material is illuminated with different laser pump fluences. We observed that an irradiance of only $\Phi_0 = 2.7W/cm^2$ on the static photo-driven device allows a modulation of the transmitted waves up to 6dB (blue color), and with an irradiance of $\Phi_0 = 4.7W/cm^2$ is modulated up to 15dB (red-color). Higher pumps overcome 20dB. The highest THz transmittance modulation obtained is around 30dB with a very low-pump equal to $\Phi_0 = 8.1W/cm^2$. This is enough to modulate the transmission of the THz waves up to 100% at a frequency ranging from 0.75THz to 1.1THz.

Figure5.14 illustrates the same THz characterization but in a polished InAs wafer of thickness $h = 8.3\mu m$. Figure5.14-A illustrates the transmitted power (in dBm) for a frequency ranging from 0.75THz to 1.1THz with different pump irradiances. The spectrum shows that the maximum depth transmission modulation of the THz

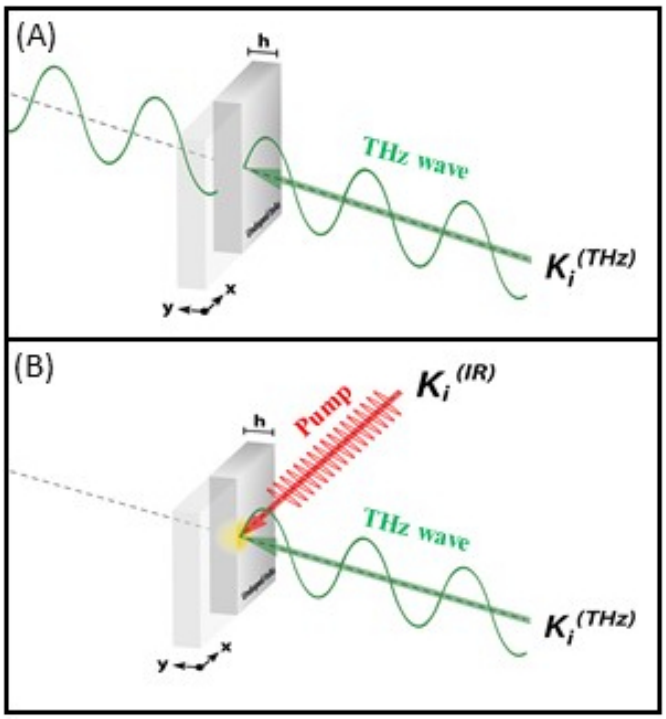

Figure 5.12 – *Schematic of the static photo-driven THz modulator, based on InAs membrane of thickness "h" which is illuminated by a focused THz light beam (green-color) emitted from the THz generation source (synthesizer). The InAs slab is illuminated by a laser pump (red-color). Then, the signal transmitted through the InAs slab is collected by the head of a heterodyne detection that sends its LO signal to an electric spectrum analyzer which displays this measurements.*

waves is $\approx$ 10dB which is 10-times lower than the modulation obtained previously. It can be explained by the fact that the InAs thickness is thicker than the previous one, therefore, the InAs sample demands more pump irradiance to be able to photo-generate an enough carrier density to control the THz waves. This assumption can be observed in figure5.14-B where the normalized THz transmission spectrum shows that the static photo-driven transmission is less modulated up to 95%. This can also be verified in figure5.14-C which illustrates that the highest transmission modulation is around 19dB at an irradiance of $\Phi_0 = 8.1W/cm^2$.

The comparison between numerical simulations presented in figure5.15 and the experimental ones presented in Fig.5.13-B and in Fig.5.14-B shows a good agreement in the normalized THz spectra results when the InAs slabs of thicknesses h=5.9μm and h=8.3μm are illuminated by a THz plane wave in normal incidence. In the numerical result, the parameter that we use to fit the values between the experimental values and the numerical simulations was the carrier lifetime recombination. The illustration of the photo-carriers distribution is complex to calculate since τ_{eff} gives a non-linear behavior by using different pump irradiances. Under this assumption, a rough description is presented for the THz spectra results. In the theoretical calculation, we consider a $\tau_{eff} = 6.5 \times 10^{-7}(s)$, which corresponds to the time obtained in the experimental determination of $L_{eff} \approx 40\mu m$. Under this conditions,

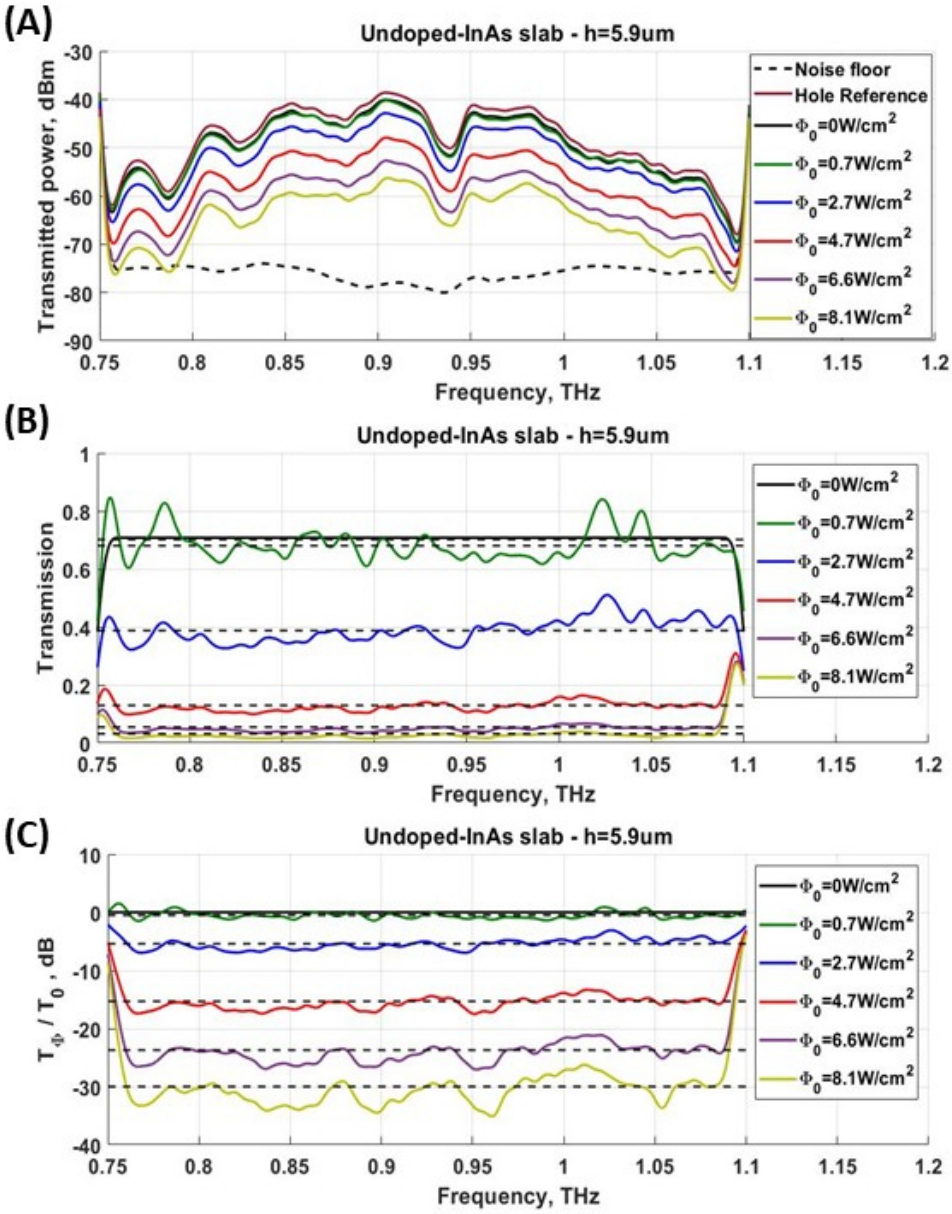

Figure 5.13 – *Transmission spectra in the THz range from 0.75THz to 1.1THz of an intrinsic InAs epitaxial layer of thickness h=5.9μm illuminated by a laser of different irradiances. (A) THz transmitted power in dBm. (B) Normalized THz transmission. (C) THz transmission ratio intensity T_{Φ_0}/T_0 in dB.*

the maps of the THz transmission coefficient calculated under different pump fluences, presented in figure5.16-B illustrates that for an irradiance over $\Phi_0 = 6.6W/cm^2$, a 60% of attenuation of the THz transmission is reached showing good agreement with the experimental result in figure5.13-B. The THz transmission attenuation can be explained by using the THz absorption coefficient presented in figure5.16-A. The map of the THz absorption shows that a 50% is reached for the homogeneous structure (HS) for a broadband frequency range spanning from 0.75THz to 1.1THz. Furthermore, we

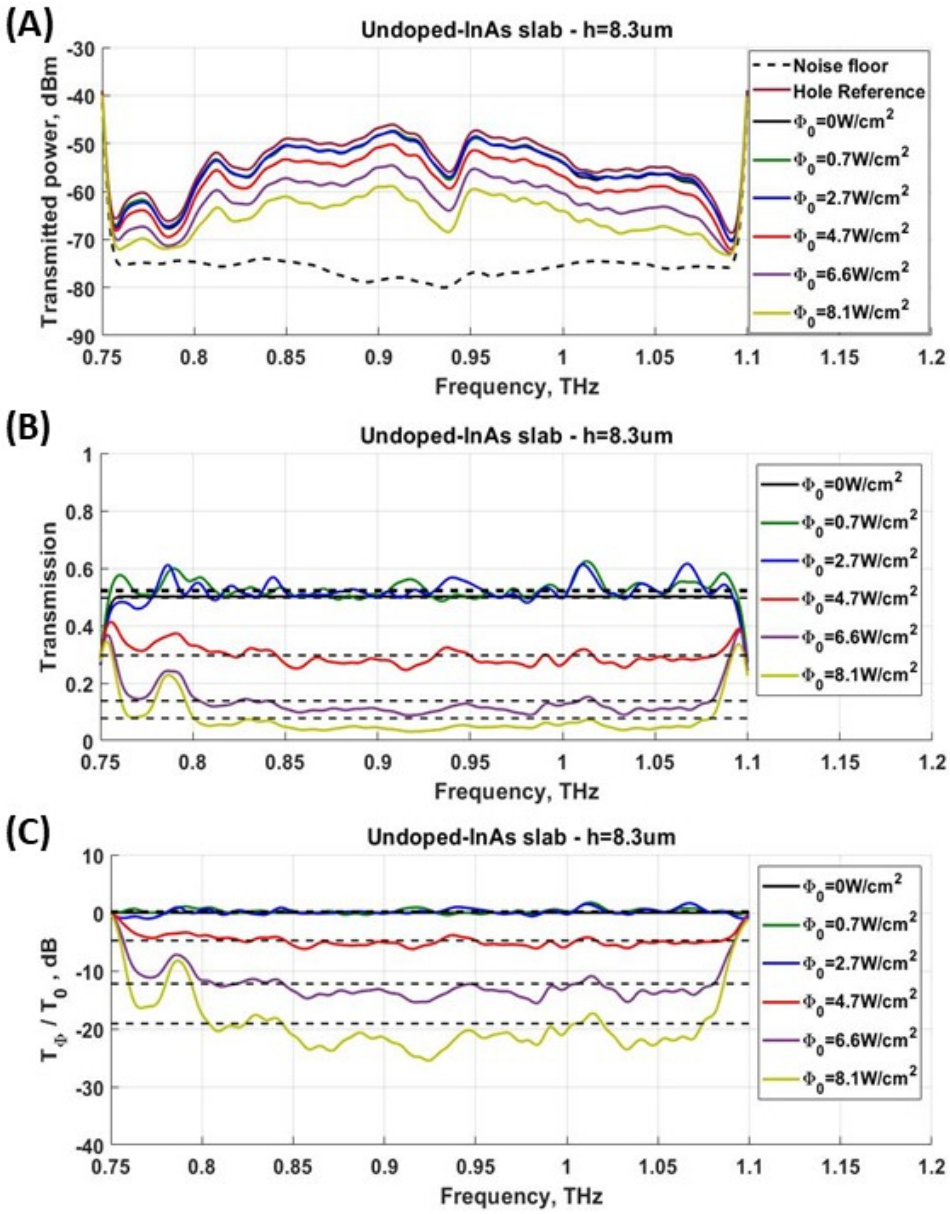

Figure 5.14 – *Transmission spectra in the THz range from 0.75THz to 1.1THz of an intrinsic InAs wafer slab of thickness h=8.3μm illuminated by a laser of different irradiances. (A) THz transmitted power in dBm. (B) Normalized THz transmission. (C) THz transmission ratio intensity* T_{Φ_0}/T_0 *in dB.*

can observe an optimum in the THz absorption when the pump irradiation increases. This transition arises for a pump irradiance around $\Phi_0 = 3.5W/cm^2$ where the real part of the average permittivity is near-zero: $\Re(\bar{\epsilon}) = 0$. Therefore, there is not need to illuminate the InAs sample with a higher pump irradiance (for example, when the pump irradiance is higher than $\Phi_0 = 3.5W/cm^2$ the absorption decreases). This THz absorption result demonstrates that thin InAs slab $h = 5.9\mu m$ behaves such as metallic material at a low pump fluence. An increase of the pump irradiance results

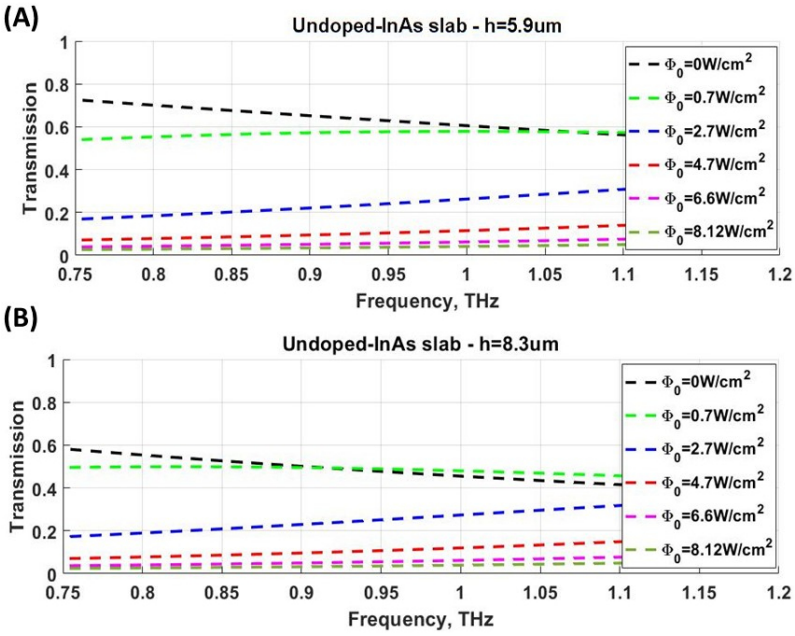

Figure 5.15 – *Theoretical result of the normalized transmission spectra in the THz range from 0.75THz to 1.1THz of an intrinsic InAs slab illuminated by a laser of different irradiances. (A) InAs slab of thickness h=5.9μm. (B) InAs slab of thickness h=8.3μm.*

in conceiving a metallic layer of very high permittivity (negative real and imaginary parts). In that case, figure5.16-C shows that the THz waves are strongly reflected by increasing the injection of pump irradiance which decreases its absorption in the InAs slab.

5.2.2.1 Confirmation of the THz waves modulation

This section deals with the confirmation of the THz waves modulation for specifics THz frequencies performing the comparison between the numerical simulations and experimental results. We also study the THz modulations according to the thickness of the InAs membrane in order to find out the thickness influence with our numerical simulations.

Figure5.17 illustrates the results of the static photo-driven THz modulator. We set a specific THz frequency ($F_c = 0.925THz$) and the InAs sample of thickness $h = 5.9\mu m$ is illuminated under different pump irradiances. Fig.5.17-A illustrates the transmitted power (in dBm) for a specific frequency with different pump irradiances. The figure shows that low-irradiances in the continuous regime of only a few W/cm^2 is enough to modulate the transmission of the THz waves up to 20dB. Fig.5.17-B presents the normalized THz transmission, where the spectrum shows that low-irradiance ($\Phi_0 = 6.6W/cm^2$) in the CW pump is enough to modulate the transmission of the THz waves from 70% to 0% on a broadband frequency range. This results validate the results presented in figure5.13-B where a pump around $\Phi_0 = 2.7W/cm^2$ is the minimum pump irradiance to start the modulation of the THz transmission radiation.

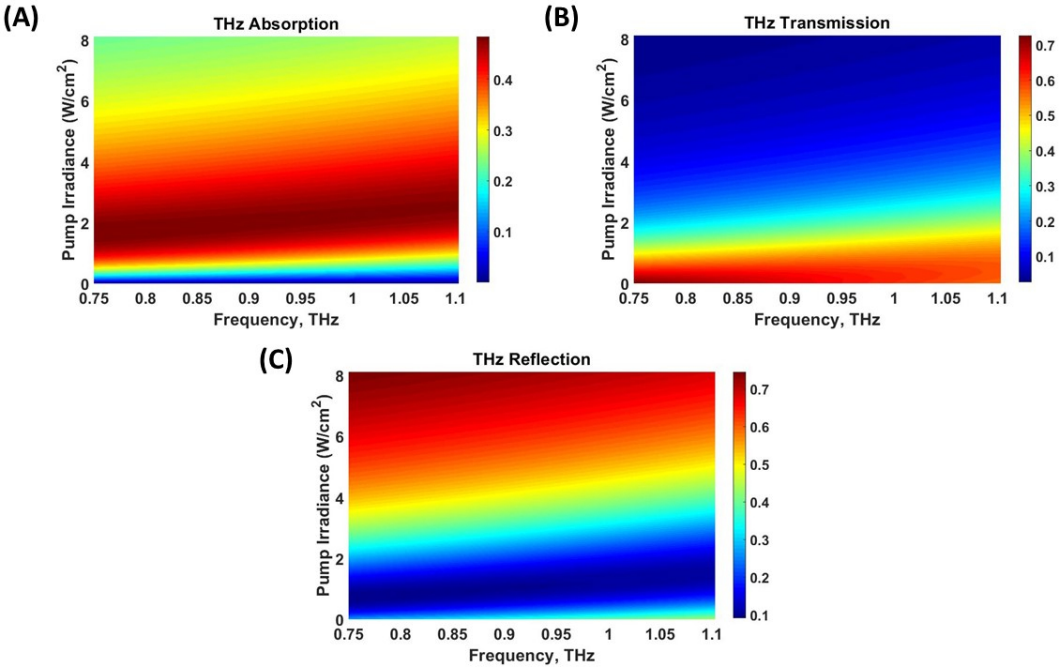

Figure 5.16 – *Theoretical results of an undoped-InAs slab of thickness $h = 5.9\mu m$ illuminated with a THz plane wave at a frequency ranging from 0.75THz to 1.1THz. (A) THz absorption. (B) THz transmission. (C) THz reflection.*

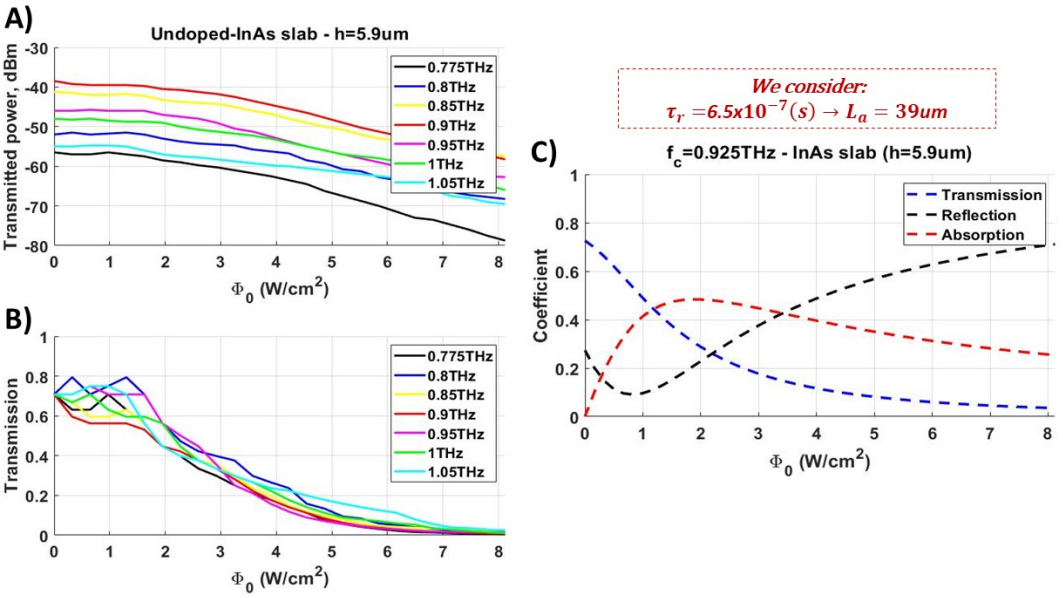

Figure 5.17 – *Confirmation of the static photo-driven THz modulator device induced by low-pump irradiances. (A) Experimental THz transmission in dBm when the pump irradiance increases. (B) Normalized THz transmission of the experimental data. (C) Theoretical THz transmission, reflection and absorption calculated at 0.925THz and for a constant carrier lifetime value $\tau_{eff} = 6.5 \times 10^{-7}(s)$.*

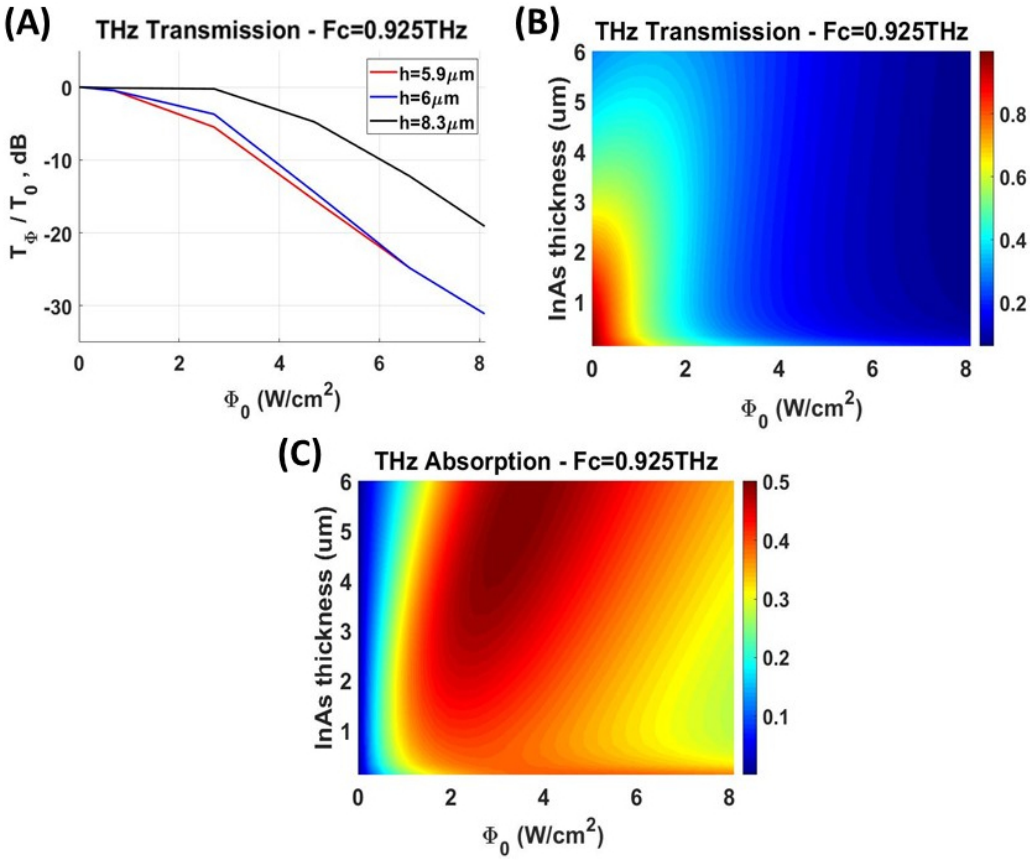

Figure 5.18 – *Comparison between the three fabricated static photo-driven THz modulators devices, based on InAs membranes of thickness $h = 5.9\mu m$ - $h = 6\mu m$ - $h = 8.3\mu m$ when the pump irradiance increases. (A) Theoretical (dashed-lines) and experimental (full-lines) results of THz transmission in dB obtained at 0.925THz. (B) Theoretical THz transmission calculated at 0.925THz when the InAs thickness increases. (C) Theoretical THz absorption calculated at 0.925THz when the InAs thickness increases.*

We also performed the simulation of the experimental data presented in Fig.5.17-B to be able to compare with the numerical simulations presented in figure5.17-C. The comparison shows a good agreement in the THz transmission distribution when the pump irradiance increases. In the theoretical result, the illustration of the THz transmission is complex to calculate since τ_{eff} gives a non-linear behavior when the pump irradiances increases. Under this assumption, a rough description is presented for the THz absorption, reflection and transmission distribution presented in Fig.5.17-C where is considered a constant $\tau_{eff} = 6.5 \times 10^{-7}(s)$. The best THz transmission comparison between numerical simulation and the experimental result is reached at high-pump irradiance since the THz transmission attenuation attains a maximal value due to the larger life-time $\tau_{eff} = 6.5 \times 10^{-7}(s)$, it means that the ambipolar diffusion length is $L_{eff} = 39\mu m$. These results shows a limitation of the home-made multiphysics code since τ_{eff} varies with the pump irradiance. It must be solved and it will be proposed as a future perspective in the short term. On the

meantime, this results give us information about the possible behavior of the THz absorption and THz reflection.

Fig.5.18-A illustrates the comparison between the numerical (dashed-lines) and the experimental (full-lines) results of the THz transmitted power in dB to understand the thickness influence with the THz modulation when the pump irradiance increases. The study was performed in the three different static photo-driven THz modulators of thickness: $h = 5.9\mu m$ - $h = 6\mu m$ - $h = 8.3\mu m$. The three photo-driven THz modulator overcome 20dB of THz transmission modulation. We can observe that the highest THz transmission modulation in the experimental results is 30dB at an irradiance of $\Phi_0 = 8.1W/cm^2$. The difference of the modulation depth between experiment and theoretical result is related to the non-linear behavior when the pump increases, nevertheless, the comparison shows a good agreement in the THz transmission distribution. Figure5.18-B shows the numerical simulation of the THz transmission spectra for a specific frequency 0.925THz. This normalized THz transmission map shows that the variation of the transmission is in agreement with the previously presented experimental results, e.g. the THz transmission attains minimal values when high irradiances are used. It can be explained using the Fig.5.18-C. This THz absorption map shows that the THz waves using a pump irradiance higher than $\Phi_0 = 6.6W/cm^2$ are strongly reflected by increasing the injection of pump fluence which decreases its absorption coefficient in the InAs slab.

5.2.3 Dynamic photo-driven THz modulator

We have also performed experiments using a modulated pump described in figure5.19. In this case, to perform the amplitude modulation of the laser pump, we use an acousto-optic modulator (AOM). The rest of the optic set-up is the same as the previous one composed of two THz wave systems: source and receiver. The THz source is obtained by a frequency-multiplied signal driven by a synthesizer. The THz detection is composed of an external heterodyne head at spectrum analyzer. The laser pump is composed of a $805nm$ laser with amplitude-modulation using an acousto-optic modulator, as illustrated in figure5.20.

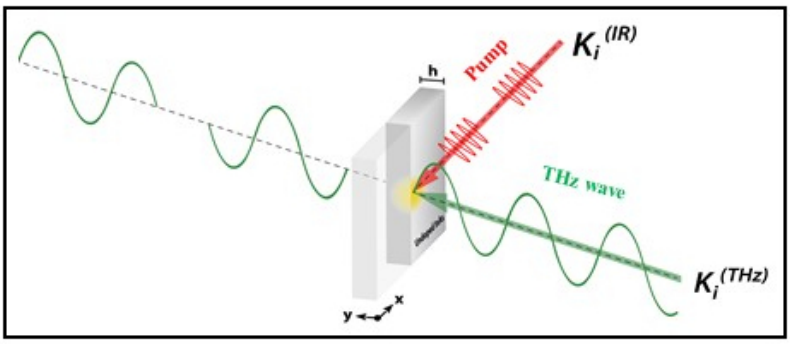

Figure 5.19 – *Schematic of the dynamic photo-driven THz modulator, based on InAs membrane of thickness "h" which is illuminated by a focused THz light beam (green-color) emitted from the THz generation source (synthesizer). The InAs slab is illuminated by using a modulated pump (red-color). Then, the signal transmitted through the InAs slab is collected by a heterodyne-detection system.*

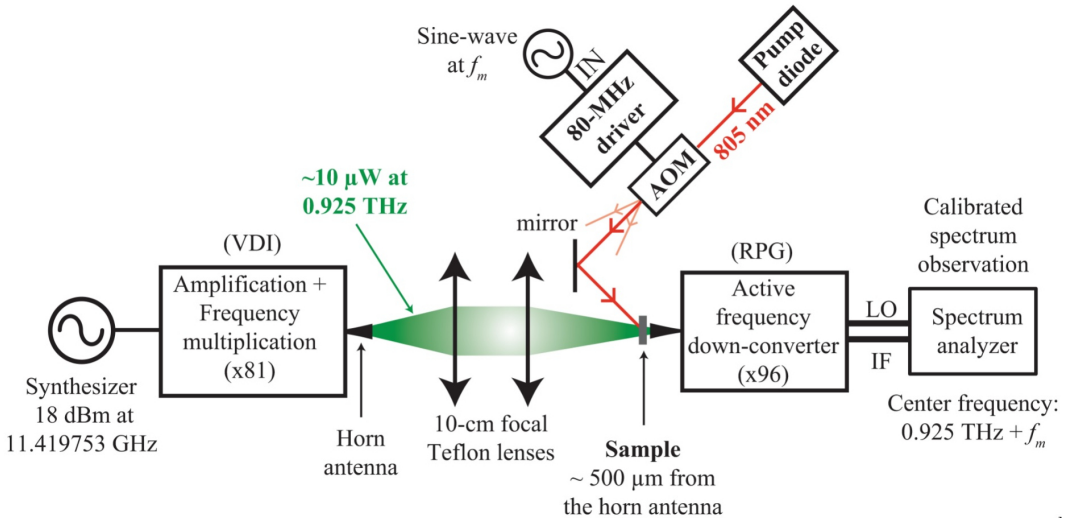

Figure 5.20 – *Schematic of the implemented optic set-up using a modulated pump using an acousto-optic modulator. It is composed of a THz source, a THz modulator, a THz detection and a laser pump to obtain the THz characterization in transmission of the InAs membrane which is irradiated by a modulated pump at room-temperature.*

To demonstrate experimentally the theoretical limits up to the MHz, we use an acousto optic modulator, as presented in Fig.5.21 located at the top right of the caption. The pump beam enters into the AOM with a certain angle of incidence that allows the wave to be reflected in the cavity. An acoustic wave signal propagates through the crystal where a stationary wave sets locally modifying the refractive index (n). As the acoustic waves propagates within the crystal, the optical index is modulated proportionally to this pressure wave. The wave being monochromatic, it leads to a sinusoidal optical index distribution that will act as a diffraction grating for the incoming light. Therefore, the incident optical wave diffracts on the grating, with a zero-order, and higher orders that are more dispersed. If we turn off the acoustic wave, we have not grating, not diffraction, so the light goes through the crystal without any other effect than standard reflection and refraction.

To perform the experiments using a modulated pump, the THz frequency was set to $f_c = 925GHz$. We use the amplitude modulation at frequency f_m with a depth of modulation m where the resulting spectrum presents: a carrier component at f_c and modulation satellites at $f_c \pm f_m$. We measure the amplitude of the modulation satellite for increasing f_m, as illustrated in figure5.22.

The modulation depth using the AOM has been evaluated using static measurements. Figure5.23-A shows the THz transmission power in dBm which is modulated with an AOM at carrier frequency $f_c = 0.925THz$. The pump induces a THz transmission power modulation of $2dB$. To verify this assertion, we plot in figure5.23-B, the THz transmission power in dBm at two different carrier frequency $f_c = 0.9THz$ (red color) and $f_c = 0.95THz$ (pink color) using different pump irradiances. The map of the THz transmission power confirms that the depth modulation of $2dB$ is reached for a pump irradiance around $\Phi_0 = 2.7W/cm^2$.

The modulation depth using the AOM has been evaluated using dynamic measurements. In figure5.24, the THz frequency was set to $f_c = 0.925THz$, we set a pump

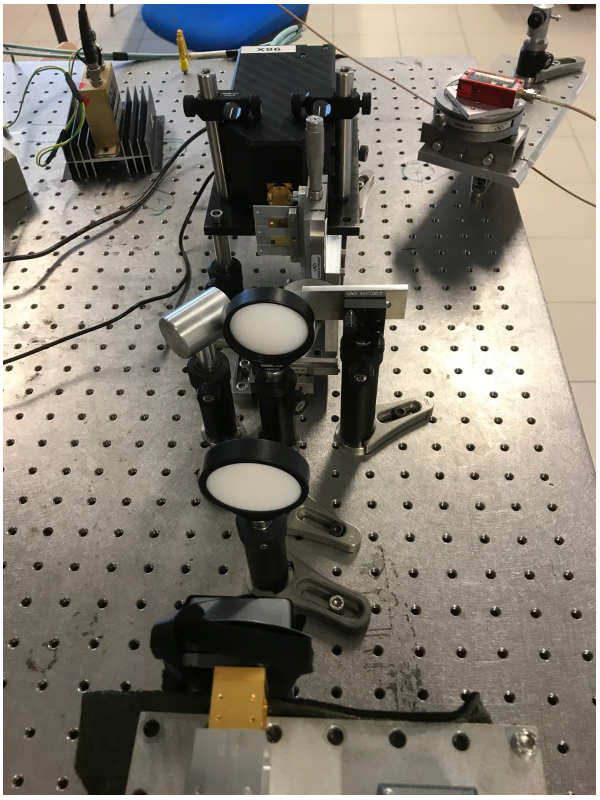

Figure 5.21 – *Home-built optical set-up using a modulated pump using an acousto-optic modulator, located at the top right of the caption.*

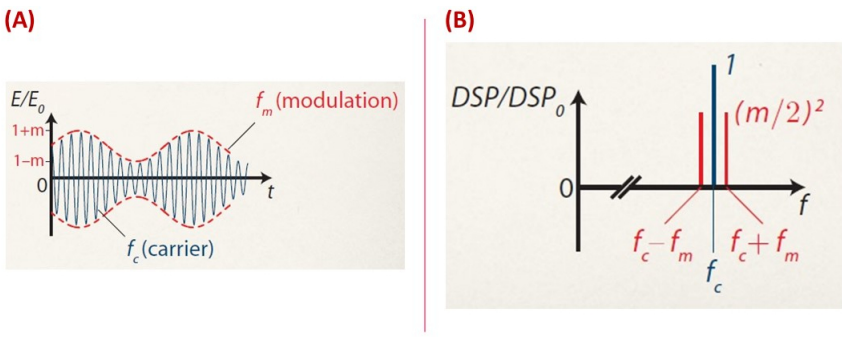

Figure 5.22 – *Basic signal processing, (A) The THz carrier signal (f_c) using an amplitude modulation at frequency f_m with a depth of modulation. (B) Resulting spectrum where a carrier component at f_c is modulated at $f_c \pm f_m$.*

irradiance of $\Phi_0 = 8.1W/cm^2$ at the laser output. These results was obtained using a square-shape modulation of the acousto-optic signal to photo-generate the InAs slab, and that it was measured using a zero-order mode at the spectrum analyser. Fig.5.24 presents the transmitted power as a function of time, showing the dynamic response of the THz modulation at $0.925THz$. This is a pedagogic way to show the THz transmission modulation for a square modulation.

Figure5.25 illustrates the THz spectrum with and without pump modulation.

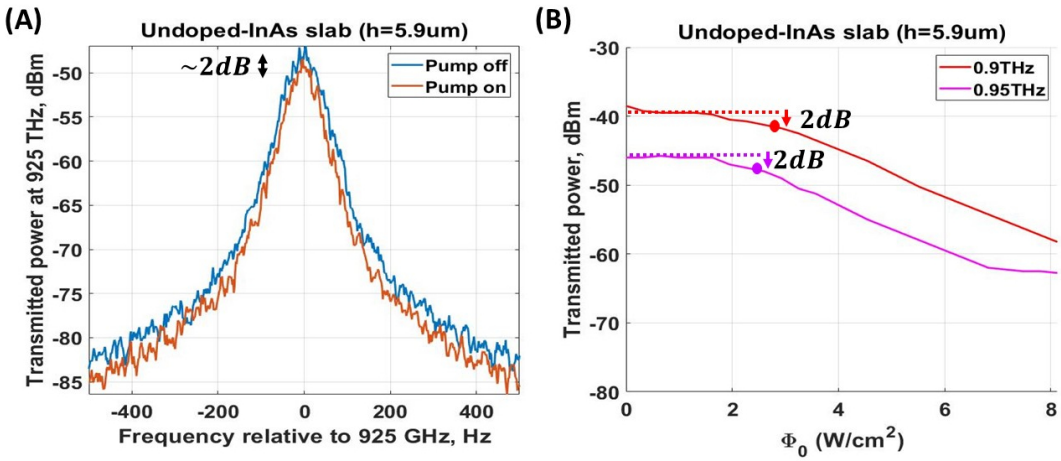

Figure 5.23 – *Modulation depth using the AOM evaluated using static measurements. (A) A 2dB THz transmission modulation is reached at carrier frequency* $f_c = 0.925THz$. *(B) THz transmission power at two different carrier frequency* $f_c = 0.9THz$ *(red color) and* $f_c = 0.95THz$ *(pink color) using different pump irradiances confirms that the depth modulation of* $2dB$ *is induced when the pump irradiance is* $\Phi_0 = 2.7W/cm^2$. *When the pump irradiance is increased, the THz transmission power modulation attains a maximal value around* $20dB$

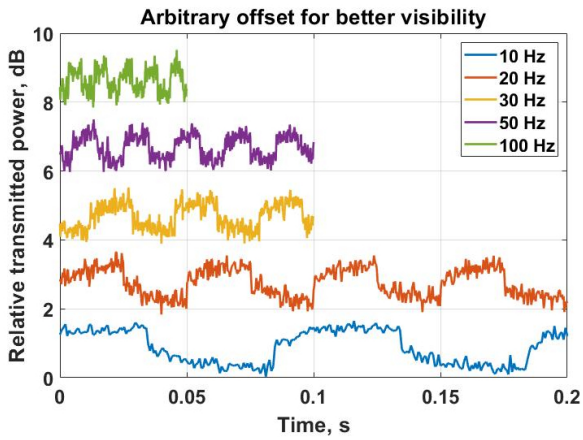

Figure 5.24 – *THz Transmitted power observed at the spectrum analyzer in a zero-span mode for a pump irradiance modulated using an on/off amplitude modulation at increasing frequencies.*

Fig.5.25-A shows the modulation satellites as expected (satellite and background power are measured for each modulation frequency). Fig.5.25-B presents the THz transmitted power modulation at 1MHz. To verify this last result, we plot the Bode-like transfer function for the undoped InAs of thickness $h = 5.9\mu m$. In this case, the THz frequency was set to 925GHz, we set a pump irradiance of $\Phi_0 = 8.1W/cm^2$ and the zero-order of the AOM diffraction output is used to photo-generate the InAs slab. Fig.5.26-A presents the maximum hold values of a fine analysis of 12000 spectra acquired to evaluate the modulation bandwidth of the InAs sample. The

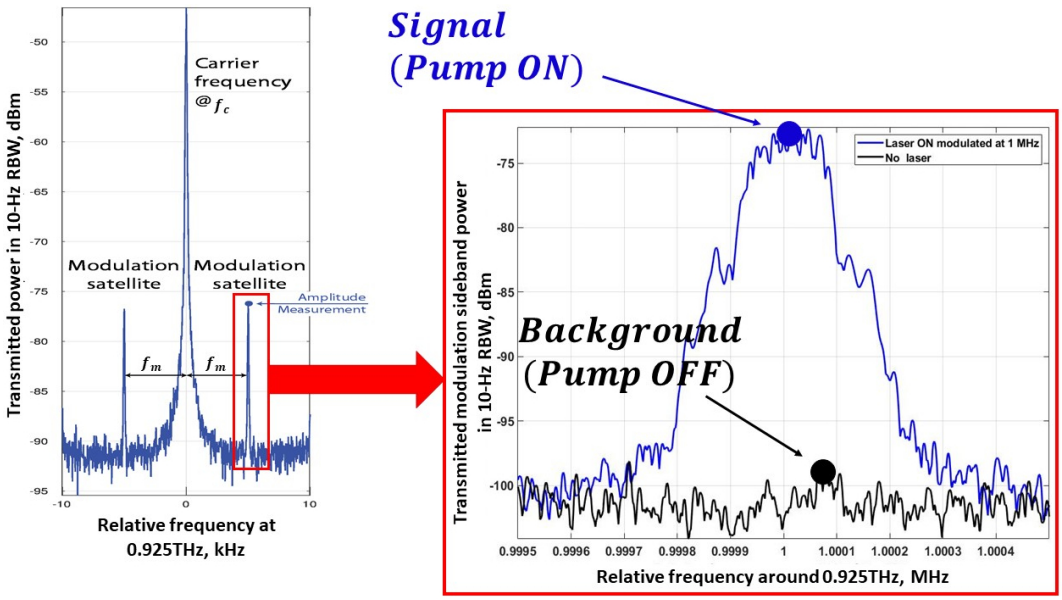

Figure 5.25 – *(A) THz frequency set at $f_c = 0.925THz$ and the THz transmitted power is modulated with a laser at $f_m = 5kHz$ in hold-on mode for the left and right modulation satellites. (B) THz transmitted power modulation with and without laser at 1MHz in hold-on mode for the right modulation satellite.*

sideband amplitude (blue dots) is measured at $f_c = 0.925THz + f_m$ for an increasing modulation frequency f_m of the laser-pump using the AOM. The observed cut-off frequency of the InAs slab $h = 5.9\mu m$ is in the MHz range. Figure5.26-B shows the peak-to-peak amplitudes (red dots) of the optical power measured by the photodiode (PDA10A-EC, Si Amplified Detector, 200-110nm provided by THORLABS) for an increasing modulation frequency of the laser-pump using the AOM. The idea is to evaluate the modulation bandwidth of the AOM. This result demonstrates that the cut-off frequency that we observe is due to the AOM and not the InAs sample.

Knowing that the cut-off frequency that we observe is due to the AOM and not to the InAs sample, we perform an attempt to extract the transfer function. Figure5.27-A shows the THz and Pump relative transmission that we use to find the InAs sample function transfer that is presented in figure5.27-B, demonstrating a cut-off frequency up to 2MHz.

The comparison between the experimental results and the theoretical assumptions shows a good agreement in the value of the high-speed modulation rate for the THz waves. A modulation rate up to 2MHz was theoretically expected. Since that, the InAs slab of thickness $h = 5.9\mu m$ has been illuminated with $\Phi_0 = 2.7W/cm^2$, this irradiance induces a photo-generated carrier density $N \approx 1.2 \times 10^{16}(cm^{-3})$ (see Table5.3), which controls the ambipolar recombination lifetime, and in this case is $\tau_{eff} = 5 \times 10^{-7}(s)$. It means that, the experimentally demonstrated high-speed modulation rate of $2MHz$ for the THz waves has been theoretically expected owing the value of the InAs recombination lifetime $1/\tau_{eff}$ $(2MHz)$. This fact suggest a dynamic response for the high-speed modulation rate which is driven by the injection level $N(\tau_{eff})$ and attains a maximal theoretical value of 0.5GHz for a $N \approx 10^{18}(cm^{-3})$

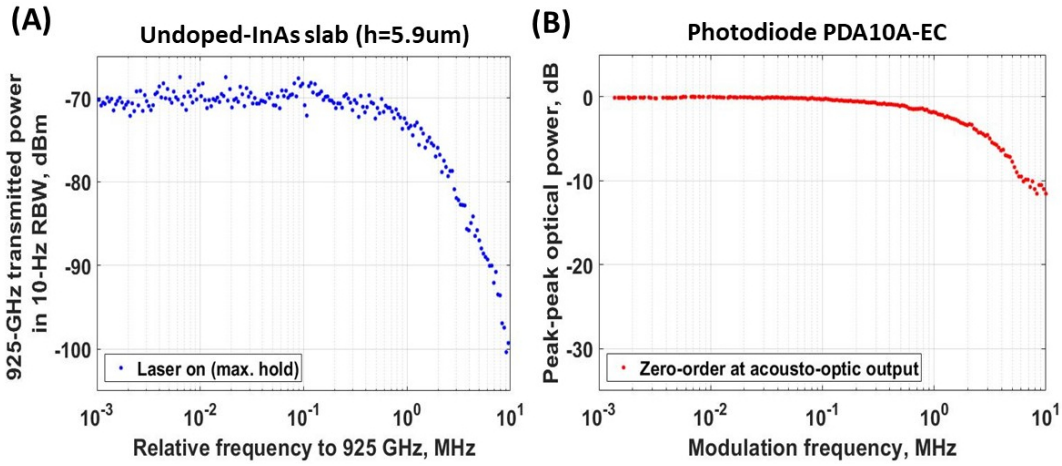

Figure 5.26 – *(A) THz transmitted power modulation for the right modulation satellite, the observed cut-off frequency of the InAs slab $h = 5.9\mu m$ is in the MHz range. (B) The photodiode PDA10A-EZ is used to observe the cut-off frequency of the AOM, it is located in the MHz range.*

according to the Fig.4.10.

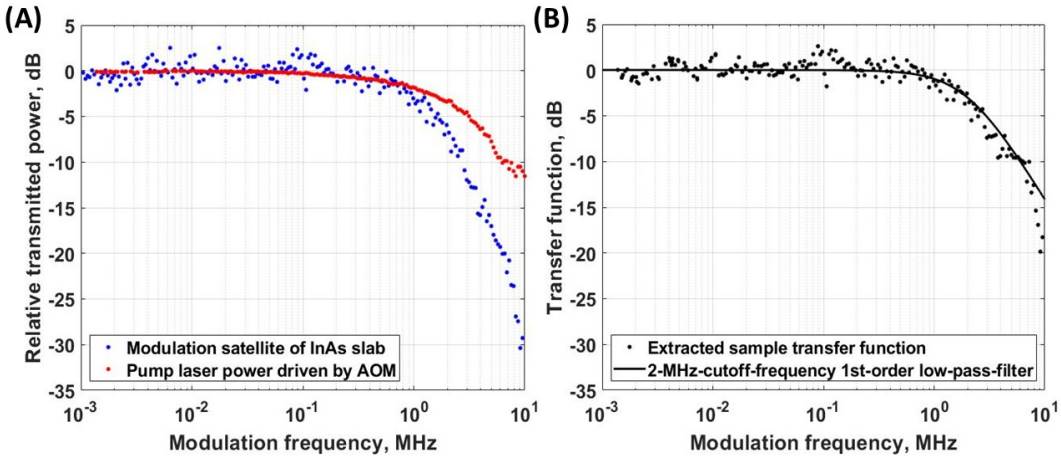

Figure 5.27 – *THz transmitted power modulation with and without laser at 1MHz in hold-on mode for the right modulation satellite.*

5.2.4 Conclusion

In this section, we have demonstrated that InAs is a promising semiconductor for the development of fast and efficient THz devices. We use two of the three static photo-driven THz modulator devices of thickness $h = 5.9\mu m$ (InAs epitaxial slab) and $h = 8.3\mu m$ (InAs wafer slab) which are driven by the CW pump. We demonstrated that low irradiance is enough to modulate at 20dB the THz transmission over a frequency range from 0.75 THz to 1.1 THz. The highest THz transmission modulation

is around 30dB with a low irradiance of only $\Phi_0 = 8.1W/cm^2$ in the continuous wave regime.

We used a modulated pump to convert the static THz modulator into a dynamic photo-driven THz modulator device using a AOM. We experimentally demonstrated a high-speed transmission modulation rate up to 2MHz, presently limited by the experimental set-up but with theoretical limits up to 0.5GHz. Nevertheless, we have the proof that MHz modulation is accessible with InAs for active plasmonics.

Before concluding, we recognize how impressive is the fact that such a small and tiny material of only a few μm can be able to modulate up to 30dB a wave of such large size as the THz wave radiation of around $300\mu m$ (1THz) when it is illuminated with an irradiance of only a few W/cm^2.

5.3 Summary

In this chapter, the experimental and theoretical results for the study of the optical characterization of the photo-excited InAs membranes were presented.

Firstly, the theoretically and experimentally optical characterization of the InAs membranes by using the experimental FTIR spectroscopy set-up and numerical simulations to study the optical control of the undoped-InAs material at different low-pump irradiances were presented. Experimental results demonstrate that low-pump irradiance is enough to modulate the transmission of the THz wave on a broadband frequency range. These results show that the InAs is a promising semiconductor for the development of fast and efficient THz components. The use of CW laser at an irradiance of few W/cm^2 is sufficient to modulate the transmission of the THz waves on a very large frequency range. A 50-fold decrease of the pumping irradiance is reached for a modulation of the THz transmission of 60% at 1THz when the InAs slab is pumped at very low irradiances compared to photo-generated surfaces made of gallium arsenide (GaAs) which have been realized with pump irradiances attaining hundreds of kW/cm^2.

Secondly, the theoretical and experimental modulation of the THz transmission up to 100% over a frequency range from 0.75 THz to 1.1 THz using very low pump fluence in the continuous wave regime were presented. Experimental results demonstrate that a modulated pump at an irradiance of few W/cm^2 is enough to dynamically control the THz transmission over a frequency range from 0.75 THz to 1.1THz and with a high-speed modulation rate up to 2MHz. We demonstrate that MHz modulation is accessible with InAs for active plasmonics at room-temperature.

These results represent a breakthrough for the conception of integrated and CMOS compatible dynamic THz modulator devices and might be a significant improvement for various non-destructive THz systems and THz applications such as sensing, imaging and security.

Conclusion and perspectives

The objective of this thesis was to propose a fundamental new design of photo-generated metasurfaces that tackles the actual limitations of high pump fluences required to manufacture fastly and efficiently THz components, as well as, the experimental demonstration of the theoretical statements by performing the technological fabrication of the photo-driven THz modulator prototype made of undoped-InAs material. This research was carried out in collaboration with the *Institut d'Electronique et des Systèmes* (IES) of Montpellier, in the NanoMir group and co-supervised by the Professor Thierry Taliercio.

Starting from theoretical statements, we propose a new conception of photo-generated metasurfaces which are photo-excited structures totally reconfigurable into the bulk to design a material by using photocarrier diffusion process and also on the surface to make the conventional flat components. This work reveals the crucial impact of the photocarrier diffusion to realize optimal metasurfaces for the versatile control of THz radiations. This scientific insight allows to control efficiently and dynamically the THz waves over a wide range of frequencies with very low pump irradiances and with high-speed modulation rate up to the MHz range.

Indium Arsenide is a material that tackles the actual limitations of this approach. The diffusion of the photocarriers plays a crucial role for realizing grating or homogeneous structures when a spatially modulated pump is considered. The study of the electronic and electromagnetic properties of an InAs layer shows that resonant absorption lines are monitored by the pump irradiance and by the spatial period of the pump. The best dynamical control for monitoring the absorption lines is obtained for a thickness of $15\,\mu m$ which corresponds to an ambipolar distance. In that case, a Fabry-Perot resonance arises close to ENZ regime and boosts the absorption to 50%. This ENZ-absorption can be optically actuated over a broad frequency band ranging from 1 THz to 3 THz when the pump fluence is increased from $25\,W.cm^{-2}$ to $100\,W.cm^{-2}$. These results open promising avenues for realizing on chip active THz components based on InAs since low pump powers of only $500\,mW$ can be easily delivered by integrated CW lasers.

We have contributed with two complementary recipes for the fabrication of photoconduction devices and THz modulation samples to experimentally demonstrate the main theoretical statements established, which are the ambipolar diffusion length and the active control of the THz radiation at low-pump irradiances, both at room-temperature. First, a photo-conduction device fabrication based on optical photolithography and dry chemical etching, applicable for the manufacturing process

of TLM devices was presented. This first part of this chapter finished with some SEM images of the TLM sample. The images show in detail the geometry of each TLM. Secondly, THz modulation samples process based on mechanical polishing and wet chemical etching is presented, applicable for the manufacturing process of undoped-InAs membranes of 10 to $1\mu m$ thick. The major achievements were to adapt the standard mechanical polishing to reduce the thickness of conventional undoped InAs acquired commercially. Two complementary etching rate for the undoped InAs have been studied at 60℃ by considering the influence of the size of the sample holder hole of $2mm$ by using the solution (H_3PO_4:H_2O_2:H_2O (2:1:2)). All these data have been integrated to the IES clean-room database. Laboratory microscope and SEM images of the undoped InAs membranes were presented. The images show in detail the geometry of the fabricated InAs membranes and that each InAs membrane has been deformed in a concave or convex shape due to mechanical forces produced by the wet chemical etching on the material.

The experimental and theoretical results for the optical characterization of the physical properties of InAs material, and the photo-conduction devices were presented. Firstly, the optical characterization of PL by using the experimental technique FTIR spectroscopy and numerical simulations to study the optical properties of the undoped-InAs material at different temperatures, at low-temperature and at room-temperature were presented. We experimentally verify the behaviour of the InAs material under different conditions when it is photo-excited by a laser pump. Furthermore, we have theoretically studied the excess carrier lifetime τ_r showing that the evolution of the effective lifetime τ_{eff} varies accordingly to the injection level $N(\tau_{eff})$. Secondly, experimental estimation of the ambipolar diffusion length in order to have a more accurate estimation of the τ_{eff} that we obtained in the PL section. It was performed using optical characterization in photo-conduction devices (TLM). We carried out experiments and numerical calculations of the optical characterization in photo-excited InAs membranes using a CW laser with an irradiance of only tens of W/cm^2. A linear fitting curve of the experimental data yields an experimental effective diffusion length L_{eff} between 40 to $2.5\mu m$. We use the carrier lifetime recombination τ_{eff} to fit the diffusion length values L_{eff}.

The experimental and theoretical results for the THz characterization of the photo-excited InAs membranes were presented. Firstly, the theoretically and experimentally optical characterization of the InAs membranes by using the experimental FTIR spectroscopy set-up and numerical simulations to study the optical control of the undoped-InAs material at different low-pump irradiances were presented. Experimental results demonstrate that low-pump irradiation is enough to modulate the transmission of the THz wave on a broadband frequency range. These results show that the InAs is an excellent semiconductor for the development of fast and efficient THz components. The use of CW laser at an irradiance of few W/cm^2 is sufficient to modulate the transmission of the THz waves on a very large frequency range. Secondly, the theoretically and experimentally modulation of the THz transmission up to 100% over a frequency range from 0.75 THz to 1.1 THz using very low pump irradiance in the continuous wave regime were presented. Experimental results demonstrate that a modulated pump at an irradiance of few W/cm^2 is enough to dynamically control the THz transmission over a frequency range from 0.75 THz to

1.1THz and with a high-speed modulation rate up to 2MHz.

Concluding on the achieved results, we demonstrate that InAs is a semiconductor for the development of fast and efficient THz devices. We show that these results overcome to the state-of-the-art technology limitations of the classical photo-generated metasurfaces technology such as: the high pump irradiances and the slow-speed THz modulation rate. Firstly, a 50-fold decrease of the pumping irradiance is reached for a modulation of the THz transmission of 60% at 1THz when the InAs slab is pumped at very low irradiances compared to photo-generated surfaces made of gallium arsenide (GaAs) which have been realized with pump irradiances attaining hundreds of kW/cm^2. These high irradiances reached with pulsed lasers are incompatible with integrated on-chip sources that deliver low intensity in the CW regime. Secondly, we demonstrate that MHz modulation is accessible with a photo-driven THz modulator made of InAs for active plasmonics at low pump irradiances (only a few W/cm^2) and at room-temperature. This photo-driven THz modulator is costless, compactness and with a high versatility able to address a wide range of frequencies compared to the current holographic technique (spatial light modulator device) linked to the photo-generated metasurfaces technology. This holographic system is fairly expensive, not compact and has a slow modulation rate up to 10kHz. These results represent a breakthrough for the conception of integrated and CMOS compatible dynamic THz modulator devices and might be a significant improvement for various THz applications such as sensing, imaging and security.

As a future work, to fully exploit the potential of the photo-generated metasurfaces we have to consider in the short term, the incorporation of the non-linear τ_{eff} curve to compute the correct photo-generated carrier density in order to properly estimate the variation of the relative photo-generated permittivity. Another important point is to include the roughness of the InAs surface in the home-made multiphysics code it will allow a better comparison between the numerical simulations and the experimental results obtained in the FTIR characterizations. In addition, the large effective diffusion length is also a limitation for realizing grating structures when a spatially modulated pump is considered because we cannot realize patterns smaller than two times L_{eff}. To conclude as short term, the incorporation of an additional electronics instrumentation faster than the AOM modulation to experimentally demonstrate the dynamic effect in the high-speed modulation of the THz waves which is driven by the carrier density $N(\tau_{eff})$. In the long term, include additional characterization techniques such as: plasmonics effects induced by photo-generated metasurfaces, growing multi-layer structures on different substrates with more complex shape and include this photo-generated technology with the conventional electronics by its integrable and adaptable low-pump irradiance. This versatile photo-generation manufacture will eventually allow to obtain structures with original shape properties that are unreachable with the standard recipes of clean room process. These original devices are environmentally favourable since they do not pollute the environment and due to the fact that their platform or screen are reusable for optical printing of different THz applications such as sensing, imaging and security. To conclude, we are convince that the theoretical and experimental knowledge acquired during this thesis opens the avenues to many others THz applications using photo-generated metasurfaces at terahertz frequencies based on the undoped-InAs material.

Appendix A

Scattering Matrix Method

The theoretical analysis of photo-generated metasurfaces developed in Chapter 2 requires the determination of the Scattering Matrix Method (S-Matrix). The S-matrix will connect the coefficients of the incoming fields to the coefficients of the outgoing fields, as presented in figureA.1.

$$\begin{bmatrix} A^{+1} \\ A^{-2} \end{bmatrix} = \begin{bmatrix} S_{11}^{1,2} & S_{12}^{1,2} \\ S_{21}^{1,2} & S_{22}^{1,2} \end{bmatrix} \begin{bmatrix} A^{-1} \\ A^{+2} \end{bmatrix} \tag{A.1}$$

where $A^{\pm(j)}$ corresponds to the field coefficients with its respective direction of propagation and (j) indicates the medium where the field coefficients are calculated.

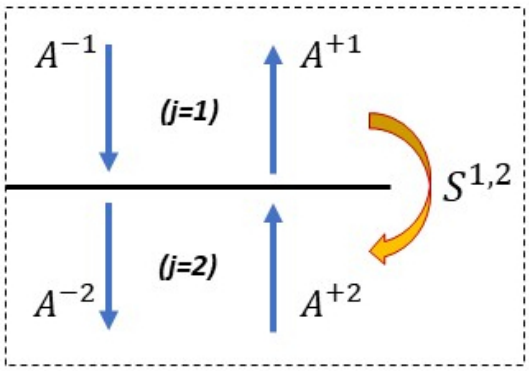

Figure A.1 – *Schematic of the interface matrix* $S^{1,2}$.

FigureA.2 shows that each interface of different medium ($j = 1$ - $j = 2$ - $j = 3$) can be described by using the S-matrix:

$$\begin{bmatrix} A^{+1} \\ A_1^{-2} \end{bmatrix} = \begin{bmatrix} S \end{bmatrix}^{(1,2)} \begin{bmatrix} A^{-1} \\ A_1^{+2} \end{bmatrix} \tag{A.2}$$

$$\begin{bmatrix} A_3^{+2} \\ A^{-3} \end{bmatrix} = \begin{bmatrix} S \end{bmatrix}^{(2,3)} \begin{bmatrix} A_3^{-2} \\ A^{+3} \end{bmatrix} \tag{A.3}$$

where $A_j^{\pm(2)}$ corresponds to the fields coefficients inside of the layer ($j = 2$), which are calculated at the superior interface ($j = 1$), or inferior interface ($j = 3$).

These fields coefficients are related by a phase relation $\phi = exp(-jkrh)$, where h is the height of the $(j = 2)$ layer. The phase relation is described by the propagation matrix, as presented in the equationA.4:

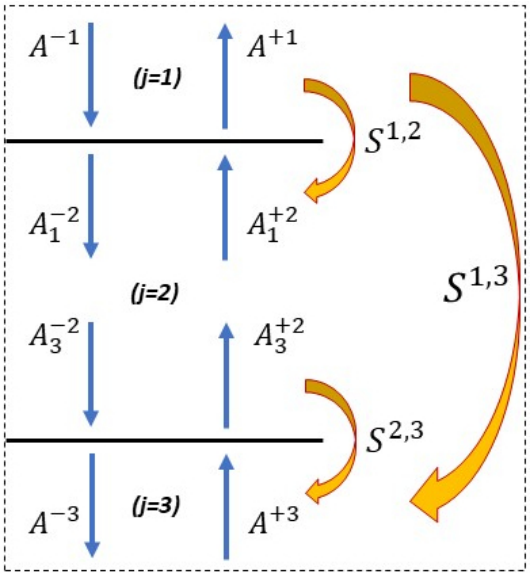

Figure A.2 – *Cascade relation of S-matrices.*

$$\begin{bmatrix} A_1^{+2} \\ A_3^{-2} \end{bmatrix} = \begin{bmatrix} 0 & \phi^{(2)} \\ \phi^{(2)} & 0 \end{bmatrix} \begin{bmatrix} A_1^{-2} \\ A_3^{+2} \end{bmatrix} \tag{A.4}$$

Thus, the coefficient of the transfer matrix between $(j = 1)$ and $(j = 3)$ can be calculated and given by:

$$\left[S\right]^{(1,3)} \begin{cases} S_{11}^{1,3} = S_{11}^{1,2} + S_{12}^{1,2}\phi^{(2)} Z_2 S_{11}^{2,3}\phi^{(2)} S_{21}^{1,2} \\ S_{12}^{1,3} = S_{12}^{1,2}\phi^{(2)} Z_2 S_{12}^{2,3} \\ S_{21}^{1,3} = S_{12}^{2,3}\phi^{(2)} Z_1 S_{21}^{1,2} \\ S_{22}^{1,3} = S_{22}^{2,3} + S_{21}^{2,3}\phi^{(2)} Z_1 S_{22}^{1,2}\phi^{(2)} S_{12}^{2,3} \end{cases}$$

$$where \begin{cases} Z_1 = (I - S_{22}^{1,2}\phi^{(2)} S_{11}^{2,3}\phi^{(2)})^{-1} \\ Z_2 = (I - S_{11}^{2,3}\phi^{(2)} S_{22}^{1,2}\phi^{(2)})^{-1} \end{cases}$$

Appendix B

Finite Difference Method

The theoretical analysis of photo-generated metasurfaces developed in Chapter 2 requires the determination of the Finite Difference Method (FDM). This method is used to solve the 1D diffusion equation for a system with finite length h and with mixed Dirichlet-Neumann conditions. We numerically solve the non uniform spatial distribution of the optical generation source term within the InAs slab which is given by:

$$\frac{\partial^2 N_i(y)}{\partial y^2} - \Big((iK)^2 + \frac{1}{L_a^2}\Big)N_i(y) = -\frac{G_i^{op}(y)}{D_a} \tag{B.1}$$

where $N(y)$ is the photo-generated carrier density, $D_a = 23.5cm^2s^{-1}$ is the ambipolar diffusion coefficient, $La = 15.32\,\mu m$ is the ambipolar diffusion length, $G_n^{op}(y)$ is the generation term related to the electric field intensity distributed in the y-direction and $K = 2\pi/d$ is the spatial frequency where d is the spatial grating period along the x-direction. To solve the last equation, we consider Dirichlet conditions, in this context equationB.1 yields:

$$\frac{N_{i+1} - 2N_i + N_{i-1}}{\Delta y^2} - \frac{N_i}{L_a^2} = fi, \tag{B.2}$$

where:

$$N_{i+1} - N_i(2+\alpha) + N_{i-1} = \Delta y^2 fi, \tag{B.3}$$

with:

$$\alpha = \Delta y^2(\frac{1}{L_a^2} + (iK)^2), \tag{B.4}$$

The initial condition (for $i = 1$) and the last condition (for $i = N$) in equationB.3 are given by:

$$N_2 - N_1(2+\alpha) + N_0 = \Delta y^2 f_1, \tag{B.5}$$

$$N_{N+1} - N_N(2+\alpha) + N_{N-1} = \Delta y^2 f_N, \tag{B.6}$$

where N_0 and N_{N+1} correspond to the boundary conditions of the system that relates the initial (s_i) and the final (s_f) surfaces recombination interaction. To determine the unknown variable at the boundaries, we discretize the Neumann condition to approximate the result of the unknown variable. In our case, we use an approximation of first order given by:

$$s_i N(y=0) = Da\frac{\partial N}{\partial y} \mid (y=0) = Da\frac{N_i - N_{i-1}}{\Delta y} \mid (y=0) \tag{B.7}$$

$$s_f N(y=h) = -Da\frac{\partial N}{\partial y} \mid (y=h) = -Da\frac{N_i - N_{i-1}}{\Delta y} \mid (y=h) \tag{B.8}$$

The opposite sign $\pm$ in the surface recombination (s_i) and (s_f) is in function of the orientation of the normal axis at the surface and specifies that the carrier flow is always directed towards the surface of the semiconductor. In this context, the boundaries may be written:

$$s_i N_1 = Da\frac{N_1 - N_0}{\Delta y} \tag{B.9}$$

$$s_f N_{N+1} = -Da\frac{N_{N+1} - N_N}{\Delta y} \tag{B.10}$$

The boundaries are found to be:

$$N_0 = N_1(1 - \frac{s_i \Delta y}{D_a}), \tag{B.11}$$

$$N_{N+1} = N_N(1 - \frac{s_f \Delta y}{D_a}), \tag{B.12}$$

We replace the expression of the equations (B.11 and B.12) in the equations (B.5 and B.6):

$$-N_2 + N_1(2 + \alpha - 1 + \frac{s_i \Delta y}{D_a}) = -\Delta y^2 f_1, \tag{B.13}$$

$$-N_{N-1} + N_N(2 + \alpha - 1 + \frac{s_f \Delta y}{D_a}) = -\Delta y^2 f_N, \tag{B.14}$$

In a matrix notation the above system of equation is simplified to:

$$M\vec{N} = -\Delta y^2 \vec{f}, \tag{B.15}$$

where the M matrix is:

$$\begin{bmatrix} [2+\alpha-N_0] & -1 & 0 & \dots & 0 & 0 & 0 \\ -1 & [2+\alpha] & -1 & \dots & 0 & 0 & 0 \\ \vdots & \ddots & \ddots & \ddots & \vdots & \vdots & \vdots \\ 0 & 0 & 0 & \dots & -1 & [2+\alpha] & -1 \\ 0 & 0 & 0 & \dots & 0 & -1 & [2+\alpha-N_{N+1}] \end{bmatrix} \begin{bmatrix} N_1 \\ N_2 \\ \vdots \\ N_{N-1} \\ N_N \end{bmatrix} = -\Delta y^2 \begin{bmatrix} f_1 \\ f_2 \\ \vdots \\ f_{N-1} \\ f_N \end{bmatrix}$$

Where the photo-generated carrier density distribution within the InAs slab is given by the following expression:

$$\vec{N} = M^{-1}(-\Delta y^2 \vec{f}) \tag{B.16}$$

Appendix C

InAs etching rate calibration

The wet etching analysis developed in Chapter 3 requires the determination of the InAs etching rate at 60℃. This study is used to reduce the InAs thickness in a shorter time, the temperature of the solution is increased from @25℃ to 60℃ in order to accelerate the etching rate. In this case, it is necessary to add the preparation of a solid mask made of SiO_2 to calculate a new proportionality law of the etching depth with the etching time at 60℃. The undoped-InAs substrate sample was subjected to the following process flow presented in figureC.1.

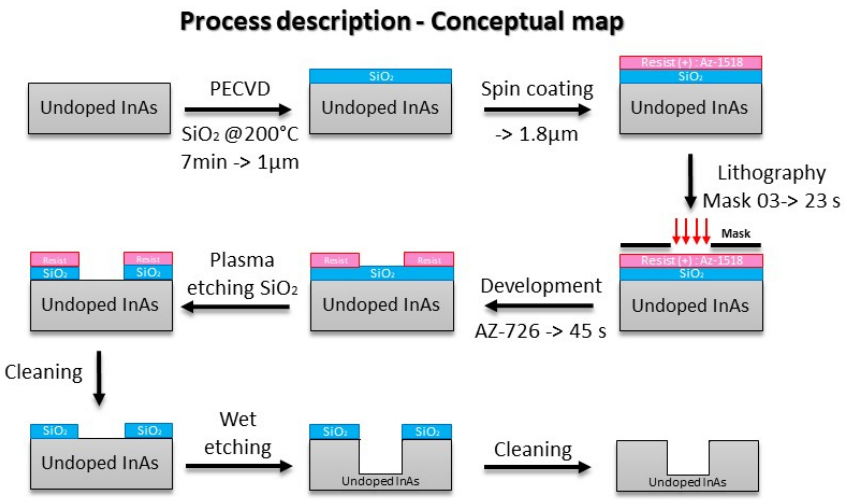

Figure C.1 – *Process flow for the calibration wet chemical etching. A. Substrate preparation. B. SiO_2 deposition. C. Photoresist deposition. D. Photolithography. E. Photoresist development. F. Plasma etching SiO_2. G. Photoresist Clean by oxygen plasma. H. Wet chemical etching. I. Final cleaning .*

1. Substrate preparation: clean with acetone and isopropanol and afterwards, cut the sample in five pieces. The pieces of undoped InAs have a thickness of 500um (Fig.C.1A).

2. SiO_2 deposition: a layer of $1.01um$ thick of SiO_2 is deposited on the top of the InAs material using a plasma enhanced chemical vapor deposition (PECVD)

chamber. The temperature in the growth chamber is 200°C. The deposition time is 7min (Fig.C.1.B).

3. Photoresist deposition: a layer of 1.8um of AZ-1518 photoresist is applied at 4000rpm for 30s with 4s acceleration ramp. Then, the solvent is evaporated by a postbake at 110°C for 1min (Fig.C.1.C).
4. Photolithography: the sample is insolated during 23s to UV exposure [105] using the mask $N-3$ available in Nanomir Group (Fig.C.1.D). The mask $N-3$ set-up is presented in figure C.2.

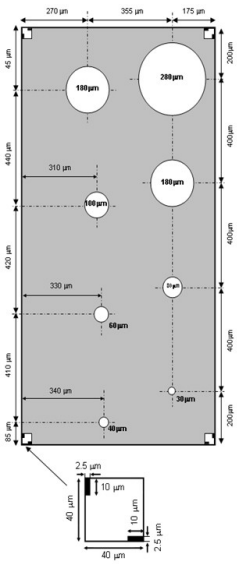

Figure C.2 – *Elementary pattern (1.6x0.8 mm) - Mask $N-3$*

5. Photoresist development: the photoresist is developed during 45s using AZ-726 developer (Fig.C.1.E).
6. Plasma etching SiO_2: the SiO_2 etching is performed in an inductively coupled plasma (ICP) reactive ion etching (RIE) reactor from Corial Plasma Processing Solutions. The SiO_2 etch depth is controlled by a laser interference measurements. One interference period corresponds to an etch depth and can be estimated by the following relation: $\lambda/2n$, where λ is the wavelength of the laser at $660nm$ and n the refractive index of the SiO_2 material. At this wavelength the refractive index is equal to $n(660nm) = 1.5$ and consequently one interference period corresponds to an etch depth of $220nm$. Therefore, five periods are needed to remove the SiO_2 layer of $1.01um$. The interference signal stops oscillating when it arrives on the InAs layer (Fig.C.1.F).
7. Photoresist clean by oxygen plasma: the sample is exposed to an oxygen plasma using the ICP corial reactor and the standard recipe from CTM for resist cleaning. This process ensures that all photoresist residues have been removed from the sample. The sample was exposed during $5min$ (Fig.C.1.G).
8. Wet chemical etching: the sample is divided into five pieces and then put into a solution of phosphoric acid diluted in hydrogen peroxide and water (H_3PO_4: H_2O_2 : H_2O (2 : 1 : 2)) at 60°C (Fig.C.1.H). More details about this process are presented below.

9. Final cleaning: The sample is successively rinsed with acetone, ethanol and isopropanol bath and dried under a nitrogen flow (Fig.C.1.I).

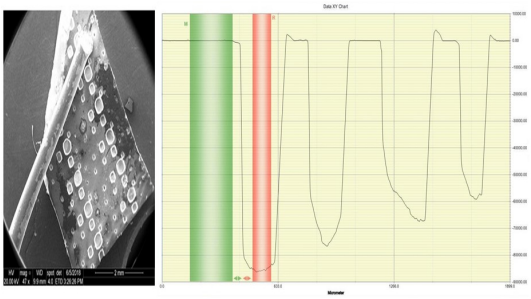

Figure C.3 – *Caption of the sample inspected by SEM. Dektak profilometer graph obtaining a description of the etch depth profile.*

To obtain the linear proportionality of the etch depth with the etch time at 60°C, the fabricated sample described previously has been cut in five pieces. The five pieces have been subjected to wet chemical etching (H_3PO_4:H_2O_2:H_2O (2:1:2)) at 60°C. Every five minutes one of the samples is removed from the solution. Then, the samples have been inspected by SEM and Dektak profilometer obtaining the etch depth profile (see FigureC.3). The profilometer shows that there are different depth profile in the sample (see FigureC.3). This is due to the influence of the circles of different sizes in mask $N-3$. The diameter's size gives a different value of the etching rate. The elaboration of a graph gives a linear-fit etching rate equal to $5.62\mu m/min$ considering a diameter of ($180\mu m$) (see FigureC.4). These datas have been entered into the IES clean-room database.

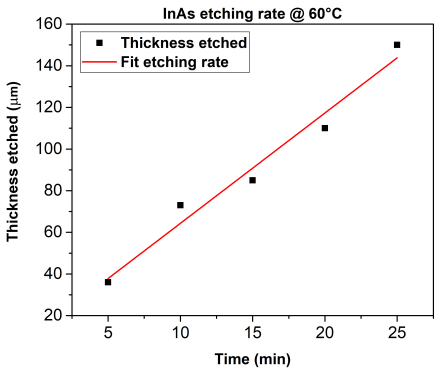

Figure C.4 – *A linear fitting curve is used to calculate the InAs etching rate. The mean value of the InAs etching rate is about 5.62 $\mu m/min$ considering a diameter of* ($180\mu m$).

After the obtention of the InAs etching rate using a solid mask made of SiO_2 with circles of different sizes, it is observed that the etching rate depends on the size of the mask circle. This fact motivated to reconsider the etching rate that will be used when a larger diameter of $2mm$ is used.

Then, a sample of InAs is polished until $100\mu m$ and then cut into twelve pieces. Each pieces of material is stuck to the sample holder. AZ-1518 photo-resist is applied to protect the inside of the hole support holder to protect it, and leaving only one face of the InAs material exposed to the consecutive etching process (Step presented in fabrication process - *Protection*). Then, the sample stuck in the sample holder is put in the solution of (H_3PO_4:H_2O_2:H_2O (2:1:2)) at 60℃.

The elaboration of a graph using the first eight samples analyzed with the profilometer gives a description of the etch depth profile. A linear-fit is computed obtaining an etching rate equal to $9.28\mu m/min$, considering a diameter of $2mm$ (see figureC.6).

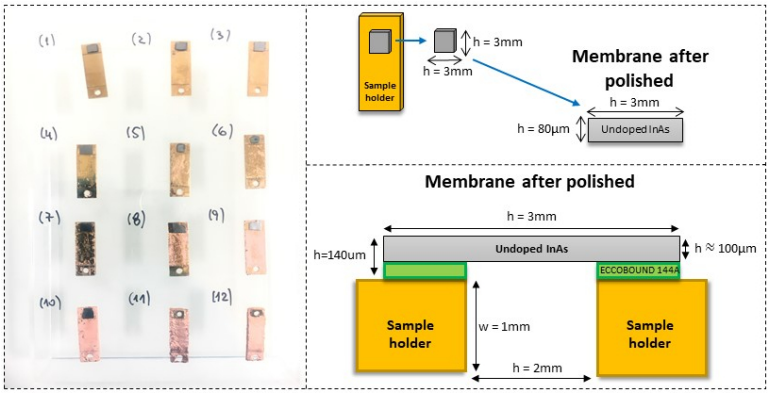

Figure C.5 – *InAs samples used to compute the etching rate considering a hole diameter of 2mm by using as a solution (H_3PO_4:H_2O_2:H_2O (2:1:2)) 60℃. The hole of 2mm diameter corresponds to the hole located in the sample holder.*

Remark, it is observed that while the etching time increases, the sample holder begins to corrode, losing the gold cover. It is possible to contemplate gradually the corrosion made by phosphoric acid on the holder sample, starting with a piece covered by gold until becoming completely copper . This fact require covering all the faces of the sample holder with AZ-1518 photoresist.

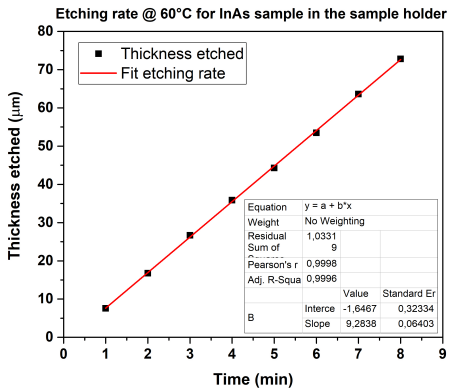

Figure C.6 – *InAs etching rate computed using a fitting curve. The mean value of the InAs etching rate is about 9.28 µm/min considering a diameter of 2mm.*

Bibliography

[1] SS Dhillon, MS Vitiello, EH Linfield, AG Davies, Matthias C Hoffmann, John Booske, Claudio Paoloni, M Gensch, Peter Weightman, GP Williams, et al. The 2017 terahertz science and technology roadmap. *Journal of Physics D: Applied Physics*, 50(4):043001, 2017.

[2] John F Federici, Brian Schulkin, Feng Huang, Dale Gary, Robert Barat, Filipe Oliveira, and David Zimdars. Thz imaging and sensing for security applications—explosives, weapons and drugs. *Semiconductor Science and Technology*, 20(7):S266, 2005.

[3] KI Zaitsev, NV Chernomyrdin, KG Kudrin, IV Reshetov, and SO Yurchenko. Terahertz spectroscopy of pigmentary skin nevi in vivo. *Optics and Spectroscopy*, 119(3):404–410, 2015.

[4] Swen Koenig, Daniel Lopez-Diaz, Jochen Antes, Florian Boes, Ralf Henneberger, Arnulf Leuther, Axel Tessmann, René Schmogrow, David Hillerkuss, Robert Palmer, et al. Wireless sub-thz communication system with high data rate. *Nature photonics*, 7(12):977, 2013.

[5] YC Shen, a T Lo, PF Taday, BE Cole, WR Tribe, and MC Kemp. Detection and identification of explosives using terahertz pulsed spectroscopic imaging. *Applied physics letters*, 86(24):241116, 2005.

[6] Danielle M Charron, Katsuhiro Ajito, Jae-Young Kim, and Yuko Ueno. Chemical mapping of pharmaceutical cocrystals using terahertz spectroscopic imaging. *Analytical chemistry*, 85(4):1980–1984, 2013.

[7] Kodo Kawase, Yuichi Ogawa, Yuuki Watanabe, and Hiroyuki Inoue. Non-destructive terahertz imaging of illicit drugs using spectral fingerprints. *Optics express*, 11(20):2549–2554, 2003.

[8] Hua Zhong, Albert Redo-Sanchez, and X-C Zhang. Identification and classification of chemicals using terahertz reflective spectroscopic focal-plane imaging system. *Optics Express*, 14(20):9130–9141, 2006.

[9] Nathan M Burford, Magda O El-Shenawee, Chad B O'neal, and Kraig J Olejniczak. Terahertz imaging for nondestructive evaluation of packaged power electronic devices. *Int. J. Emerg. Technol. Adv. Eng*, 4(1):395–401, 2014.

[10] MR Scarfi, M Romano, R Di Pietro, O Zeni, A Doria, GP Gallerano, E Giovenale, G Messina, A Lai, G Campurra, et al. Thz exposure of whole blood for

the study of biological effects on human lymphocytes. *Journal of Biological Physics*, 29(2-3):171–176, 2003.

[11] Richard H Clothier and Nicola Bourne. Effects of thz exposure on human primary keratinocyte differentiation and viability. *Journal of Biological Physics*, 29(2-3):179–185, 2003.

[12] E Pickwell and VP Wallace. Biomedical applications of terahertz technology. *Journal of Physics D: Applied Physics*, 39(17):R301, 2006.

[13] Zachary D Taylor, James Garritano, Shijun Sung, Neha Bajwa, David B Bennett, Bryan Nowroozi, Priyamvada Tewari, James W Sayre, Jean-Pierre Hubschman, Sophie X Deng, et al. Thz and mm-wave sensing of corneal tissue water content: In vivo sensing and imaging results. *IEEE transactions on terahertz science and technology*, 5(2):184–196, 2015.

[14] Calvin Yu, Shuting Fan, Yiwen Sun, and Emma Pickwell-MacPherson. The potential of terahertz imaging for cancer diagnosis: A review of investigations to date. *Quantitative imaging in medicine and surgery*, 2(1):33, 2012.

[15] M Koch, S Hunsche, P Schumacher, MC Nuss, J Feldmann, and J Fromm. Thz-imaging: a new method for density mapping of wood. *Wood Science and Technology*, 32(6):421–427, 1998.

[16] Sillas Hadjiloucas, Lucas S Karatzas, and John W Bowen. Measurements of leaf water content using terahertz radiation. *IEEE Transactions on microwave theory and techniques*, 47(2):142–149, 1999.

[17] Ian F Akyildiz, Josep Miquel Jornet, and Chong Han. Terahertz band: Next frontier for wireless communications. *Physical Communication*, 12:16–32, 2014.

[18] Steven Cherry. Edholm's law of bandwidth. *IEEE spectrum*, 41(7):58–60, 2004.

[19] Thomas Kürner and Sebastian Priebe. Towards thz communications-status in research, standardization and regulation. *Journal of Infrared, Millimeter, and Terahertz Waves*, 35(1):53–62, 2014.

[20] Tadao Nagatsuma, Guillaume Ducournau, and Cyril C Renaud. Advances in terahertz communications accelerated by photonics. *Nature Photonics*, 10(6):371, 2016.

[21] Mark J Rosker and H Bruce Wallace. Imaging through the atmosphere at terahertz frequencies. In *2007 IEEE/MTT-S International Microwave Symposium*, pages 773–776. IEEE, 2007.

[22] Josep Miquel Jornet and Ian F Akyildiz. Channel modeling and capacity analysis for electromagnetic wireless nanonetworks in the terahertz band. *IEEE Transactions on Wireless Communications*, 10(10):3211–3221, 2011.

[23] Jonathan Y Suen. Terabit-per-second satellite links: A path toward ubiquitous terahertz communication. *Journal of Infrared, Millimeter, and Terahertz Waves*, 37(7):615–639, 2016.

[24] Shian U Hwu, Cindy T Jih, et al. Terahertz (thz) wireless systems for space applications. In *2013 IEEE Sensors Applications Symposium Proceedings*, pages 171–175. IEEE, 2013.

[25] Peter H Siegel. Terahertz technology. *IEEE Transactions on microwave theory and techniques*, 50(3):910–928, 2002.

[26] Masayoshi Tonouchi. Cutting-edge terahertz technology. *Nature photonics*, 1(2):97, 2007.

[27] Daniel M Mittleman. Twenty years of terahertz imaging. *Optics express*, 26(8):9417–9431, 2018.

[28] Benjamin S Williams. Terahertz quantum-cascade lasers. *Nature photonics*, 1(9):517, 2007.

[29] Gian Piero Gallerano, S Biedron, et al. Overview of terahertz radiation sources. In *Proceedings of the 2004 FEL Conference*, volume 1, pages 216–221, 2004.

[30] JT Darrow, BB Hu, X-C Zhang, and DH Auston. Subpicosecond electromagnetic pulses from large-aperture photoconducting antennas. *Optics letters*, 15(6):323–325, 1990.

[31] Tao Chen, Liangling Wang, Lijuan Chen, Jing Wang, Haikun Zhang, and Wei Xia. Tunable terahertz wave difference frequency generation in a graphene/algaas surface plasmon waveguide. *Photonics Research*, 6(3):186–192, 2018.

[32] R Czarny, M Alouini, X Marcadet, S Bansropun, JL Doualan, R Moncorgé, JF Lampin, M Krakowski, and D Dolfi. Continuous wave thz generation based on a dual-frequency laser and a ltg-ingaas photomixer. In *2006 International Topical Meeting on Microwave Photonics*, pages 1–3. IEEE, 2006.

[33] Rüdeger Köhler, Alessandro Tredicucci, Fabio Beltram, Harvey E Beere, Edmund H Linfield, A Giles Davies, David A Ritchie, Rita C Iotti, and Fausto Rossi. Terahertz semiconductor-heterostructure laser. *Nature*, 417(6885):156, 2002.

[34] Cherif Belacel, Yanko Todorov, Stefano Barbieri, Djamal Gacemi, Ivan Favero, and Carlo Sirtori. Optomechanical terahertz detection with single meta-atom resonator. *Nature communications*, 8(1):1578, 2017.

[35] Christopher G Wade, Nikola Šibalić, Natalia R de Melo, Jorge M Kondo, Charles S Adams, and Kevin J Weatherill. Real-time near-field terahertz imaging with atomic optical fluorescence. *Nature Photonics*, 11(1):40, 2017.

[36] PY Han and XC Zhang. Free-space coherent broadband terahertz time-domain spectroscopy. *Measurement Science and Technology*, 12(11):1747, 2001.

[37] M Ashida, A Doi, S Saito, K Sakai, T Itoh, et al. Sensitivity of photoconductive antenna for ultrabroadband terahertz radiation: feasibility of detection over 100thz. In *International Quantum Electronics Conference, 2005.*, pages 1471–1472. IEEE, 2005.

[38] C Kübler, Rupert Huber, and A Leitenstorfer. Ultrabroadband terahertz pulses: generation and field-resolved detection. *Semiconductor science and technology*, 20(7):S128, 2005.

[39] Qi Wu and X-C Zhang. Free-space electro-optic sampling of terahertz beams. *Applied Physics Letters*, 67(24):3523–3525, 1995.

[40] Masato Suzuki, Masayoshi Tonouchi, Ken-ichi Fujii, Hideyuki Ohtake, and Tomoya Hirosumi. Excitation wavelength dependence of terahertz emission from semiconductor surface. *Applied physics letters*, 89(9):091111, 2006.

[41] M Yoshimura et al. Growth of 4-dimethylamino-n-methyl-4-stilbazolium tosylate (dast) crystal and its application to thz wave generation, 17ps-24. *Ext. Abs. Int. Work. Terahertz Technology*, 2005.

[42] Masahiko Tani, Kwang-Su Lee, and X-C Zhang. Detection of terahertz radiation with low-temperature-grown gaas-based photoconductive antenna using 1.55 μm probe. *Applied Physics Letters*, 77(9):1396–1398, 2000.

[43] Zhiping Jiang and X-C Zhang. 2d measurement and spatio-temporal coupling of few-cycle thz pulses. *Optics express*, 5(11):243–248, 1999.

[44] Michel Rochat, Lassaad Ajili, Harald Willenberg, Jerome Faist, Harvey Beere, Giles Davies, Edmund Linfield, and David Ritchie. Low-threshold terahertz quantum-cascade lasers. *Applied Physics Letters*, 81(8):1381–1383, 2002.

[45] Alan WM Lee, Qi Qin, Sushil Kumar, Benjamin S Williams, Qing Hu, and John L Reno. Real-time terahertz imaging over a standoff distance ($>$ 25 meters). *Applied Physics Letters*, 89(14):141125, 2006.

[46] Erwin Hack, Lorenzo Valzania, Gregory Gäumann, Mostafa Shalaby, Christoph Hauri, and Peter Zolliker. Comparison of thermal detector arrays for off-axis thz holography and real-time thz imaging. *Sensors*, 16(2):221, 2016.

[47] Nathaniel K Grady, Jane E Heyes, Dibakar Roy Chowdhury, Yong Zeng, Matthew T Reiten, Abul K Azad, Antoinette J Taylor, Diego AR Dalvit, and Hou-Tong Chen. Terahertz metamaterials for linear polarization conversion and anomalous refraction. *Science*, 340(6138):1304–1307, 2013.

[48] Ren-Hao Fan, Yu Zhou, Xiao-Ping Ren, Ru-Wen Peng, Shang-Chi Jiang, Di-Hu Xu, Xiang Xiong, Xian-Rong Huang, and Mu Wang. Freely tunable broadband polarization rotator for terahertz waves. *Advanced Materials*, 27(7):1201–1206, 2015.

[49] Nanfang Yu, Patrice Genevet, Mikhail A Kats, Francesco Aieta, Jean-Philippe Tetienne, Federico Capasso, and Zeno Gaburro. Light propagation with phase discontinuities: generalized laws of reflection and refraction. *science*, 334(6054):333–337, 2011.

[50] Nanfang Yu and Federico Capasso. Flat optics with designer metasurfaces. *Nature materials*, 13(2):139, 2014.

[51] Nanfang Yu and Federico Capasso. Optical metasurfaces and prospect of their applications including fiber optics. *Journal of Lightwave Technology*, 33(12):2344–2358, 2015.

[52] Prasad P Iyer, Nikita A Butakov, and Jon A Schuller. Reconfigurable semiconductor phased-array metasurfaces. *ACS Photonics*, 2(8):1077–1084, 2015.

[53] Ho-Seok Ee and Ritesh Agarwal. Tunable metasurface and flat optical zoom lens on a stretchable substrate. *Nano letters*, 16(4):2818–2823, 2016.

[54] Kebin Fan and Willie J Padilla. Dynamic electromagnetic metamaterials. *Materials Today*, 18(1):39–50, 2015.

[55] Wenshan Cai and Vladimir M Shalaev. *Optical metamaterials*, volume 10. Springer, 2010.

[56] Tomer Lewi, Prasad P Iyer, Nikita A Butakov, Alexander A Mikhailovsky, and Jon A Schuller. Widely tunable infrared antennas using free carrier refraction. *Nano letters*, 15(12):8188–8193, 2015.

[57] Ioannis Chatzakis, Philippe Tassin, Liang Luo, Nian-Hai Shen, Lei Zhang, Jigang Wang, Thomas Koschny, and Costas M Soukoulis. One-and two-dimensional photo-imprinted diffraction gratings for manipulating terahertz waves. *Applied Physics Letters*, 103(4):043101, 2013.

[58] Maxim R Shcherbakov, Sheng Liu, Varvara V Zubyuk, Aleksandr Vaskin, Polina P Vabishchevich, Gordon Keeler, Thomas Pertsch, Tatyana V Dolgova, Isabelle Staude, Igal Brener, et al. Ultrafast all-optical tuning of direct-gap semiconductor metasurfaces. *Nature communications*, 8(1):17, 2017.

[59] Takanori Okada and Koichiro Tanaka. Photo-designed terahertz devices. *Scientific reports*, 1:121, 2011.

[60] Giorgos Georgiou, HK Tyagi, P Mulder, GJ Bauhuis, JJ Schermer, and J Gómez Rivas. Photo-generated thz antennas. *Scientific reports*, 4:3584, 2014.

[61] Jinying Guo, Teng Wang, Huan Zhao, Xinke Wang, Shengfei Feng, Peng Han, Wenfeng Sun, Jiasheng Ye, Guohai Situ, Hou-Tong Chen, et al. Reconfigurable terahertz metasurface pure phase holograms. *Advanced Optical Materials*, page 1801696, 2019.

[62] Francesco P Mezzapesa, Lorenzo L Columbo, Carlo Rizza, Massimo Brambilla, Alessandro Ciattoni, Maurizio Dabbicco, Miriam S Vitiello, and Gaetano Scamarcio. Photo-generated metamaterials induce modulation of cw terahertz quantum cascade lasers. *Scientific reports*, 5:16207, 2015.

[63] G Georgiou, C Tserkezis, MC Schaafsma, Javier Aizpurua, and J Gómez Rivas. Active loaded plasmonic antennas at terahertz frequencies: Optical control of their capacitive-inductive coupling. *Physical Review B*, 91(12):125443, 2015.

[64] Tom P Steinbusch, Hemant K Tyagi, Martijn C Schaafsma, Giorgos Georgiou, and J Gómez Rivas. Active terahertz beam steering by photo-generated graded index gratings in thin semiconductor films. *Optics express*, 22(22):26559–26571, 2014.

[65] Yuanmu Yang, N Kamaraju, Salvatore Campione, Sheng Liu, John L Reno, Michael B Sinclair, Rohit P Prasankumar, and Igal Brener. Transient gaas plasmonic metasurfaces at terahertz frequencies. *ACS Photonics*, 4(1):15–21, 2016.

[66] Carlo Rizza, Alessandro Ciattoni, Lorenzo Columbo, Massimo Brambilla, and Franco Prati. Terahertz optically tunable dielectric metamaterials without microfabrication. *Optics letters*, 38(8):1307–1309, 2013.

[67] Xinke Wang, Zhenwei Xie, Wenfeng Sun, Shengfei Feng, Ye Cui, Jiasheng Ye, and Yan Zhang. Focusing and imaging of a virtual all-optical tunable terahertz fresnel zone plate. *Optics letters*, 38(22):4731–4734, 2013.

[68] Carlo Rizza, Alessandro Ciattoni, Francesco De Paulis, Elia Palange, Antonio Orlandi, Lorenzo Columbo, and Franco Prati. Reconfigurable photoinduced metamaterials in the microwave regime. *Journal of Physics D: Applied Physics*, 48(13):135103, 2015.

[69] Kai Liu, Jingzhou Xu, Tao Yuan, and X-C Zhang. Terahertz radiation from inas induced by carrier diffusion and drift. *Physical Review B*, 73(15):155330, 2006.

[70] Aaron J Miller, Arttu Luukanen, and Erich N Grossman. Micromachined antenna-coupled uncooled microbolometers for terahertz imaging arrays. In *Terahertz for Military and Security Applications II*, volume 5411, pages 18–25. International Society for Optics and Photonics, 2004.

[71] T Yasui, A Nishimura, T Suzuki, K Nakayama, and S Okajima. Detection system operating at up to 7 thz using quasioptics and schottky barrier diodes. *Review of scientific instruments*, 77(6):066102, 2006.

[72] S Ariyoshi, C Otani, A Dobroiu, H Sato, K Kawase, HM Shimizu, T Taino, and H Matsuo. Terahertz imaging with a direct detector based on superconducting tunnel junctions. *Applied physics letters*, 88(20):203503, 2006.

[73] S Komiyama, O Astafiev, V Antonov, T Kutsuwa, and H Hirai. A single-photon detector in the far-infrared range. *Nature*, 403(6768):405, 2000.

[74] G Georgiou. Photo-generated terahertz devices. 2016.

[75] Eduardo Alvear-Cabezón, Rafik Smaali, Emmanuel Centeno, Fernando Gonzalez-Posada, and Thierry Taliercio. Photogenerated metasurfaces at terahertz frequencies induced by a continuous-wave low pump. *Physical Review B*, 98(3):035305, 2018.

[76] R Smaali, T Taliercio, and E Centeno. Photo-generated metasurfaces for resonant and high modulation of terahertz signals. *Optics letters*, 41(16):3900–3903, 2016.

[77] Rafik Smaali, Fatima Omeis, Antoine Moreau, Thierry Taliercio, and Emmanuel Centeno. A universal design to realize a tunable perfect absorber from infrared to microwaves. *Scientific reports*, 6:32589, 2016.

[78] Rafik Smaali, Fatima Omeis, Antoine Moreau, Emmanuel Centeno, and Thierry Taliercio. Miniaturizing optical antennas using hyperbolic metamaterial wires. *Physical Review B*, 95(15):155306, 2017.

[79] Franziska B Barho, Fernando Gonzalez-Posada, Maria-José Milla-Rodrigo, Mario Bomers, Laurent Cerutti, and Thierry Taliercio. All-semiconductor plasmonic gratings for biosensing applications in the mid-infrared spectral range. *Optics express*, 24(14):16175–16190, 2016.

[80] Franziska B Barho, Fernando Gonzalez-Posada, Maria-Jose Milla, Mario Bomers, Laurent Cerutti, Eric Tournié, and Thierry Taliercio. Highly doped semiconductor plasmonic nanoantenna arrays for polarization selective broadband surface-enhanced infrared absorption spectroscopy of vanillin. *Nanophotonics*, 7(2):507–516, 2018.

[81] Thierry Taliercio, Fernando Gonzalez-Posada Flores, Franziska B Barho, María José Milla-Rodrigo, Mario Bomers, Laurent Cerutti, and Eric Tournié. Plasmonic bio-sensing based on highly doped semiconductors. In *Optical Sensing, Imaging, and Photon Counting: Nanostructured Devices and Applications 2017*, volume 10353, page 103530S. International Society for Optics and Photonics, 2017.

[82] Carlo Rizza, Lorenzo Columbo, Massimo Brambilla, Franco Prati, and Alessandro Ciattoni. Extrinsic electromagnetic chirality in all-photodesigned one-dimensional terahertz metamaterials. *Physical Review B*, 93(24):241305, 2016.

[83] Edward D Palik. *Handbook of optical constants of solids*, volume 3. Academic press, 1998.

[84] Junho Yoon, Ming Zhou, Md Alamgir Badsha, Tae Young Kim, Young Chul Jun, and Chang Kwon Hwangbo. Broadband epsilon-near-zero perfect absorption in the near-infrared. *Scientific reports*, 5:12788, 2015.

[85] Simon Vassant, Alexandre Archambault, François Marquier, Fabrice Pardo, Ulf Gennser, Antonella Cavanna, Jean-Luc Pelouard, and Jean-Jacques Greffet. Epsilon-near-zero mode for active optoelectronic devices. *Physical review letters*, 109(23):237401, 2012.

[86] Young Chul Jun, John Reno, Troy Ribaudo, Eric Shaner, Jean-Jacques Greffet, Simon Vassant, Francois Marquier, Mike Sinclair, and Igal Brener. Epsilon-near-zero strong coupling in metamaterial-semiconductor hybrid structures. *Nano letters*, 13(11):5391–5396, 2013.

[87] Inigo Liberal and Nader Engheta. Near-zero refractive index photonics. *Nature Photonics*, 11(3):149, 2017.

[88] David E Aspnes and AA Studna. Dielectric functions and optical parameters of si, ge, gap, gaas, gasb, inp, inas, and insb from 1.5 to 6.0 ev. *Physical review B*, 27(2):985, 1983.

[89] Emmanuel Rosencher and Borge Vinter. *Optoelectronics*. Cambridge University Press, 2002.

[90] Yassine Sayad. Détermination de la longueur de diffusion des porteurs de charge minoritaires dans le silicium cristallin par interaction lumière matière. *Institut National des Sciences Appliquées de Lyon*, 2009.

[91] Donald A Neamen et al. Semiconductor physics and devices. 1992.

[92] YP Varshni. Band-to-band radiative recombination in groups iv, vi, and iii-v semiconductors (i). *physica status solidi (b)*, 19(2):459–514, 1967.

[93] Joel Chaskalovic. *Finite element methods for engineering sciences: theoretical approach and problem solving techniques*. Springer Science & Business Media, 2008.

[94] Carlo Rizza, Alessandro Ciattoni, Elisa Spinozzi, and Lorenzo Columbo. Terahertz active spatial filtering through optically tunable hyperbolic metamaterials. *Optics letters*, 37(16):3345–3347, 2012.

[95] C Hilsum. Simple empirical relationship between mobility and carrier concentration. *Electronics Letters*, 10(13):259–260, 1974.

[96] MP Mikhailova, M Levinshtein, S Rumyantsev, and M Shur. Handbook series on semiconductor parameters. *Word Scientific*, 1:147–168, 1996.

[97] Henry Mathieu and Hervé Fanet. *Physique des semiconducteurs et des composants électroniques*, volume 189. Dunod Paris, 2001.

[98] G Granet and B Guizal. Efficient implementation of the coupled-wave method for metallic lamellar gratings in tm polarization. *JOSA A*, 13(5):1019–1023, 1996.

[99] Sidhant Grover. Effect of transmission line measurement (tlm) geometry on specific contact resistivity determination. 2016.

[100] S Maimon and GW Wicks. n b n detector, an infrared detector with reduced dark current and higher operating temperature. *Applied Physics Letters*, 89(15):151109, 2006.

[101] PC Klipstein. Xbnn and xbpp infrared detectors. *Journal of Crystal Growth*, 425:351–356, 2015.

[102] Hector Cotal, Chris Fetzer, Joseph Boisvert, Geoffrey Kinsey, Richard King, Peter Hebert, Hojun Yoon, and Nasser Karam. Iii–v multijunction solar cells for concentrating photovoltaics. *Energy & Environmental Science*, 2(2):174–192, 2009.

[103] Nan Yao and Zhong Lin Wang. *Handbook of microscopy for nanotechnology.* Springer, 2005.

[104] Hari Singh Nalwa. *Handbook of Advanced Electronic and Photonic Materials and Devices, Ten-Volume Set*, volume 1. Academic Press, 2000.

[105] Theodore C Hennessy. *Lithography: principles, processes and materials.* Nova Science,, 2011.

[106] Stephen J Pearton, Cammy R Abernathy, and Fan Ren. *Topics in growth and device processing of III-V semiconductors*, volume 1. World scientific, 1996.

[107] JJ Kelly, JEAM van de Meerakker, PHL Notten, and RP Tijburg. Wet-chemical etching of iii-v semiconductors. *Philips technical review*, 44(3):61–74, 1988.

[108] John Chalmers and Peter Griffiths. *Handbook of Vibrational Spectroscopy, 5 volumes set.* Wiley, 2002.

[109] RE Hester and RJH Clark. Spectroscopy for surface science, 1998.

[110] Peter Fellgett. *Theory of infra-red sensitivites and its application to investigations of stellar radiation in the near infra-red.* PhD thesis, University of Cambridge, 1951.

[111] E Knözinger. Pr griffiths, ja de haseth: Fourier transform infrared spectroscopy, vol. 83 aus der reihe: Chemical analysis—a series of monographs of analytical chemistry and its applications, john wiley+ sons, chichester, new york, brisbane, toronto, singapore 1986. 656 seiten, preis:£ 76.75. *Berichte der Bunsengesellschaft für physikalische Chemie*, 90(12):1240–1241, 1986.

[112] Arsen V Subashiev, Oleg Semyonov, Zhichao Chen, and Serge Luryi. Urbach tail studies by luminescence filtering in moderately doped bulk inp. *Applied Physics Letters*, 97(18):181914, 2010.

[113] Yatendra Pal Varshni. Temperature dependence of the energy gap in semiconductors. *Physica*, 34(1):149–154, 1967.

[114] I Vurgaftman, J áR Meyer, and L áR Ram-Mohan. Band parameters for iii–v compound semiconductors and their alloys. *Journal of applied physics*, 89(11):5815–5875, 2001.

[115] WT Tsang, EF Schubert, and JE Cunningham. Doping in semiconductors with variable activation energy. *Applied physics letters*, 60(1):115–117, 1992.

[116] J Domaradzki. Light-beam-induced current (lbic) technique for semiconductors and ics testing. In *Lightmetry 2002: Metrology and Testing Techniques Using Light*, volume 5064, pages 269–275. International Society for Optics and Photonics, 2003.

[117] BA Oliver and AE Dixon. Laser beam induced current measurements of minority carrier diffusion length. *Canadian Journal of Physics*, 65(8):814–820, 1987.

[118] RM Cosby, JH Logsdon, and BR Gossick. An experimental determination of the ambipolar diffusion coefficient in germanium. *Solid-State Electronics*, 16(12):1441–1446, 1973.

[119] SM Davidson and CA Dimitriadis. Advances in the electrical assessment of semiconductors using the scanning electron microscope. *Journal of microscopy*, 118(3):275–290, 1980.

[120] Yassine Sayad, A Kaminski, D Blanc, A Nouiri, and M Lemiti. Determination of diffusion length in photovoltaic crystalline silicon by modelisation of light beam induced current. *Superlattices and Microstructures*, 45(4-5):393–401, 2009.

[121] SAYAD Yassine. *Interaction Laser-Semiconducteur: Contribution à l'étude de la technique LBIC-application au silicium photovoltaïque.* PhD thesis, UNIVERSITE MENTOURI DE CONSTANTINE, 2009.

[122] Richard Bardoux. *Spectroscopie de boîtes quantiques individuelles GaN/AlN en phase hexagonale.* PhD thesis, Université Montpellier II-Sciences et Techniques du Languedoc, 2007.

[123] M Ortolani, JS Lee, U Schade, and H-W Hübers. Surface roughness effects on the terahertz reflectance of pure explosive materials. *Applied Physics Letters*, 93(8):081906, 2008.

[124] Stefan F Busch, Steffen Schumann, Christian Jansen, Maik Scheller, Martin Koch, and Bernd M Fischer. Optically gated tunable terahertz filters. *Applied Physics Letters*, 100(26):261109, 2012.

[125] T Kleine-Ostmann, K Pierz, G Hein, P Dawson, Michel Marso, and Martin Koch. Spatially resolved measurements of depletion properties of large gate two-dimensional electron gas semiconductor terahertz modulators. *Journal of Applied Physics*, 105(9):093707, 2009.

[126] AJ Fitzgerald, E Berry, NN Zinovev, GC Walker, MA Smith, and JM Chamberlain. An introduction to medical imaging with coherent terahertz frequency radiation. *Physics in Medicine & Biology*, 47(7):R67, 2002.

[127] K Humphreys, JP Loughran, Marcin Gradziel, W Lanigan, T Ward, J Anthony Murphy, and Créidhe O'Sullivan. Medical applications of terahertz imaging: a review of current technology and potential applications in biomedical engineering. In *The 26th Annual International Conference of the IEEE Engineering in Medicine and Biology Society*, volume 1, pages 1302–1305. IEEE, 2004.

Publications and Conference proceedings list

Publications

• *Eduardo Alvear-Cabezón, Rafik Smaali, Fernando Gonzalez-Posada, Thierry Taliercio, and Emmanuel Centeno*, "**Photogenerated metasurfaces at terahertz frequencies induced by a continuous-wave low pump**.". Physical Review B, **98** 035305 July (2018).

• *Eduardo Alvear-Cabezón, Rafik Smaali, Fernando Gonzalez-Posada, Thierry Taliercio, and Emmanuel Centeno*, "**Photo-generated carriers in InAs slab at THz frequencies induced by a continuous wave low irradiance**." (Experimental work - Under preparation)

• *Eduardo Alvear-Cabezón, Stephane Blin, Philippe Nouvel, Fernando Gonzalez-Posada, Rafik Smaali, Roland Teissier, Alexei Baranov, Thierry Taliercio, and Emmanuel Centeno*, "**Photo-driven THz modulator based on InAs slab induced by a continuous-wave low irradiance**." (Experimental work - Under preparation)

• *Eduardo Alvear-Cabezón, Rafik Smaali, Fernando Gonzalez-Posada, Thierry Taliercio, and Emmanuel Centeno*, "**Plasmonics effects induced by photo-generated metasurfaces at THz frequencies**." (Theoretical work - Under preparation)

Conference Proceedings

SEPT 2019	INTERNATIONAL CONFERENCE ON INFRARED, MILLIMETER, AND TERAHERTZ WAVES (IRMMW-THz) **Paris, France** *Eduardo Alvear-Cabezón, Stephane Blin, Philippe Nouvel, Fernando Gonzalez-Posada, Rafik Smaali, Roland Teissier, Alexei Baranov, Thierry Taliercio, and Emmanuel Centeno* "Low-pump irradiance to modulate THz waves driven by photo-generated carriers in an InAs slab." Poster
MAY 2019	SURFACE PLASMON PHOTONICS (SPP9) **Copenhagen, Denmark** *Eduardo Alvear-Cabezón, Rafik Smaali, Stephane Blin, Fernando Gonzalez-Posada, Thierry Taliercio, and Emmanuel Centeno* "Photo-generated metasurfaces at Teraherz frequencies." Poster
APR 2019	FRENCH-GERMAN THz CONFERENCE 2019 (FGTC) **Kaiserslautern, Germany** *Eduardo Alvear-Cabezón, Rafik Smaali, Stephane Blin, Fernando Gonzalez-Posada, Thierry Taliercio, and Emmanuel Centeno* "Photo-generated carriers in InAs slab at THz frequencies induced by a continuous wave low irradiance." Oral
AUG 2018	INTERNATIONAL CONFERENCE ON THE PHYSICS OF SEMICONDUCTORS (ICPS) **Montpellier, France** *Eduardo Alvear-Cabezón, Rafik Smaali, Fernando Gonzalez-Posada, Thierry Taliercio, and Emmanuel Centeno* "Photo-generated metasurfaces at THz frequencies induced by a CW low-pump." Poster
JUNE 2018	JOURNÉE DU NANO, MICRO ET OPTOÉLETRONIQUE (JNMO) **Agay-Cap Esterel, France** *Eduardo Alvear-Cabezón, Rafik Smaali, Fernando Gonzalez-Posada, Thierry Taliercio, and Emmanuel Centeno* "Photo-generated metasurfaces at THz frequencies induced by a continuous wave low-pump." Poster
MAI 2018	JOURNÉES DU NANOSCIENCES ET ONDES DU TÉRAHERTZ AU MOYEN INFRAROUGE (GDR NANOTERAMIR) **Montpellier, France** *Eduardo Alvear-Cabezón, Rafik Smaali, Fernando Gonzalez-Posada, Thierry Taliercio, and Emmanuel Centeno* "Photo-generated metasurfaces at THz frequencies induced by a CW low-pump." Poster